UNIVERSITY OF NOVA GORICA
GRADUATE SCHOOL

STUDIES OF SCHEMES TO OBTAIN COHERENT VUV AND X-RAY PULSES: SEEDED HARMONIC GENERATION, SELF-SEEDING AND SELF- AMPLIFIED SPONTANEOUS EMISSION

DISSERTATION

Simone Spampinati

Mentor: prof. dr. Giovanni De Ninno

Nova Gorica, 2014

UNIVERZA V NOVI GORICI
FAKULTETA ZA PODIPLOMSKI ŠTUDIJ

ŠTUDIJ NAČINOV ZA GENERACIJO KOHERENTNIH PULZOV V VUV IN RENTGENSKEM PODROČJU

DISERTACIJA

Simone Spampinati

Mentor: prof. dr. Giovanni De Ninno

Nova Gorica, 2014

This thesis is dedicated to my parents and my brother.

Acknowledgments

First I would like to thank my advisor, prof. Giovanni De Ninno, for giving me the opportunity to candidate me for a phd. I would also thank him for his support in these years and for his guidance to the completion of this thesis. I would also thank prof. G. Bratina and prof S.Stanic to have admitted me to the graduated school of the University of Nova Gorica. I would also thank prof S. Stanic for helps in the correction of the thesis. I want thank to who supported me with working positions during my phd: Emanuel Karantzoulis, Alessandro Fabbris, Stephen Milton, Michele Svanderlik and prof. Tor Raubenheimer. I would also thank Tor for a lot of discussions, suggestions and corrections of the thesis. I want thank to Luca Giannessi to have introduce me to the physics of free electron laser, for a lot of lessons and for an invaluable example of enthusiasm.

I enjoyed a lot of great helps from my colleagues Alberto Lutman, Enrico Allaria, Laura Badano, Davide Castronovo, Max Cornacchia, Paolo Craievich, Miltcho Danailov, Alexander Demidovich, Yuantao Ding, Bruno Diviacco, Eugenio Ferrari, William M. Fawley, Lars Froehlich, Zhirong Huang, Henry Loos, Heinz-Dita Nuhn, Giuseppe Penco, Daniel Ratner, Carlo Spezzani, Cristian Svetina, Mauro Trovo', Marco Veronese, Jihao Yi and Marco Zangrando during discussions and commissioning times in Trieste and at SLAC.

Special acknowledgments go to Simone Di Mitri and Juhao Wu for a lot of discussions and lessons on accelerator and FEL physics.

I want thank prof Shaukat Khan and David Newton for a lot of helps and corrections of the thesis.

I want thank to my friends: Alberto, Alessandro, Andrea, Annalisa, Annamaria, Bibi, Chris, Claudio, Cristina, Daniele, David, Dennis, Fabrizio, Federico, Giacomo, Giusy, Lia, Luca, Laura, Marco, Matteo, Max, Sara, Stefano, Paolo, Pietro, Rytis, Tomasz, Valentina, Vincenzo.

Finally, I thank my parents my brother Luca and my aunt Angela for their support and encouragements.

Abstract

The need for coherent and intense pulsed radiation is spread among many research disciplines, such as biology, nanotechnology, physics, chemistry and medicine. Synchrotron light only partially meets these requirements. A new kind of light source, Free-Electron Laser (FEL), has been developed in the last decades to provide radiation in VUV/X-ray spectral region with characteristics beyond the reach of conventional light sources. In fact, FELs such as LCLS, FLASH and SACLA work regularly in the self ampli_ed spontaneous emission regime (SASE) producing short (<100 fs) and very intense (up to tens of GW) VUV and X-ray radiation pulses, characterized by good transverse coherence but poor longitudinal coherence, relevant shot-to-shot central frequency and power _uctuations. In this work we present the experimental results obtained using three techniques, aimed at further improving the spectral and temporal quality of SASE FEL light. The most promising technique is high-gain harmonic generation (HGHG). We will present the commissioning of FERMI@ELETTRA FEL1 line. Our activity provided a signi_cant contribution to the extension of harmonic generation in the deep VUV and X-ray regime. This required a careful optimization of the electron beam used to drive the FEL process. Our work focused in particular on the implementation of the laser heater system devoted to suppress microbunching instability. The second technique that will be described is self-seeding, applied to the hard X-ray regime. We will present the results of the experiments done at LCLS (to which we have actively participated) and the simulations that we have performed in order to interpret the obtained results. Finally, we have demonstrated the possibility to reduce dramatically the spectral width of SASE mode, generating isolated radiation spikes. The test experiment, on this scheme, carried at SPARC will be described here. In conclusion, this work provides new experimental results supporting the idea of using FELs as light sources capable of generating fully coherent and powerful pulses in the VUV and X-ray spectral regime, and con_rming the importance of the electron beam quality to reach spectral purity and high _ux of these pulses.

Keywords: FEL, longitudinal coherence, microbunching, laser heater, seeding, HGHG, self seeding, tapering.

Povzetek

Potrebe po koherentnih pulznih svetlobnih izvorov z visoko luminoznostjo so skupne raznim znanstvenim področjem, biologija, nanotehnologija, fizika, kemija in medicina. Sinhrotronska svetloba samo delno izpolnjuje te zahteve. Z namenom, da bi ustvarili sevanje v spektralnem območju VUV (10 nm - 200 nm) in X (0.01 nm - 10 nm) z lastnostmi, ki presegajo zmožnosti konvencionalnih svetlobnih virov, je bila v zadnjih desetletjih razvita nova vrsta svetlobnih izvorov, t.i. "laserji na proste elektrone" (free electron lasers" ali FEL). FEL naprave, kot so Linac Coherent Light Source (LCLS) v ZDA, Free-electron-LASer v Hamburgu (FLASH) v Nemčiji in SPring-8 Angstrom Compact free electron laser (SACLA) na Japonskem običajno delujejo v načinu t.i. samo-ojačevane spontane emisije (SASE) ter generirajo kratke (<100 fs) in zelo močne (do več deset GW) svetlobne pulze v spektralnem območju VUV in X žarkov. Ti pulzi imajo dobro transverzalno koherenco, slabo longitudinalno koherenco in precejšnje fluktuacije centralne frekvence in moči med pulzi.

V disertaciji predstavljamo rezultate uporabe treh različnih tehnik za izboljšanje spektralne in časovne kakovosti pulzov, ki nastajajo v FEL pri načinu SASE. Za najbolj obetavno tehniko se je izkazalo generiranje višjih harmonikov z visokim izkoristkom (high-gain harmonic generation oziroma HGHG). Predstavili bomo zagon prve faze (FEL1) projekta FERMI@ELETTRA, kjer smo tehniko HGHG tudi uporabili in s tem pomembno prispevali k povišanju generiranja harmonikov v globoko območje VUV in X žarkov. Izvedba HGHG je zahtevala natančno optimizacijo žarka elektronov, ki se uporablja za generacijo svetlobnih pulzov v FEL. Osredotočili smo se predvsem na zagon grelnega laserja za odstranitev nestabilnosti elektronskega žarka v obliki mikro gruč. Druga tehnika, ki smo jo uporabili, je t.i. "self-seeding", ki se običajno uporablja v področju X žarkov najvišjih energij. Predstavili bomo rezultate eksperimentalnega dela na FEL napravi LCLS in simulacij, ki so bile potrebne za njihovo interpretacijo. V zadnjem delu smo, na podlagi eksperimentalnega dela na FEL napravi SPARC, predstavili nov način, ki bo lahko omogočal bistveno zmanjšanje spektralne širino SASE svetlobnih pulzov in generiranje ostrih konic SASE svetlobe.

Disertacija zajema skupek novih rezultatov, ki omogočajo uporabo FEL kot svetlobnih virov za generacijo popolnoma koherentnih svetlobnih pulzov z visoko luminoznostjo v spektralnem območju VUV in X žarkov. Rezultati prav tako potrjujejo, da je kakovost elektronskega žarka v FEL bistvenega pomena za doseganje spektralne čistosti in visoke luminoznosti izsevanih svetlobnih pulzov.

Ključne besede: laser na proste elektrone, FEL, longitudinalna koherenca, mikro gruče, generiranje višjih harmonikov z visokim izkoristkom, HGHG, grelni laser, časovno okno.

Contents

Chapter 1

Introduction

1.1 Introduction

Synchrotron radiation established itself, in the last decades, as one of the most important tools for scientific discoveries through the implementation of techniques like diffraction, spectroscopy, scattering and microscopy [1]. The achievable wavelengths cover the range from hard X-rays to infrared light. One of the most important figures of merit of synchrotron radiation facilities is the spectral brightness, which defines the photon flux per unit area, unit solid angle and unit spectral bandwidth. Typical synchrotron brightness values are around $10^{19} - 10^{21} \cdot (photons/\mathrm{s} \cdot mm^2 \cdot mrad^2 \cdot 0.1\% \cdot bandwidth)$. Other important characteristics are the bandwidth, the wavelength tunability and the pulse duration. Despite the obtained successes, the light produced by synchrotron machines does not permit the realization of a large class of experiments that require more intense and shorter light pulses, or a complete coherence of the employed radiation. Light pulses delivered by synchrotron machines have

a time duration ranging between tens and hundreds of *ps*. Therefore, they are not suited to resolve in time electronic and molecular dynamics, which evolve with time scales of the order of tens or hundreds of femtoseconds [2, 3, 4]. Other classes of experiments on non-linear phenomena require a single-shot photon flux higher than that provided by synchrotrons [5, 6]. In order to meet these requirements, free-electron lasers (FELs) were proposed [7, 8, 9]. These devices can provide a peak brilliance many orders of magnitude higher than that of synchrotron facilities. The brilliance of some synchrotron beamlines as well as of proposed and existing FEL is shown in figure 1.1 The improvement in terms of peak brightness of the X-FEL projects with respect to a typical synchrotron source is evident.

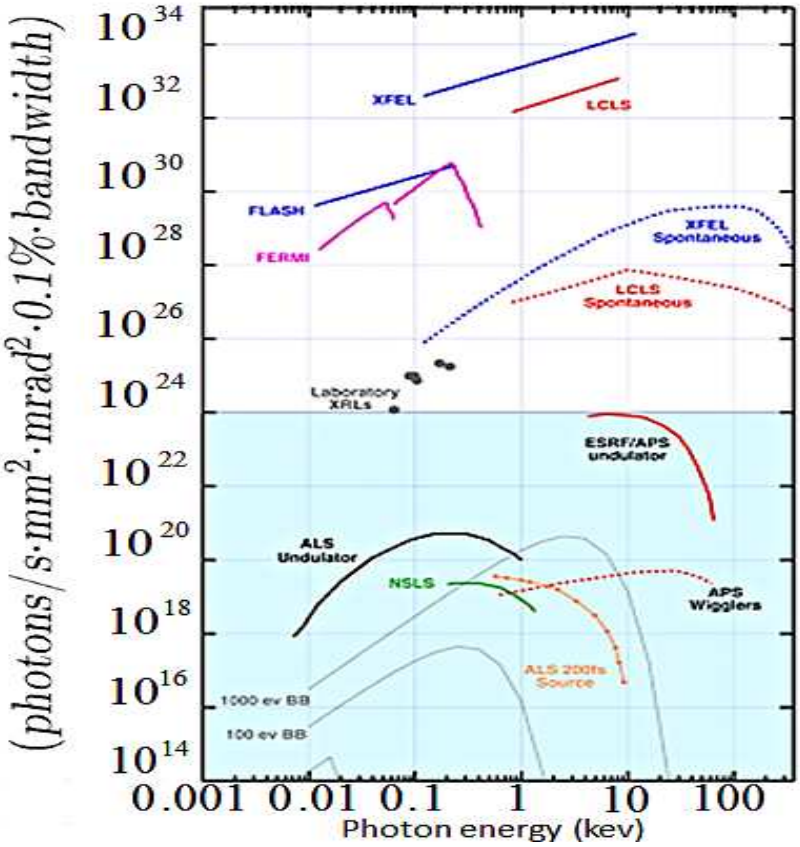

Figure 1.1: Brightness of light sources based on synchrotrons and FELs. The improvement in terms of peak brightness of the X-FEL projects with respect to a typical synchrotron source is evident. Courtesy of A. Nelson.

LCLS (linac coherent light source), FLASH (Free-Electron laser in Hamburg) and SACLA (SPring-8 Angstrom Compact free-electron laser) [10, 11, 12] are three facilities just working in the soft X-ray regime (LCLS, FLASH, SACLA) and in the hard X-ray regime (LCLS, SACLA) while a FEL working down to 20 *nm* has actually been commissioned at FERMI@Elettra [13].

Temporal coherence [14] is the measure of the average correlation between the wave and

itself delayed by τ, at any pair of times. The delay over which the phase and the amplitude changes by a significant amount (and hence the correlation decreases by significant amount) is defined as the coherence time τ_c. At $\tau = 0$ the degree of coherence is perfect whereas it drops significantly when the time delay increases to τ_c. The coherence length L_c is defined as the distance the wave travels in the coherence time. The coherence time is a measure of the monochromaticity of the light, since by Fourier transformation:

$$\tau_c \simeq \frac{1}{\Delta\nu_L} \qquad L_c \simeq \frac{c}{\Delta\nu_L} \tag{1.1}$$

where $\triangle\nu_L$ is the spectral width of the wave (full width at half maximum, FWHM) and c is the speed of light. The minimum possible duration (FWHM) for a wave with the spectral bandwidth $\triangle\nu_L$ is:

$$\triangle\tau_L = \frac{0.44}{\triangle\nu_L} \tag{1.2}$$

$$\triangle\nu_L \triangle\tau_L = c \cdot \triangle\tau_L \frac{\triangle\lambda_L}{(\lambda_L)^2} = 0.44 \tag{1.3}$$

The equations 1.2 and 1.3 are valid for a pulse with Gaussian shape in time and frequency while a pulse with a different shape has a greater time-bandwidth product. It is clear, from equations 1.1 and 1.3, that a pulse with a time-bandwidth product given by 1.3, i.e. a Gaussian pulse, has the longest coherence length possible associated with a given pulse duration. Any deviation of the time-bandwidth product value from 0.44 implies a reduc-

tion of the coherent length. The transverse coherence implies a definite phase relationship between points separated by a distance L transverse to the direction of beam propagation. The spatial coherence can be measured in a classic Young's slits interference experiment [15]. The transverse coherence and the large photon flux open up new perspectives for single-shot imaging, allowing single pulse coherent diffraction imaging [16, 17].

Synchrotron radiation is temporally incoherent and characterized by only partial transverse coherence. LCLS, FLASH and SACLA work regularly producing short and very intense x-ray radiation pulse characterized by good transverse coherence but poor longitudinal coherence [18, 19], relevant shot to shot central frequency fluctuations and power fluctuations. On the other hand, experiments in the vacuum ultraviolet (VUV) region producing completely coherent pulses have been performed at several test facilities such as DUV FEL [20] at BNL laboratory, the FEL on the Elettra synchrotron ring in TRIESTE [21], SPARC (Sorgente pulsate amplificata radiazione coerente) [22] in Frascati (INFN/ENEA/CNR) and MAX 4 demonstrator in Lund [23]. The extension of the schemes applied and results obtained by these facilities down to *nm* wavelength requires a careful design of the electron beam source, as in the case of FERMI@Elettra [24]. Fully coherent pulses in the deep VUV and X-ray regime will allow, for example, multi-dimensional spectroscopy [25, 26] of valence excitations in molecules [27] and coherent electron-hole interaction [28], the probing of the electron correlation in solids via inelastic X-ray scattering [29] with very high resolution and TG [30, 31] formation in the sample with a nanometer scale spatial period.

The work presented in this manuscript reports some experiments devoted to improve longitudinal coherence and spectral purity and stability of VUV and X-FEL. We will analyse results obtained at FERMI@Elettra, LCLS and SPARC. We will describe FEL schemes

and measurements related to these experiments. We will show that the FEL longitudinal and transverse coherence, and the spectral quality, are influenced also by electron beam properties. Then, we will discuss the way to optimize the electron beam in the context of FERMI@Elettra.

1.2 FEL principle and schemes

Radiation production in a FEL [7] is based on the passage of a relativistic electron beam through the periodic magnetic field of an undulator, generating emission at a resonant frequency fixed by the electron energy and undulator period and magnetic field. Different types of undulator can be used. The most common are the planar and the helical undulators [32]. The undulator axis coincides with the direction of propagation of the electrons and the direction of propagation of the wave. The magnetic field is perpendicular to the undulator axis. The plane undulator is formed by a series of alternating dipoles. The electrons follow a sinusoidal trajectory in the plane containing the undulator axis and perpendicular to the magnetic field of the undulator as shown in figure 1.2.

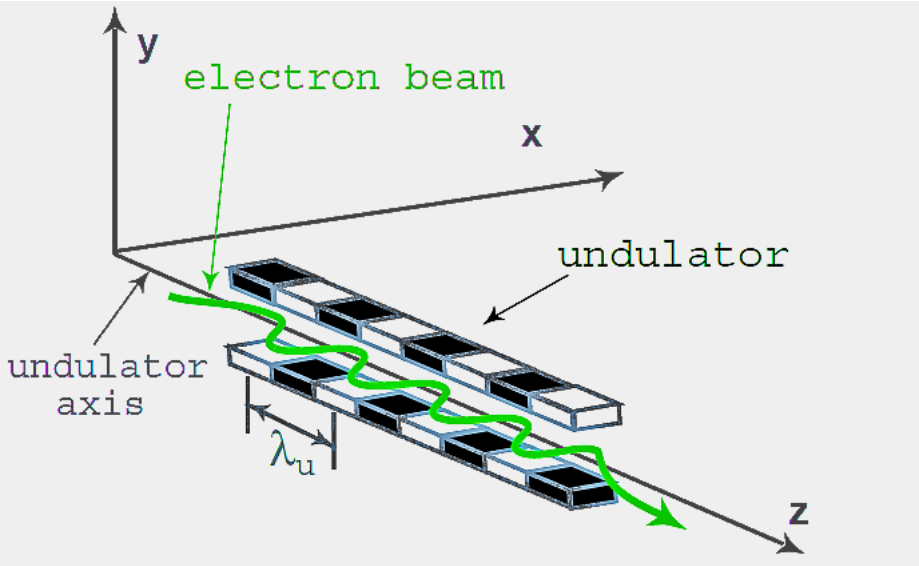

Figure 1.2: Electron trajectory (green line) in a planar undulator. The magnetic field of the undulator forces the electron on a zig-zag path with a spatial period that copies that of the undulator.

In a helical undulator the electrons follow a helical path. The resonance wavelength that is the central wavelength of the undulator on axis radiation is given by [32]:

$$\lambda_r = \frac{\lambda_U}{2\gamma^2}\left(1 + K_{rms}^2\right) \tag{1.4}$$

$$K = \frac{e_0 B_0 \lambda_U}{\beta m_e c} \tag{1.5}$$

where $K = K_{rms}$ for a helical undulator and $K = \sqrt{2} \cdot K_{rms}$ for a planar undulator. Here λ_U is the undulator period, γ is the Lorentz factor, e_0 is the electron charge, B_0 is the on axis magnetic field generated by the undulator and m_e is the electron mass. K is the undulator strength parameter. The transverse velocity of the electrons, which is driven

by the undulator magnetic field, couples through the Lorentz force to a co-propagating electromagnetic wave at the same resonant frequency. The electric field of the wave must be contained in the plane in which the electron moves [33]. The electrons interact with a linearly polarized radiation in a planar undulator and with an elliptically polarized radiation in a helical undulator. This interaction produces a spatial modulation at the scale of the laser wavelength (bunching) into the electron beam. When the bunching is significant, the beam starts to radiate coherently, reaching intensities much higher than spontaneous emission [34]. The co-propagating radiation can be provided by an external seed laser or can be the spontaneous radiation produced by the beam in the undulator. In these two cases we have respectively a seeded [8] and a self-amplified spontaneous emission (SASE) [35] FEL. Both seeded and SASE FELs can generate very short wavelengths, and in both cases the amplification of the radiation with the fundamental wavelength is accompanied by the production of radiation at high harmonics of the fundamental with an energy decreasing with the harmonic number [36]. An exponential instability in the field amplitude derives from the self-consistently coupled equations that describe the FEL process [33]. The light has a higher velocity with respect to that of the wiggling electrons and there is a slippage of the radiation with respect to the electrons. When the resonance condition is satisfied, the light advances one wavelength for each undulator period. Electrons can communicate with the ones ahead only if their separation is less than the total slippage $N\lambda_R$. N is the total number of undulator periods. The SASE [35] scheme relies on the presence of a (weak) bunching factor at any wavelength (shot noise), naturally present in the electron beam at the entrance of the undulator [37]. The component of the shot noise matching the undulator resonant wavelength is amplified, leading to an exponential growth of the

spontaneous radiation [38]. The radiation power exponentially grows along the undulator as $P(z) \propto P(0)e^{-\frac{z}{L_G}}$ [39], where $P(0)$ is the initial radiation power, L_G is the so called gain length, and z is the coordinate along the undulator, up to a saturation value given by $P_{sat} \approx \rho P_e$ where $P_e = EI$ is the electron beam power and ρ is the Pierce parameter defined as $\rho = \frac{\lambda_U}{4\pi L_G}$ [40]. SASE FELs require very high-gain as the input power given by noise is very weak. Figure 1.3 shows the scheme of a SASE FEL.

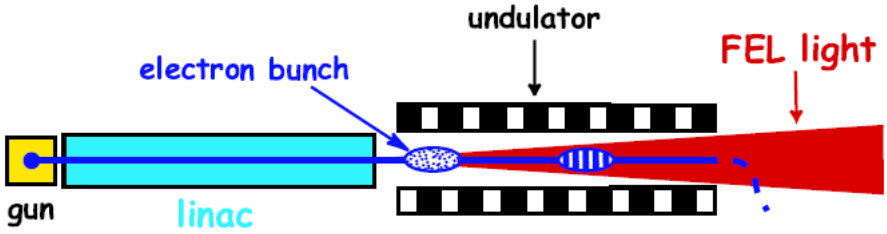

Figure 1.3: FEL in single-pass SASE configuration. The electron beam is generated in the gun, accelerated in a linear accelerator (linac) and then injected in the undulator. The electron beam emits spontaneous radiation in the undulator and interacts with it. The electron beam contains a weak bunching factor at any wavelength as a consequence of the current granularity (shot noise). The component of the shot noise matching the undulator resonant wavelength is amplified, leading to an exponential growth of the spontaneous radiation. Courtesy of F. Curbis.

The length $\lambda_R \frac{L_G}{\lambda_U}$ represents the slippage in one gain length and is called cooperation length and it is $< 20\,\mu m$, i.e. only a small fraction of length of typical electron beam that is $20 - 300\,\mu m$. FELs in SASE mode deliver powerful light pulses with good transverse properties but poor longitudinal coherence [41, 42]. In the SASE regime, the amplification starts from noise. Therefore the amplification process starts from a different input in any part of the beam. Then, initially the emitted radiation has a random value of phase and amplitude along the beam. The output SASE radiation consists of a series of spikes [35]. There is no

phase relation between the different spikes and any spike identifies a region over which phase and amplitude correlation is established by the slippage of the radiation over the electrons. The spikes' length is then equal to the cooperation length. Any SASE pulse contains tens of longitudinal modes not correlated in phase and the bandwidth is therefore much larger than the transform limited value of the pulse duration [35]. The stochastic nature of shot noise causes a large shot-to-shot amplitude and wavelength fluctuation of SASE radiation [35].

In a seeded FEL amplifier, an external laser is injected in the undulator with the electron beam that acts as an active gain medium amplifying the input signal. In this case the longitudinal coherence and the spectral stability of the seed are transferred to the FEL radiation. The first FEL amplifier reported experiment was done at Stanford amplifying a CO_2 laser [8]. Figure 1.4 shows the FEL amplifier concept [43].

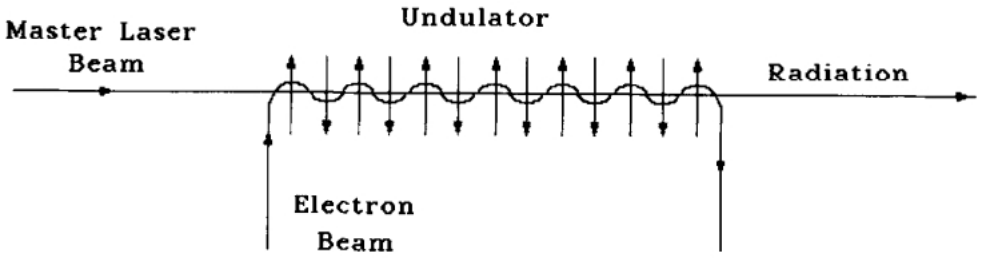

Figure 1.4: Conceptual scheme of a FEL amplifier [43]. The electron beam is injected in the undulator with a co-propagating laser beam. The laser beam is amplified by the interaction with the electron beam.

The harmonics of Ti:Sa lasers [44] are today more frequently used as seeds in FEL experiments. These harmonics can be produced focusing the beam with a wavelength of 750-800 *nm* into a crystal [45] or a noble gas [46]. Crystals permit the production of intense radiation

beams at the second and third harmonic of the fundamental while the radiation emerging from the gas contains higher harmonics [47]. As we have just seen, some harmonic conversion and amplification happens in the FEL too with an efficiency decreasing with the harmonic number. It is possible to increase the efficiency at higher harmonics working with two independent undulators, the second one being tuned to one of the harmonics of the first. The external seed interacts with the electrons in the first undulator. The laser-electron interaction produces energy modulation in the bunch at the wavelength of the laser. Then, the beam goes through a magnetic device (dispersive section), in which the path length of the electrons depends on their energy. In this way the energy modulation is converted in a density modulation at the harmonics of the seed. The beam is now ready to emit coherently in a second longer undulator (called radiator), tuned at one of the harmonics of the seed laser. This scheme, called high-gain harmonic generation (HGHG) [48], is shown in figure 1.5:

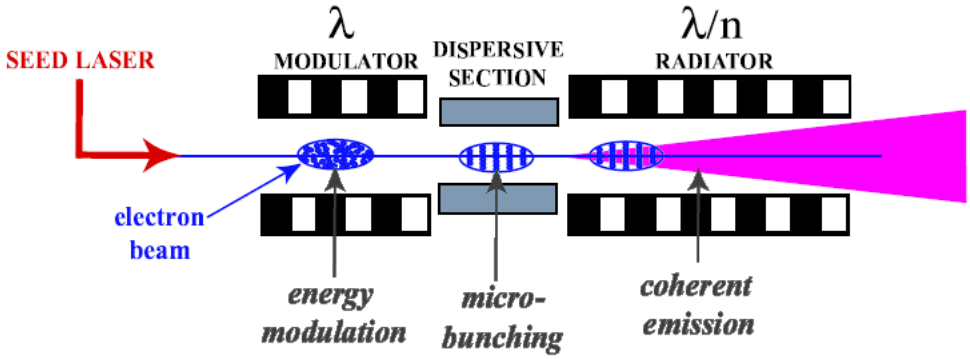

Figure 1.5: Scheme of a FEL working in the HGHG. The electron beam interacts with the seed laser within the modulator. Here the beam energy is modulated by the laser. The energy modulation is converted in a density modulation, at the harmonics of the laser wavelength, in the dispersive section. FEL radiation is emitted in the radiator tuned at the desired harmonic of the seed. Courtesy of F.Curbis.

Several seed FEL experiments in HGHG and in direct seeding configuration have been performed [20, 21, 22, 23]. HGHG can be repeated with a second stage composed of a modulator, a dispersive section and a radiator following the first stage. In this case the FEL radiation produced in the first radiator is used as a short wavelength high power seed in the second modulator. A magnetic chicane can be placed between the first radiator and the second modulator to delay the electron beam with respect to the seed. In this way the FEL production in the second stage starts in a fresh part of the bunch. This method is called the fresh bunch technique [49]. Figure 1.6 shows the fresh bunch scheme.

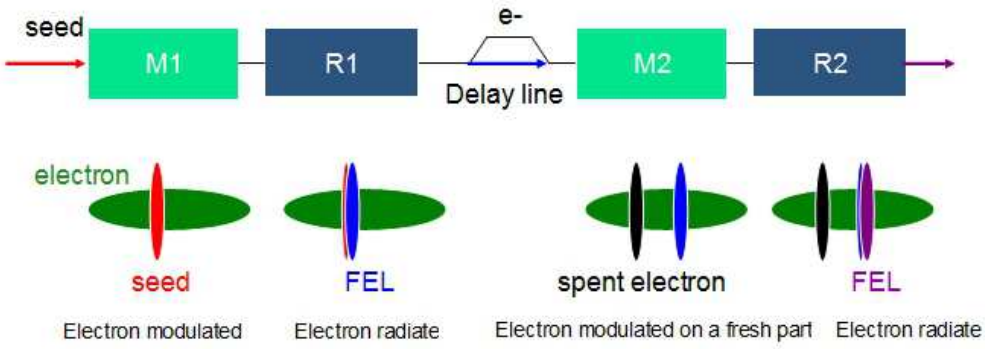

Figure 1.6: Fresh bunch scheme. The electron beam interacts with the seed laser in the first modulator and it gains a spatial energy modulation at the laser wavelength. The energy modulation is converted in a density modulation, at the harmonics of the laser wavelength, in the first dispersive section. FEL light is produced in the first radiator that is tuned to a selected harmonic of the seed. This first HGHG stage is followed by another in which the light pulse produced in the first radiator is used to modulate the electron beam in the second modulator. The electron beam is delayed, by a magnetic chicane, with respect to the FEL pulse before entering in the modulator. In this way the entire HGHG process, in the second stage, happens in a fresh part of the bunch. Courtesy of L. Giannessi.

Up to now we have described high-gain single-pass configurations in which the radiation is produced while the electrons make one single trip through the undulator line and is directly

extracted and used for experiments. FELs can work even in oscillator configuration in which the radiation is accumulated in an optical cavity during more trips of the electron beam in the undulators [50]. This permits the use of a less bright electron beam and for this reason it can be implemented even on storage rings, exploiting the high repetition rate and stability of these accelerator machines [51]. On the other hand, the efficiency of optical cavities and mirrors is low in the extreme VUV and X-ray regime and therefore the operations of oscillator FELs are actually limited to wavelengths longer than $\approx 200\,nm$ [52]. For this reason only single stage schemes have been studied and implemented in the VUV and X-ray regime, even if also FEL oscillator schemes are proposed [53, 54]. This thesis describes and discusses only single stage FELs. Figure 1.7 shows a FEL oscillator scheme implemented on a storage ring FEL.

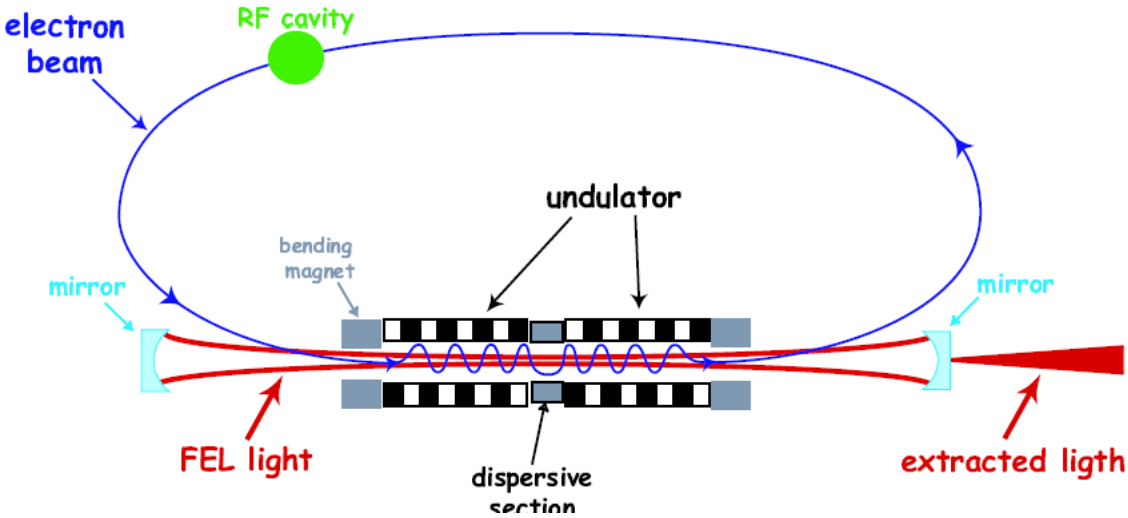

Figure 1.7: FEL oscillator on a storage ring. The radiation produced by the electrons in the undulator is stored in an optical cavity and interacts with the electron beam in the following turns. The undulator can be a single section or, as in the picture, a Klystron composed by two undulators and a dispersive section. Courtesy of F. Curbis.

1.3 Electron beam requirements

FELs operating in the VUV and X-ray regime, both in SASE and seeded configuration require a beam with high electron density in the six dimensional phase space. This requires high current, low transverse emittance and low energy spread [55, 56]. The Pierce parameter ρ, indicating the efficiency of the interaction, has typical values in the X-ray regime of $10^{-4} - 10^{-3}$ for a current of 500-3000 A. The high beam current is required to keep some efficiency and a relevant emitted power at very short wavelengths. The relative energy spread of the electron beam at saturation is $\approx \rho$. An initial relative energy spread approaching the maximum value $\approx \rho$, that occurs at saturation, greatly reduces the FEL interaction. Then, it becomes clear that a low relative energy spread of the order of 10^{-4} of the electron beam is of critical importance. The other beam parameter with a critical importance is the normalized transverse beam emittance, $\varepsilon_n = \varepsilon\gamma$, where the geometric transverse emittance ε is a measure of the transverse phase space domain occupied by the beam [57]. A limit on the geometric beam emittance for ensuring good spatial (transverse) coherence from sources of spontaneous undulator radiation was derived in [58], giving $\varepsilon_n < \frac{\lambda}{4\pi}$, where $\frac{\lambda}{4\pi}$ is the minimum phase space area for a diffraction limited photon beam. The fulfilment of this requirement is necessary to obtain a matching of light and electron beam transverse phase space, i.e. the radius and angular divergence of the electron and photon beams must be matched to provide a good overlap and interaction between photons and electrons along the undulator [59]. The above mentioned relation between geometric emittance and the radiation wavelength gives a rough rule-of-thumb estimate of the electron energy/wavelength possibilities. It shows, for example, that the minimum wavelength achievable decreases with the normalized emittance, for a given beam energy and from this relation a requirement of

a normalized emittance in the range 1–3 *mm·mrad* comes out for a FEL in the VUV and X-ray regime. Here all beam parameters are to be considered as slice parameters with a slice length given by the FEL cooperation length.

The linear accelerators designed to drive the VUV and X-ray FELs have to deliver an electron beam with very high quality. The design of most of the linacs proposed to drive VUV and X-ray FELs includes a photoinjector [60] that represents the first part of the machine to produce low emittance beam and one or more compressors to raise the beam peak current. The electrons are produced by the impact of a UV laser on a copper cathode placed in a first radio frequency (RF) cavity in which the electrons are accelerated to an energy of few *MeV* (typically 4-6 *MeV* [61]). The first part of the photoinjector composed of this first cavity is called the gun. Electrons emitted from the cathode are non-relativistic. They repel each other transversally through Coulomb forces while space charge forces are mainly longitudinal for relativistic electrons. Fast acceleration in the gun cavity is important to obtain low emittance. The gun cavity is surrounded by a solenoid that compensates Coulomb repulsion in the non-relativistic regime. Then the beam enters the following booster sections placed at a distance from the gun imposed by the emittance compensation scheme [62, 63, 64] and then the beam goes in a linear accelerator (linac) [65]. The bunch is compressed in a magnetic bunch compressor. See [66] for a review of magnetic bunch compression. Several phenomena, leading to a degradation of the beam quality can take place in the linac and in the bunch compressors. Non-linearity in beam compressors [67] and the microbunching instability [68] in the linac affect the beam longitudinal phase space leading to a degradation of the beam FEL spectral purity [69]. We will introduce bunch compression and microbunching instability in the next chapter. The accelerator scheme

described above is the one used in LCLS, FERMI, FLASH and other future FEL facilities planed or in realization [70, 71].

1.4 Improving SASE

Several ideas have been proposed and partially tested to improve the spectral purity and stability of SASE FELs. A first class of methods relies on the shaping of the longitudinal electron-beam phase space, enabling the gain only in a small longitudinal portion of the beam [72, 73], comparable to one cooperation length. In this case, the reduction of the electrons involved in the photons production leads to a relatively low output power. Another method exploits a combination of a linear variation of beam energy along the beam longitudinal coordinate (linear chirp) and a variation of the peak magnetic field (tapering) along the undulator, to help the growth of a single spike. This scheme was proposed in [74] and recently tested at SPARC [75]. Another technique to improve the spectral quality of the SASE radiation is the so called self-seeding [76]. This technique has been recently tested at LCLS [77]. The self-seeding scheme consists of a first SASE stage in which a pulse with a peak power of GW level is produced in the soft or hard X-ray regime. Then, such a pulse is used to produce a monochromatic seed for a second undulator line, tuned at the seed wavelength. The seed coming from the first stage is eventually amplified, up to saturation.

1.5 State of the art

The state of art in the field of X-ray regime and VUV light sources producing coherent radiation is represented by SASE FELs [10,11,12] operating down to the hard X-ray regime and by seeded facilities working in the VUV [13, 20-23]. SASE FEL's are capable of generating X-ray pulses ranging from hundreds down to tens of femtoseconds, allowing the direct observation of structural dynamics [78, 79]. LCLS [10] is a single-pass SASE free-electron laser driven by the SLAC linear accelerator. This light source has been in operation since 2009, generating pulses with a peak power of tens of GW. The shortest wavelength at LCLS is $1.5{\cdot}10^{-10}m$. LCLS is a SASE FEL. Therefore, the pulses are characterized by a stochastic spiking structure in time and frequency. Every pulse contains tens of such spikes. As a consequence, the coherence length is shorter than the pulse length and the pulse bandwidth is longer than that determined by the pulse length. The short pulse duration ($<$100 fs) and the high peak power per pulse (tens of GW) permits to do time resolved experiments, to study non-linear phenomena and to do diffraction of some single macro molecules like viruses [80] and enzyme [81]. FLASH [11] in Hamburg and SACLA [12] in Japan are the other facilities that use X-rays produced by FELs operating in SASE mode. FLASH reaches 1.5 nm and SACLA operates down to $0.7 \cdot 10^{-10}m$. The operations of seeded FELs were limited, before the commissioning of FERMI, down to 60 nm. These seeding experiments are performed at SPARC [22], DUV-FEL [20] and at SPring-8 [82], and at the storage ring Elettra's FEL [21]. Recently, the first commissioned FEL line of FERMI@Elettra [13], named FEL1, generated powerful FEL pulses at 20 nm, the thirteenth harmonic of the seed laser in one HGHG stage. Wavelength harmonic conversion down to the 29th harmonic [83] in a single stage cascade has been demonstrated too. The commissioning of the second FEL

line of FERMI, FEL2, has started at the end of 2012 [84]. FEL2 works in two stage HGHG scheme and uses the fresh bunch technique [59].

1.6 Thesis plan

This thesis reports some experiments devoted to improve longitudinal coherence and spectral purity and stability of VUV and X-FEL. The structure of the thesis is the following. Chapter 2 is dedicated to presenting elements of beam and FEL physics. Chapter 3 introduces the layout of the facilities in which the experiments described in this thesis are performed. In Chapter 4 we describe the commissioning of the FERMI@Elettra linac. Chapter 5 describes the results of FEL1 commissioning. Chapter 6 presents, self-seeding in the hard X-ray regime, the results of self-seeding experiments performed at LCLS and related simulations. Chapter 7 introduces a FEL scheme working with a chirped electron beam and a tapered undulator and presents the experiment done at SPARC in this configuration.

Chapter 2

Particle accelerator and FEL theory

In this chapter we introduce the basics of particle accelerator and FEL theory that will be used in the following chapters.

2.1 Electron beam dynamics

Several techniques exist to accelerate charged particles [85]. Modern linear accelerators (linacs) use radio frequency, RF cavities to accelerate particles to the final energy [65]. The RF cavities provides a longitudinal electric field, whose typical frequency is from hundreds of *MHz* up to few *GHz*. The motion of a charged particle in electromagnetic fields is governed by the Lorentz force:

$$F = e(E + v \times B) \tag{2.1}$$

where e is the particle charge, v is the particle velocity, E is the electric field and B is the magnetic field. In this thesis we will treat only electrons for which $e = e_0 = 1.609 \cdot 10^{-19} C$. The energy gain/loss for an electron passing through a cavity is:

$$\frac{dE}{dt} = e_0 V_0 sin(\omega_{rf} t + \phi) \tag{2.2}$$

where V_0 is the effective peak accelerating voltage and ϕ is the RF phase angle. In any particle accelerator a reference trajectory, on which all particles should move, exists by design. Electromagnetic guide fields are used to force the particles to move on trajectories close to the design orbit. The guide fields are typically stationary magnetic fields transverse to the direction of motion. Dipole magnets are used to bend the particles trajectory on the design orbit if this deviates from a straight path [86, 87]. These magnets define the design orbit for a reference particle with the nominal momentum p_0. Particles in the bunch with momentum p different from the nominal one are bent differently and can go far away from the designed orbit. A spread in the bunch of the initial position and momentum tends to spread the particles transversely. Transverse focusing is thus used to limit the transverse beam dimension. Focusing forces are usually provided by quadrupole magnets. Typically, the design orbit lies within a plane and all magnets are oriented in such a way that the particle motion can be decoupled in the horizontal and vertical direction. In the following we assume that the trajectory lies in the horizontal plane only [87, 88]. It is convenient to describe the motion of individual particles in terms of coordinates related to a reference particle, with nominal momentum. At any longitudinal position s along the reference trajec-

tory, the instantaneous position of a particle can be specified by the curvilinear-orthogonal coordinates (x, y, s). The horizontal and vertical displacements with respect to the design orbit are then perpendicular to the tangent at the design orbit and are specified by the corresponding coordinates x and y in a local right-handed rectangular coordinate system as shown in figure 2.1a. The dipoles are rectangular magnets. Their longitudinal axes are parallel to the longitudinal axis of the incoming beam. We consider dipoles with poles flat and parallel to the horizontal plane. The magnetic field of these dipoles, B_y, is homogeneous and directed along the vertical axis. The geometrical relationship between the trajectory parameters inside the dipole are shown in figure 2.1b.

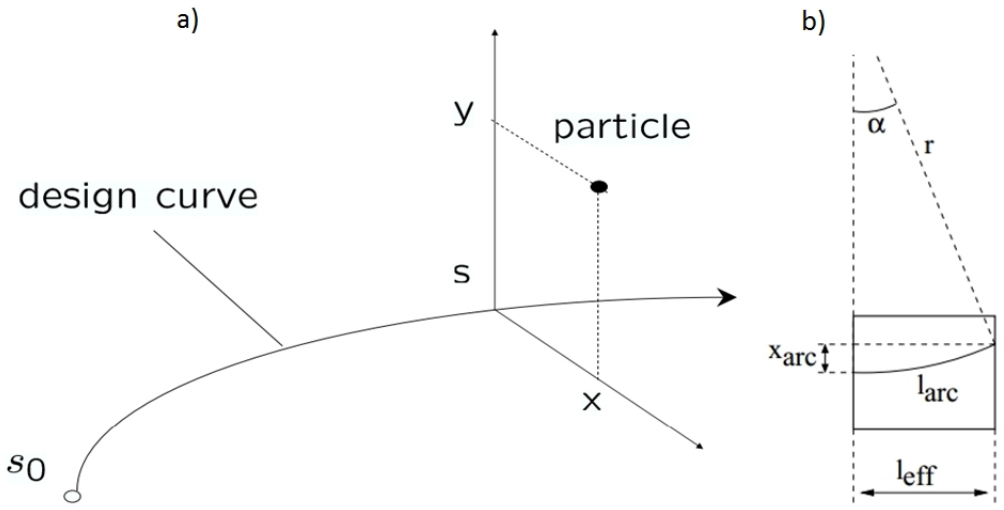

Figure 2.1: a: Design orbit and coordinate system. Taken from [87]. b: Trajectory in a dipole. Taken from [88].

The general equation of motion for an electron, choosing s as the independent coordinate and retaining only terms up to the first order in the dependent variable, with a momentum slightly deviating from the nominal is [86]:

$$\frac{d^2x}{ds^2} = -K_x(s)x + \frac{\delta}{\rho(s)} = p_0(1+\delta) \tag{2.3}$$

where, terms of second and higher order in (x, y, δ) are neglected. Here $\rho\,(s)$ is the local bending radius at the position s along the beam trajectory [86]. These equations describe the focusing of electrons in the linear approximation. They are examples of Hill's differential equation [89]. A proper arrangement of alternating quadrupole fields is required to keep particles close to the design trajectory simultaneously in both transverse planes [86]. The function K_x(s) is piecewise assuming a specific value in any magnet sections. The solutions of Hill's equation can be assembled from local solutions by means of transfer matrices. The general solution of the homogeneous Hill's equation and its derivative can be expressed, within an interval $s0 \leq s \leq L$, in terms of linearly independent solutions u1(s) and u2(s):

$$\frac{d^2x}{ds^2} = -K_x(s)x; \quad x(s) = a_1u_1(s) + a_2u_2(s); \quad x^{'}(s) = a_1u_1^{'}(s) + a_2u_2^{'}(s) \tag{2.4}$$

we can express the equations 2.4 in matrix form:

$$X(s) = \begin{bmatrix} x(s) \\ x^{'}(s) \end{bmatrix}; \; X(s) = U(s)A; \quad U(s) = \begin{bmatrix} u_1(s) & u_2(s) \\ u_1^{'}(s) & u_2^{'}(s) \end{bmatrix}; \quad A = \begin{bmatrix} a_1 \\ a_2 \end{bmatrix} \tag{2.5}$$

The matrix equation, yielding a representation of the general solution in terms of the initial

conditions X(s0) at s0, can be expressed as:

$$X(s) = M_x(s, s_0)X(s_0);\ M(s_n, s_0) = M(s_n s_{n-1}) \cdot .....M(s_1, s_0) \tag{2.6}$$

Where M is the transfer matrix. A similar formalism is applied to the y plane. The transfer matrix can be written in the following way:

$$M(S, S_0) = \begin{bmatrix} C(S) & S(S) \\ C'(S) & S'(S) \end{bmatrix} \tag{2.7}$$

where C and S are the cosine like and sine like solution of Hill's equation satisfying the relations:

$$C(s_0) = 1;\ C'(s_0) = 0;\ S(s_0) = 0;\ S'(s_0) = 1 \tag{2.8}$$

In general the matrices M_x and M_y have a different shape in any specific magnetic element. The representation 2.6 of the general solution of the Hill's equation is very useful in accelerator physics, since the function K(s) is typically piecewise constant to a very good approximation. The equation of motion can thus be solved locally yielding transfer matrices for the single intervals in which K_x(s) is constant, specifying a particular lattice component such as a quadruple or a dipole and the general solution can be calculated by matrix multiplication as indicated by the second identity in 2.6. A solution of the inhomogeneous equation 2.4 can be found by using Green's functions, yielding a particular solution $\delta \cdot \eta$(s) with [57, 90]:

$$\eta(s) = S(s)\int_{s_0}^{s}\frac{C(t)}{\rho(t)}dt - C(s)\int_{s_0}^{s}\frac{S(t)}{\rho(t)}dt \tag{2.9}$$

Physically, $\delta \cdot \eta(s)$ is the horizontal offset of an electron with relative momentum deviation δ from the design orbit at s, provided the electron was moving on the design orbit in a small interval around s_0. The function $\eta(s)$ is called the momentum dispersion function. The general solution of the inhomogeneous equation can be expressed using again matrix notation:

$$\begin{bmatrix} x(s) \\ x'(s) \\ \delta \end{bmatrix} = \begin{bmatrix} C(s) & S(s) & \eta(s) \\ C'(s) & S'(s) & \eta'(s) \\ 0 & 0 & 1 \end{bmatrix} \begin{bmatrix} x(s) \\ x'(s) \\ \delta \end{bmatrix} \tag{2.10}$$

The equation is referred to the x plane. It is possible to extend the matrix formulation to the two planes and include even the longitudinal motion. To this end the particle can be represented by a vector $\overline{X}(\bar{x})$ where $\bar{x} = [x,\, x',\, y,\, y',\, z,\, \delta]$ and z is the longitudinal position within the bunch relative to the beam centroid (z=0). We write the matrix equation of the particles in the bunch in the six dimension phase space making some simplifications. Assuming that the beam trajectory lies in the horizontal plane allows us to decouple the motion in the two transverse planes and so to simplify the equations by setting those term to zero in the matrix R that couple the two planes and the terms that couple energy into vertical plane. For a transfer line in which RF cavities are absent the equation can be

further simplified to assume the form:

$$\bar{X}(s) = \begin{bmatrix} R_{11} & R_{12} & 0 & 0 & 0 & R_{16} \\ R_{21} & R_{22} & 0 & 0 & 0 & R_{26} \\ 0 & 0 & R_{33} & R_{34} & 0 & 0 \\ 0 & 0 & R_{43} & R_{44} & 0 & 0 \\ R_{51} & R_{52} & R_{53} & R_{54} & 1 & R_{56} \\ 0 & 0 & 0 & 0 & 0 & 1 \end{bmatrix} \bar{X}(s_0) \quad \overline{X}(s) = \begin{bmatrix} x \\ x' \\ y \\ y' \\ z \\ \delta \end{bmatrix} \tag{2.11}$$

Any element R_{ij} of matrix R for a particular lattice component indicates the influence of the value assumed by the coordinate j at the start of the element, on the coordinate i at the end of the element. For example particles with different energy move on different paths in a layout element in which $R_{56} \neq 0$. Their longitudinal separation, if the other coordinates are the same for the two particle and at the first order in the energy separation, evolves in this way:

$$\triangle_z^{'} = \triangle_z + R_{56} \cdot \triangle_E \tag{2.12}$$

where $\Delta_z^{'}$, Δ_z, and $\Delta_E^{'}$ are the particle longitudinal separation before the element, after the element and the relative energy separation of the two particles respectively. The general solution of the homogeneous Hill's equation can be expressed in the phase-amplitude form [87]:

$$x(s) = \sqrt{a_x \beta_x(s)} cos(\phi_x(s) + \phi_{x,0}) \tag{2.13}$$

where $\beta_{x,y}(s)$ and $\phi_{x,y}(s)$ are the betatron and the phase function, while $a_{x,y}(s)$ and $\phi_{x,y,1}$ are real constants specifying the particular solution, and the betatron phase. The beta function in a given accelerator completely describes the lateral focusing properties of the guide field and the significant characteristics of the particle trajectories. The maximum displacement of a particle from the design orbit at position s in the x and y planes are $\sqrt{a_x \beta(s)}$ and $\sqrt{a_y \beta_y(s)}$. The phase-amplitude solution allows an instructive interpretation, which can be seen by combining x(s) and $x'(s)$ according to [87]:

$$\gamma_x x^2 + 2\alpha x x^{'} + \beta_x x^{'2} = a_x \qquad \gamma_y y^2 + 2\alpha y y^{'} + \beta_y y^{'2} = a_y \tag{2.14}$$

Equation 2.14 defines an ellipse in the coordinates space $(x, x^{'})$ centred at$(x, x^{'}) = (0, 0)$ and with area $\pi a_{x,y}$. The particle motion can thus be interpreted as a movement on an ellipse in phase space, whose shape varies along the accelerator according to the corresponding transfer matrices while its area remains constant. The interpretation of the particle motion in terms of a transforming ellipse in phase space is particularly helpful for describing the development of an electron distribution ϱ(x, x') under the linear dynamics described above. Since the dynamics of a single electron is determined by its phase space coordinates (x, x'), every electron within a certain phase space area will stay within this area if the boundary is transformed according to the equation of motion. Since an elliptical area with centre (0, 0) remains elliptical as shown above, the transformation of a few ellipse parameters

is suited to describe the envelope of an electron ensemble in coordinate space. Because of its importance the parameter a is called the Courant-Snyder invariant. The relation of Courant-Snyder parameters to the ellipse geometry is sketched in figure 2.2 [86].

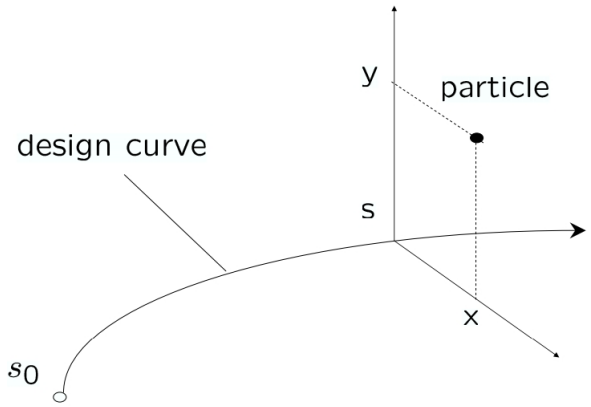

Figure 2.2: Beam in x-x' space and Courant-Snyder parameters. Taken from [87].

The evolution of the electron beam distribution can be described by means of the following covariance matrix evolving from an initial point s_0 to a final point s_1 according to the matrix formalism:

$$\sigma_x = \begin{bmatrix} \langle x^2 \rangle & \langle xx' \rangle \\ \langle xx' \rangle & \langle x'^2 \rangle \end{bmatrix} \qquad \sigma_x(s) = M_x \sigma_x(s_0) M_x^T \tag{2.15}$$

where we have indicated with $\langle x \rangle$and $\langle x^2 \rangle$ the first and second moment of the beam distribution. The following relation can be demostrated [90]:

$$\epsilon_x \beta_x(s) = \left\langle (x(s))^2 \right\rangle \qquad \epsilon_y \beta_y(s) = \left\langle (y(s))^2 \right\rangle \tag{2.16}$$

where the ϵ_x, called geometric emittance [90], is defined as:

$$\epsilon_x = \sqrt{det(\sigma_x)} = \sqrt{\langle x^2 \rangle \langle x'^2 \rangle - \langle x x' \rangle^2} \tag{2.17}$$

is called the geometric emittance [90]. Emittance has the units of length and represents the area (root mea square, RMS) occupied by the beam in the x-x' space. The quantities $\left\langle (x(s))^2 \right\rangle$, corresponding to the element$(\sigma_x)_{1,1}$ of the covariance matrix, can be obtained observing the bunch images at one screen and measuring the RMS size of the beam. Then the product of beam emittance and the beta function at one point is determined. It is possible to recover the Twiss parameters α_x, β_x and γ_x and the emittance at the point s_0, if it is the initial point of a quadrupole and if a screen for transverse measurements is placed in the point s. The technique used to accomplish this is the quadrupole scan [90] and it consists of measuring the beam size of the electron distribution on the screen as a function of the quadrupole field strength for at least three different quadrupole settings.

A simple application of bending magnets is represented by beam energy spectrometer lines in which the beam energy distribution is characterized by analyzing the transverse profile collected on a screen, in the bending plane. Particles with different energy follow different trajectories in the spectrometer dipole. The horizontal dimension of the beam on the screen is:

$$\sigma_x = \sqrt{(\sigma_x)^2_{Twiss} + \left(\eta \frac{\sigma_\gamma}{\gamma_0}\right)^2}; \quad (\sigma_x)_{Twiss} = \sqrt{\frac{\beta_x \epsilon_{x,n}}{\gamma}} \tag{2.18}$$

A measurement of σ_x, when all the other quantities entering in the equation are known or estimated, yields a value for the slice energy spread. The mean energy γ is obtained from the value of the magnetic field of the bending magnet that is needed to bring the beam on the reference trajectory to the centre of the screen. The values of $(\sigma_x)_{Twiss}$ and η can be calculated by the magnetic machine lattice and beam emittance. The value of the dispersion η at screen location can be measured changing the beam energy and measuring the change of the beam position on the screen. A first value of the energy spread can be obtained neglecting the Twiss beam size and considering the measured beam size as the pure chromatic one:

$$(\sigma_\gamma)_{Chromatic} = \gamma_0 \frac{\sigma_x}{\eta} \tag{2.19}$$

On the other hand even a beam with zero energy spread has a finite beam size on the screen due to beam emittance and to the size of the pixels composing its image. In analogy with equation 2.20 we can define these two contributions to the measured energy spread derived from the Twiss parameters and pixel size:

$$(\sigma_\gamma)_{Twiss} = \gamma_0 \frac{(\sigma_x)_{Twiss}}{\eta} \;\; (\sigma_\gamma)_{pixel} = \gamma_0 \frac{\Delta_{pixel}}{\eta} \tag{2.20}$$

The energy spread terms $(\sigma_\gamma)_{pixel}$ and $(\sigma_\gamma)_{Twiss}$ indicate the screen resolution and the lattice resolution. A better estimate of energy spread can be obtained subtracting in quadrature $(\sigma_\gamma)_{pixel}$ and $(\sigma_\gamma)_{Twiss}$ from $(\sigma_\gamma)_{Chromatic}$. Spectrometers have to be designed in order to

maximize the dispersion and minimize the beam Twiss dimension on the screen. This permits to maximize the pure chromatic dimension on the screen and to minimize $(\sigma_\gamma)_{Pixel}$ and $(\sigma_\gamma)_{Twiss}$.

2.2 Magnetic bunch length compression

Magnetic bunch length compression is carried out via ballistic contraction of the particles path length in a magnetic chicane. The linac located upstream of the magnetic chicane is run off-crest to establish a correlation between the particle energy deviation with respect to the reference particle and the z coordinate along the bunch. More precisely, the linac phase is adjusted so that the bunch head has a lower energy than the tail. The leading particles travel, in the magnetic chicane, on a longer path than the trailing particles due to their lower energy. Since all particles of the ultra-relativistic beam travel in practice at the speed of light, the bunch edges approach the centroid position and the total bunch length is finally reduced. Figure 2.3 shows the concept design of magnetic bunch compression. In the following, we choose a longitudinal coordinate system such that the head of the bunch is at z<0.

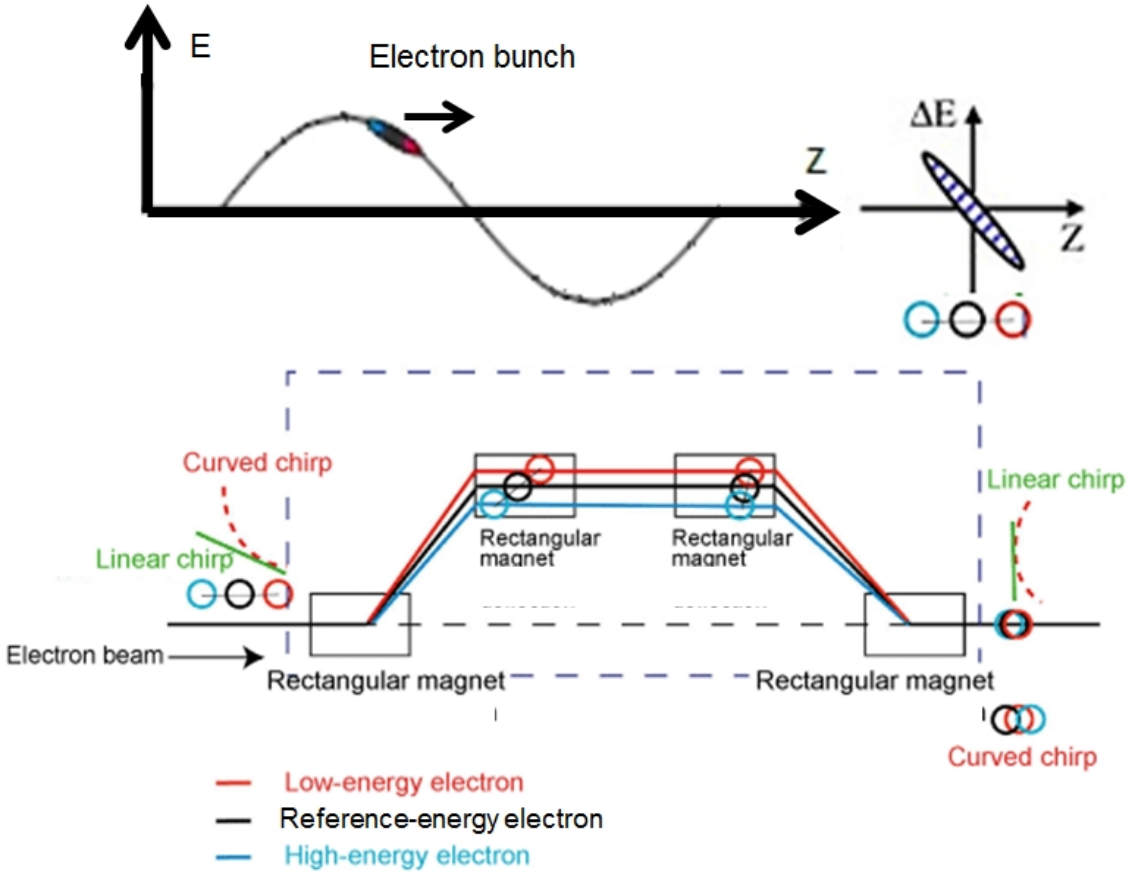

Figure 2.3: Schematic of magnetic bunch length compression by a four dipole symmetric chicane. On the top, the energy manipulation of the bunch, done before the bunch compressor, is shown. The electron beam is accelerated off crest to impose an energy position correlation along the bunch. The head of the bunch has a lower energy with respect to the tail. The head of the bunch is at z<0 as shown on the top of the picture. The dynamics of the beam in the chicane is shown at the bottom of the picture. The head of the bunch is deflected more by the four dipoles and then travels, in the chicane, on a longer path. The head of the bunch is delayed with respect to the tail and then the beam is compressed linearly. Taken from http://www.spring8.or.jp/en/news_publications/press_release/2009/090826/

In the first approximation we can assume a linear dependence of the particle path lengths on the coordinate $\delta = \frac{\delta_\gamma}{\gamma_0}$ as described by the element of the linear transfer matrix $R_{56} = \frac{\partial z}{\partial \frac{\delta_\gamma}{\gamma_0}}$.

The position occupied by a particle in the beam is modified in the following way where z_i and z_f are the particle's position in the bunch respectively before and after the chicane:

$$z_f = z_i + R_{56}\frac{\delta_\gamma}{\gamma_0};\ R_{56} \approx -2\theta^2\left(d + \frac{2}{3}l_{eff}\right) \tag{2.21}$$

where θ is the deflection angle of any of the four magnet, d is the distance between the first and the second magnet and between the third and the fourth magnet and l_{eff} is the magnetic length of any of the fourth magnets. Also $\frac{\delta\gamma}{\gamma_0}$ can be expanded up to the 1^{st} order:

$$\frac{\delta\gamma}{\gamma_0} = hz \tag{2.22}$$

A linac with energy gain $E = eV \cdot sin\,(\phi)$ where V and ϕ are the peak accelerating voltage and accelerating phase, imparts to the beam the following linear energy chirp:

$$h = \frac{d\frac{\delta\gamma}{\gamma_0}}{dz} = \frac{2\pi}{\lambda_{RF}}\frac{e_0 V cos\,(\phi)}{E_0 + e_0 V sin\,(\phi)} \tag{2.23}$$

where E_0 is the energy before the linac and λ_{RF} is the RF wavelength. The RMS bunch length after compression is obtained, in the linear approximation, by substituting equations 2.22 and 2.23 into equation 2.21:

$$\sigma_z = \left\langle z^2 - \langle z\rangle^2\right\rangle \approx \sigma_{z_0}\left(1 + h \cdot R_{56}\right);\ \ CF = \frac{1}{1 + h \cdot R_{56}} \tag{2.24}$$

where σ_{z_0} is the RMS bunch length before compression. The ratio between initial and final bunch length, CF, is called compression factor. The peak beam current after compression

is then I= $CF \cdot I_0$ where I_0 is the initial beam current. The beam is compressed for CF>1 and it implies $h \cdot R_{56} < 0$. R_{56} is negative, as seen by equation 2.24, and a positive chirp is needed to compress the beam.

Up to now we are considering bunch compression in the linear approximation, assuming that the compression process is linear in z and in ρ. In this approximation the difference between the longitudinal position of a particle in the bunch before and after the chicane is linear in z, $z_f - z_i = R_{56}hz$, then any point of the beam is compressed by the same factor as $\frac{d(z_f - z_i)}{dz} = R_{56}h$. This means that, in the limits of validity of this approximation, the bunch shape is preserved while the bunch length is compressed. In this limit it is possible to obtain a flat current profile simply starting from a flat current distribution at the linac entrance. A flat current is important, in a seeded and self-seeded scheme, to have a flat FEL gain profile along the bunch preserving the Gaussian shape of the seed and then permitting a FEL output pulse with a spectrum bandwidth close to the Fourier limit. In the real case, second order terms are present in the path-length energy dependence of the chicane transport matrix and in the electron energy-bunch position relation (second order chirp) as the RF acceleration is governed by the sine function of the RF phase. The transformation of the bunch longitudinal coordinate through the magnetic chicane and the quantity $\frac{\delta\gamma}{\gamma_0}$ at 2nd order are:

$$z_f = z_i + R_{56}\frac{\delta_\gamma}{\gamma_0} + T_{566}\left(\frac{\delta_\gamma}{\gamma_0}\right)^2; T \approx -\frac{3}{2}R_{56}; \tag{2.25}$$

$$\frac{\delta\gamma}{\gamma_0} = hz + h'z^2 \; h' = \frac{d\left(\frac{\delta\gamma}{\gamma_0}\right)^2}{dz^2}; \; h^{'} = \frac{1}{2}\frac{dh}{dz} = -\left(\frac{2\pi}{\lambda_{RF}}\right)^2 \frac{e_0 V sin\phi}{E_0 + e_0 V sin\phi} \tag{2.26}$$

where T_{566} is the term of the chicane transport matrix with a second order dependence in energy. It derives from equations in 2.25 and 2.26 that non-linear terms in energy-position correlation and in the chicane transfer matrix are negligible for small compression factor, CF<3. It can be found that the coupling between second order terms in the energy-position bunch correlation and the chicane second order path-length dependence from the particle energy leads to a non-linear compression for a linear compression factor greater than 3 [91]. In this regime, the difference between the longitudinal position of a particle in the bunch before and after the chicane is no longer linear in z, as can be seen by equations in 2.25 and 2.26. Accordingly, the compression is not constant along the beam and this produces a less homogeneous beam distribution, with formation of current spikes at the edges of the electron bunch. An electron beam distribution as uniform as possible provides the maximum peak current in the main body of the bunch and this improves the FEL gain and the photon flux. Limitation of the current spikes derived by non-linearity in the beam compression is important, both for seeded and SASE scheme to avoid the strong longitudinal wake fields that can disrupt beam phase space as the beam travels along the high energy linac section and the long undulator vacuum chamber usually characterized by a small gap and a high impedance. The use of a short RF accelerating cavity, operated at a higher harmonic of the linac RF frequency [92, 93], is usually adopted in order to linearize the 2nd order bunch length transformation thereby maintaining the initial temporal bunch profile. In section 4

experimental results of beam compression in FERMI bunch compressor are presented.

2.3 Microbunching in high brightness electron beam

The very bright electron beam required to drive VUV and X-ray FELs is susceptible to a microbunching instability [68] that produces energy and current modulations [94-98] at short wavelengths ($\approx 1 - 5\ \mu m$). This collective instability takes place as linacs for FEL light sources are equipped with bunch compressors designed to increase the peak current to the level required for photon production. The microbunching instability was first foreseen in [94] as a klystron-like mechanism of amplification of density modulations, characterized by some modulation periods, in an electron bunch compressed via a magnetic chicane. The microbunching instability is presumed to start at the photoinjector exit growing from a pure density and/or energy modulation caused by shot noise and/or unwanted modulations in the photoinjector laser temporal profile. As the electron beam travels along the linac to reach the first bunch compressor (BC1), the density modulation leads to an energy modulation via (LSC). The resultant energy modulations are then transformed into higher density modulations by the bunch compressor. This increased current modulation leads to further energy modulations in the rest of the linac. Coherent synchrotron radiation in the bunch compressor can also contribute to enhance the energy and density modulations and can even increase the beam emittance [99, 100]. The modulations caused by the photocathode laser temporal profile have usually a period of hundreds of microns [101] while shot noise spectrum has a white noise distribution and then some modulations are present even at shorter wavelengths. Several studies [102-104] indicate that shot noise density modulations at the

photocathode exit have amplitudes that can reach 0.01% while the modulations caused by the laser modulation can reach ≈ 1. The presence, in the beam current distribution, of a modulation with a specific period corresponds to a non-zero value of the bunching factor at the corresponding wave vector: $b(k) = \frac{1}{Nec}\int I(z)\, e^{-kz} dz$ [95]. The bunching factor associated with the shot noise can be estimated by the following formula $b(k) = \sqrt{\frac{kec}{I_b 2\pi}}$ [105]. The model for microbunching instability predicts that the beam, going into the bunch compressor, gets energy modulations along the linac via the action of the longitudinal space charge (LSC) coupled with the initial current density modulations. The LSC action can be described by a longitudinal impedance model. The beam with a bunching factor b'(k) gains an amplitude modulation given, in gamma units, by [95]:

$$\Delta_m(k) = -\frac{I 4\pi b'(k)}{Z_0 I_A}\int_0^L Z(k,s) ds \tag{2.27}$$

The integral is from the beginning of the linac ($\approx 100 MeV$) to the bunch compressor location and L is the length of this part of the linac in which energy modulations are accumulated starting from the initial density modulations. Both shot noise and laser modulations have characteristic scales shorter than the uncompressed bunch length. Thus they can be a driving term for space charge energy modulations. The expression of the longitudinal space charge impedance is $Z(k) = \frac{4iZ_0}{kr_b^2} l \left[1 - \frac{kr_b}{\gamma} K_1\left(\frac{kr_b}{\gamma}\right)\right]$. The distribution function in the longitudinal phase space of the beam has the following form in front of the bunch compressor [95]:

$$f_0(z', \delta_\gamma) = f_0(z', \delta - hz' - \delta_m(z')) \tag{2.28}$$

where z is the longitudinal coordinate in the bunch, δ is the relative deviation $\frac{\Delta\gamma}{\gamma_0}$ from the nominal beam energy γ_0, h is the linear chirp used to compress the beam, $\delta_m(k) = \Delta_m(k)/\gamma_0$ is the relative amplitude of the energy modulation gained by the beam via LSC in the linac, $f_0(z', \delta' = \Delta\gamma'/\gamma_0)$ is the initial longitudinal distribution, z' and $\delta'$are the longitudinal and energy coordinates of a particle in the beam before compression. Equation 2.28 describes the beam distribution function before the bunch compressor. The action of the compressor is described by the change of variable $z = z' + R_{56}[\delta' + hz' + \delta_m(z')]$. Thus, the energy modulation is converted into an additional density modulation at a compressed wave number $k_f = CF \cdot k$ given by:

$$b_f(k_f) = \int dz d\delta f(z, \delta) e^{-ik_f} = \int dz' d\delta' f_0(z', \delta') e^{-ik_f z' - ik_f R_{56}\left[\delta' + hz' + \delta_m(z')\right]} \tag{2.29}$$

Now we use the linear approximation valid for small energy modulations such as $|kR_{56}\delta_m| << 1$ and we expand 2.29 as:

$$b_f(k_f) = [b'(k) - ik_f R_{56}] \int d\delta' V(\delta') e^{-ik_f R_{56}\delta'} \tag{2.30}$$

When the initial density modulation can be neglected with respect to the chicane contribution, as the first term in 2.30 can be neglected and the instability is said to be in the "high-gain regime". Now we express, in the high-gain regime, the gain in the density modu-

lation after the first bunch compressor that is given by the ratio of the final over the initial bunching [95]:

$$G(k) = |\frac{b_f}{b'}| \approx \frac{I_0}{\gamma I_A}|k_f R_{56} \frac{\Delta_\gamma(k)}{\gamma_{compressor}}| \int d\delta' V(\delta') e^{-ik_f R_{56}\delta'}. \tag{2.31}$$

The gain assumes the following expression when the initial energy distribution is Gaussian:

$$G(k) = |\frac{b_f}{b'}| \approx \frac{I_0}{\gamma I_A}|k_f R_{56} \frac{\Delta_m(k)}{\gamma_{compressor}}| exp\left(-\frac{1}{2}k_f^2 R_{56}^2 \frac{\sigma_\gamma^2}{\gamma_{compressor}^2}\right) \tag{2.32}$$

Now we use the nominal parameters from the FERMI@Elettra conceptual design report (CDR) [24] to calculate microbunching effects in one concrete example. The beam has a charge of 800 pC, it is compressed by a factor 10 in a bunch compressor located at an energy of 270 MeV with $R_{56} = -41\,mm$. Then the beam is accelerated to the final energy of 1.2 GeV. The initial slice energy spread coming from the photoinjector, indicated as σ_γ^2 in the equation 2-32, is 3 keV. For this calculation we use only shot noise as a source of the initial density modulation. The density modulation gain curve obtained by equation 2.32 is shown in figure 2.4a. The blue curve is obtained for a Gaussian energy spread of 3 keV. The other curves in 2.4 are obtained for higher values of the initial energy spread. The expression for the microbunching gain in the linear regime contains two terms. The first one represents the conversion of energy modulation into density modulation for a zero energy spread beam, while the exponential term in equation 2.32 represents the combined action of slice energy spread and R_{56} in the bunch compressor. The first term is inversely proportional to the modulation wavelength. The second term goes from zero to one for

increasing modulation wavelengths. Modulations too short are smeared out by the combined action of slice energy spread and R_{56} in the bunch compressor and then the gain is small at short wavelengths. Longer modulation wavelengths are more resistant to the smearing in the bunch compressor but the first term of equation reduces the gain as the spatial period of the modulations becomes longer and longer. The gain curve presents a maximum and a band of amplified wavelengths as the two terms in equation 2.32 have opposite behaviours with respect to the modulation wave vector. The bunching spectrum of the compressed beam can be obtained from the gain curve and the initial bunching spectrum using the high-gain approximation $G\left(k_i\right) \approx |\frac{b_{ind}(k_f)}{b_i(k_i)}|$. The current modulations obtained by the beam during bunch compression leads to further energy modulations in the rest of the linac via longitudinal space charge. In figure 2.4b we illustrate the spectrum of amplitude energy modulations accumulated at the end of the linac calculated with the equations 2.27 and 2.32 starting from shot noise. The energy modulation spectrum shows a resonant behaviour as the gain curve has a maximum and a band of amplified wavelengths.

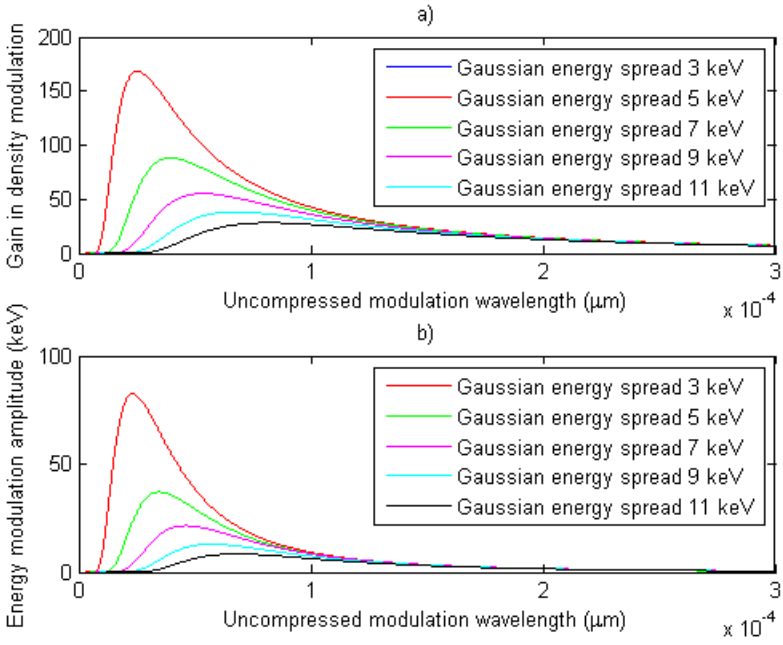

Figure 2.4: a: Gain curve of FERMI@Elettra linac in the compressor scheme for several values of the initial slice energy spread. The horizontal axis is the compressed modulation wavelength. b: Energy modulations spectrum at the end of the linac.

Now we suppose that all these energy modulations are converted into uncorrelated energy spread and we calculate the slice energy spread induced in the beam at the end of the linac by microbunching, in the linear approximation regime, convolving the spectral power density of the initial shot noise with the gain curve calculated above [95]:

$$\sigma_\gamma^2 = \frac{1}{2}\int \frac{d\triangle_\gamma{}^2(\lambda)}{d\lambda} d\lambda \tag{2.33}$$

The total beam slice energy spread at the end of the linac is obtained by summing in

quadrature the energy spread given by the natural beam energy spread multiplied by the compression factor that is applied to the bunch along the linac. We obtain a total slice energy spread of 115 keV. The microbunching instability can take place because the beam coming from the photoinjector is very cold [95, 102]. The exponential term in the expression for the density modulation gain shows that the particle longitudinal phase mixing contributes to the suppression of the instability if the initial uncorrelated relative energy spread $\frac{\sigma_\gamma}{\gamma}$ is sufficiently large with respect to the relative energy modulation amplitude $\frac{\Delta_\gamma}{\gamma}$. In the case of non-reversible particle mixing in the longitudinal phase space (total suppression of the instability), this damping mechanism is called energy Landau damping. Figure 2.4a shows, as seen before, the gain curve, obtained from equation 2.32, for several values of energy spread, considering a Gaussian energy distribution. It is evident that an uncorrelated energy spread higher that the natural one coming from the photoinjector effectively reduces the microbunching gain. For this reason, a laser heater has been proposed to cure and control microbunching instability in the linacs projected to drive VUV and X-ray FELs [95, 106, 107]. This device can add a small controlled amount of energy spread to the electron beam in order to reduce the microbunching instability through Landau damping in the bunch compressor [95, 106]. The laser heater consists of a short permanent magnet planar undulator located in a small magnetic chicane through which an external laser pulse is superimposed to the electron beam. The resulting interaction within the undulator produces a modulation of the mean electron beam energy on the scale of the optical wavelength λ_L. The mean beam energy, after the undulator has then the following variation with respect to the beam longitude coordinate z:

$$E(z) = E_0 + \triangle\gamma_L sin\left(k_L z + \phi_0\right) \tag{2.34}$$

where E_0 and ϕ_0 are the central beam energy and the phase between the laser and the electron beam. The transverse dynamics in the last half of the chicane time-smears the energy modulation leaving only an effective energy spread increase [95, 106]. The electron distribution is modified by the laser electron interaction in the undulator. Assuming initially Gaussian distributions in energy and in the transverse coordinates, the electron distribution function becomes [95]:

$$f_0(z, \delta_\gamma, r) = \frac{I_0}{ec\sqrt{2\pi}\sigma_\gamma} exp\{-\frac{\left[\delta\gamma - \triangle\gamma_L(r) sin\left(k_L z\right)\right]^2}{2\sigma_{\gamma_0}^2}\}\frac{1}{2\pi} exp(-\frac{r^2}{2\sigma_x^2}) \tag{2.35}$$

where $k_L = \frac{2\pi}{\lambda_L}$, and $\sigma_x = \sigma_y$ is the RMS electron beam size in the transverse plane and r is the radial coordinate. The amplitude of the FEL energy modulation$\triangle\gamma_L(r)$ for a fundamental Gaussian mode laser co-propagating with a round electron beam at the energy in an undulator of length L_U, which is short compared to both the Rayleigh length of the laser and the beta functions $\beta_{x,y}$ of the electrons is [95]:

$$\triangle\gamma_L(r) = \sqrt{\frac{P_L}{P_0}}\frac{KL_U}{\sigma_r\gamma_0} JJ(K) exp(-\frac{r^2}{4\sigma_r^2}); \quad JJ(K) = J_0(\frac{K^2}{4+2K^2}) - J_1\left(\frac{K^2}{4+2K^2}\right) \tag{2.36}$$

where $P_0 = 8.7\,GW$, P_L is the laser power and K is the undulator parameter defined by 1.5. Integrating the distribution function in 2.35 over the transverse and longitudinal coordinates, we obtain the modified energy distribution [95]:

Parameter	Vlaue
Electron beam energy	97 Mev
Electron beam size	130 μm
Laser wavelength	783 nm
Laser beam size	620 (130) μm
Laser peak power	780 (32) μJ

Table 2.1: Laser heater parameters. Laser parameters in brackets are referred to the case in which the laser and the electron beam transverse sizes are matched.

$$V(\delta_\gamma) = \int r dr \cdot exp(-\frac{r^2}{2\sigma_x^2}) \int \frac{d\xi}{\sqrt{\triangle\gamma_L(r)^2 - (\delta\gamma - \xi)^2}} \cdot exp\left(-\frac{\xi^2}{2\sigma_{\gamma_0}^2}\right) \tag{2.37}$$

From the distribution 2.37 we obtain the RMS beam energy spread that is [108]:

$$\sigma_\gamma = \sqrt{(\sigma_{\gamma_0})^2 + \frac{\sigma_r^2}{2(\sigma_r^2 + \sigma_x^2)} (\triangle_L(0))^2} \tag{2.38}$$

where $\triangle_L(0)$ is the on axis amplitude of the laser modulation. The total slice energy spread is the sum of the initial energy spread and of the energy spread coming from the laser heater action. We plot the energy distribution given by the equation 2.37 using laser heater parameters from table 2.1, in figure 2.5 for $\sigma_r > \sigma_x$ (when the laser spot size is much larger than the electron beam size, red curve) and $\sigma_r \approx \sigma_x$ (when the laser spot size is matched to the e-beam size, blue curve).

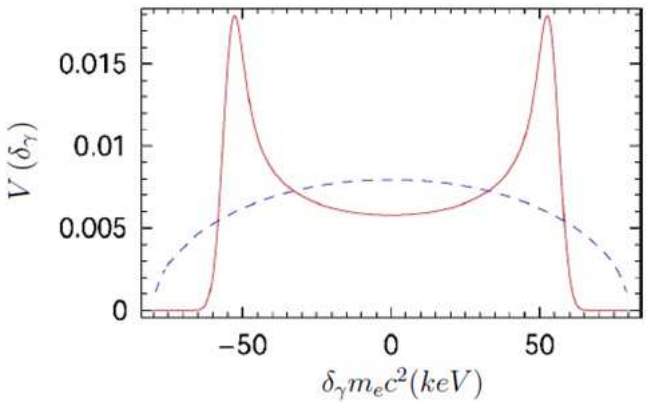

Figure 2.5: Electron energy distribution after the laser heater for a larger laser spot (blue dashed curve) and for a matched laser spot (red solid curve). The laser powers are given in table 2.1.

When the spot size is much larger than the size of the electron beam the amplitude of the energy modulation is almost the same for all electrons and the energy profile is a double horn distribution. In this case Landau damping is not very effective because the two peaks in the energy distribution are well separated and act like two different electron beam populations, reducing the mixing. On the other hand when the laser profile matches the transverse dimension of the electron beam the energy modulation changes a lot across the transverse profile of the electron beam. The resulting energy distribution is more uniform and the mixing in the bunch compressor is more effective, reducing the microbunching gain. It is possible to derive the expression for the gain of the bunching in the bunch compressor for the beam heated by the laser heater [95] by inserting expression 2.36 and 2.37 in expression 2.31:

$$G(k) = |\frac{b_f}{b'}| \approx \frac{I_0}{\gamma I_A}|k_f R_{56}\frac{\Delta_m(k)}{\gamma_{compressor}}|S_L(A,B)\, exp\left(-\frac{1}{2}k_f^2 R_{56}^2 \frac{\sigma_\gamma^2}{\gamma_{compressor}^2}\right) \quad (2.39)$$

$$S_L(A,B) = \int RdR \cdot exp\left(-\frac{R^2}{2}\right) J_0\left[A \cdot exp\left(-\frac{R^2}{4B^2}\right)\right]; A = R_{56}k_f\frac{\triangle_L}{\gamma_0}; B = \frac{\sigma_r}{\sigma_x} \quad (2.40)$$

The energy spread σ_γ in equation 2.39 is the natural one coming from the photoinjector and has a value of about 3 *keV*. We see that the maximum suppression is obtained when the laser dimension matches that of the electron beam. For any value of the slice energy spread added by the laser heater, taking B=1, we can calculate the final value of the slice energy spread at the FERMI linac end. The result is plotted in figure 2.5a. The final energy spread is determined by the microbunching and by Liouville's theorem that states that the area in the phase space is conserved. A compression by the factor CF of the bunch length produces a growth of the initial energy spread proportional to the compression factor.

The Landau damping in the bunch compressor is not effective for a too small energy spread and this produces an increase of the final slice energy spread. Increasing the initial energy spread reduces the microbunching and the final slice energy spread. For a certain value of initial energy spread the microbunchig instability is switched off and then the final energy spread, dominated by Liouville theorem, is proportional to the initial energy spread. The curve in figure 2.6a is only an approximation of the energy spread induced by micobunching as we have used a linear model of longitudinal space charge ignoring the contribution of the coherent synchrotron radiation (CSR) in the bunch compressor. The results obtained

working with the linear model can be improved by a numerical multi-particle code and numerical Vlasov solver. Figure 2.6b shows the energy spread at the linac end as a function of the initial energy spread compressing the beam with one or two bunch compressors. The two curves are referring to a bunch of 800 pC compressed by a factor 10 with one or two compressors.

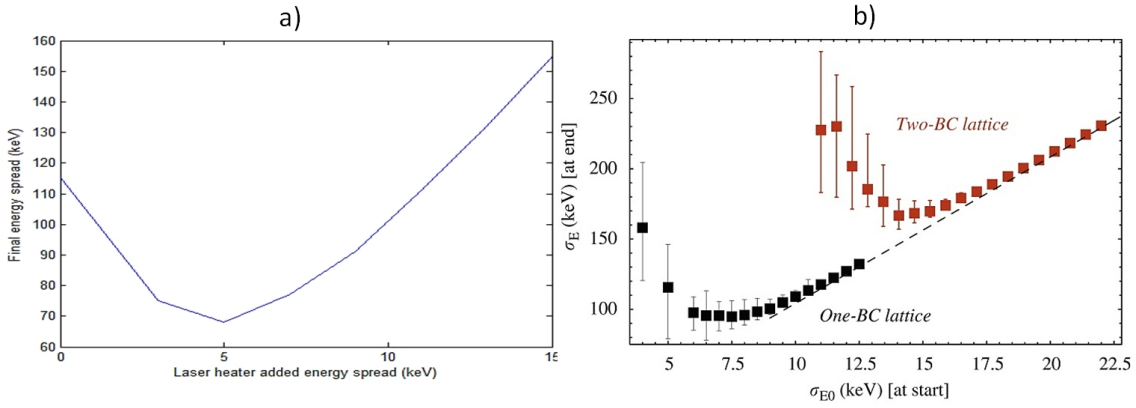

Figure 2.6: a: Final uncorrelated energy spread vs. initial slice energy spread. b: Final vs. initial uncorrelated energy spread for one and two stage compression in FERMI@Elettra. Vlasov solver simulation results taken from [97].

The results shown in figure 2.6b, presented [97], are obtained with a Vlasov solver developed by M.Venturini [96] and are in good agreement with the qualitative behaviour predicted by the linear model.

2.4 Particle and radiation dynamics in the FEL process

The basic principle of the FEL emission relies on the interaction between a relativistic electron beam and a co-propagating electromagnetic wave in the presence of a static, periodic

magnetic field. The magnetic field, provided by an undulator, induces electrons to move on an oscillating trajectory. The transverse component of the electron velocity is then coupled to the electromagnetic field propagating along the undulator axis. This interaction creates a force along this direction and, depending on their phase with respect to the electromagnetic field, electrons can gain or lose energy. As a consequence, the electron distribution inside the bunch is modified: the particles are distributed in micro-bunches separated by the wavelength of the co-propagating radiation. The FEL process starts when there is a net amplification of the electromagnetic wave to the detriment of the electrons' energy. FEL radiation occurs at the wavelength given by the resonance condition (1.4, 1.5). The FEL process can be also seen as a stimulated emission/stimulated absorption process. The electromagnetic wave is amplified (net gain) when the electron beam is slightly out of resonance, because in case of perfect resonance half of the electrons gain energy and half lose energy. FEL dynamics can be described by Maxwell and Lorentz equations in a 3D framework. We consider a mono-energetic electron beam moving through an undulator generating a magnetic field: $\overrightarrow{B_U} = \nabla \times \overrightarrow{A_U}$. We assume the existence of a wave co-propagating with the electron beam in the undulator: $\overrightarrow{E} = -\frac{1}{c} \cdot \frac{\partial \overrightarrow{A}}{\partial t}$ and $B = \nabla \times \overrightarrow{A}$. The total vector potential is the sum of two components:

$$\overrightarrow{A_{tot}}(z,t) = \overrightarrow{A_U}(z) + \overrightarrow{A}(z,t) \tag{2.41}$$

$$\overrightarrow{A_U}(z) = \frac{a_U}{\sqrt{2}}(\overrightarrow{e} exp(-ik_u z) + c.c) \tag{2.42}$$

$$\overrightarrow{A}(z) = -\frac{i}{\sqrt{2}}(\overrightarrow{e}a_r(z,t)exp(-i\Phi_r)exp(ik_r z - i\omega_z t) + c.c) \tag{2.43}$$

where $\overrightarrow{A_U}(z)$ is the undulator vector potential and $\overrightarrow{A}(z,t)$ is the vector potential of the wave. $a_U = \frac{Bk_U}{2}$, $k_U = \frac{2\pi}{\lambda_U}$ where λ_U is the undulator period and $\overrightarrow{e} = \frac{(\overrightarrow{x}+i\overrightarrow{y})}{2}$ where are the orthogonal unit vectors along the $\widehat{x}$ and $\widehat{y}$ axes transverse to the propagation axis z. $k_r = \frac{2\pi}{\lambda_r} = \frac{\omega_r}{c}$, Φ_r is the phase of the radiation field and $a_r = \frac{e\lambda_r E}{2\pi mc^2}$ represents the amplitude of the electromagnetic field, being $E = \left|\overrightarrow{E}\right|$ and e and m the electron charge and mass. Its dependence on transverse coordinates (x and y) is neglected in the plane-wave and paraxial approximation. Although the 3D model so far described is more general and accounts for the three dimensional effects, here we want to review the simplified model presented in [40] which neglects transverse dimensions but captures the essential features of the FEL process. We can derive the equations for electrons dynamics from the Lorentz equation. Considering the electron phase $\theta = (k_r + k_u)z - \omega_r t$ relative to the radiation+undulator field, which propagates in the z direction at the phase velocity $v_p = \frac{\omega_r}{k_r+k_u}$, this expression can be derived in order to get the evolution of the phase. Considering the definitions of the vector potentials, and using the paraxial approximation $\frac{d}{dt} \approx \frac{cdt}{dz}$, we can obtain the equations for the longitudinal evolution of electrons [109] in the one-dimensional (longitudinal) approximation, the evolution of the electrons energy and phase are:

$$\frac{d\gamma}{dz} = -\frac{a_U k_r}{\gamma}a_r(exp[i\theta] - c.c.) \tag{2.44}$$

$$\frac{d\theta}{dz} = k_u - k_r\frac{1 + a_U^2 + ia_U(a_r exp[i\theta] - c.c.)}{2\gamma^2} \tag{2.45}$$

The electromagnetic field obeys the wave equation where the source term is the average over the electron beam cross section of the transverse current density [37, 39]. In the slowly varying envelope approximation (SVEA), given by $\left|\frac{\partial a}{\partial z}\right| << |ak_r|$ and $\left|\frac{\partial a}{\partial t}\right| << |a\omega|$, the second order derivatives can be neglected and the equation for the field can be approximated. Since $\overrightarrow{a}$ is slowly-varying on the scale of the radiation wavelength λ, the transverse current can be average over a longitudinal distance of several wavelengths. Finally the equation for the field evolution, neglecting the transverse variation of the electron and electromagnetic field, in the 1D model can be written as:

$$\left(\frac{\partial}{\partial z}+\frac{1}{c}\frac{\partial}{\partial t}\right)a_r = k_r\left(\frac{\omega_p}{\omega_r}\right)^2\left(a_{rU}\left\langle\frac{exp(-i\theta)}{\gamma}\right\rangle-\left\langle\frac{i}{\gamma}a_r\right\rangle\right) \tag{2.46}$$

where $\omega_p = \sqrt{4\pi e^2\frac{n}{m}}$ is the plasma frequency, with n the total electron number density. The symbol $\langle..\rangle$ represents the average over a sample of N electrons of a given function: $\langle f(\theta,\gamma)\rangle = \frac{1}{n}\sum_{j=1}^{N} f(\theta_j,\gamma_j)$.

We define now the energy-detuning parameter δ_r:

$$\delta_r = \frac{1}{\rho}\frac{\langle\gamma\rangle^2-\gamma_r^2}{\gamma_r^2} \tag{2.47}$$

here $\langle\gamma\rangle$ is the mean electron energy at the undulator entrance and γ_r is the resonant energy. In the regime we are interested in (i.e., the so called Compton regime), the energy of the electron beam is high and the charge density is low, i.e., 1. The relative energy variation of electrons is assumed to be:

$$\left|\frac{\gamma_j-\langle\gamma\rangle}{\langle\gamma\rangle}\right| << 1 \tag{2.48}$$

The derivative with respect to the time, in the equation for the field, can be neglected. The coordinates z and t can be normalized with respect to the undulator length L_U and to l_b/c (where l_b is the bunch length) and therefore the ratio between the temporal and spatial derivative coefficients in the equation becomes $\frac{L_U\left(1-\overline{\beta}_{\parallel}\right)}{\beta_{\parallel} l_b} = \frac{N_U \lambda_r}{l_b}$ where N_U is the number of undulator periods. The term $\frac{N_U \lambda_r}{l_b}$ represents the total slippage, i.e. distance between the electrons and the radiation due to their different velocities. When the total slippage is much smaller than the bunch length l_b, the time derivative can be neglected. This regime is called the "steady-state regime" and its evolution depends only on the longitudinal coordinate. The temporal coherence of the radiation is due to the slippage, because by means of this mechanism the wave fronts can talk to each other. The radiation emitted by electrons in the bunch tail interacts with electrons located as far as the total slippage length.

It has been shown that the field evolution, in the 1D model and steady state Compton regime, along the longitudinal coordinate, from small to strong signal regime and using the original variable z, can be reproduced by the following equations [110] where the so-called fundamental FEL parameter or Pierce parameter is introduced:

$$P_L(z) = \frac{P(0)}{9} \frac{exp(\frac{z}{L_{1d}})}{1 + \frac{P_0}{9P_{sat}}\left[exp(\frac{z}{L_{1d}}) - 1\right]}; \tag{2.49}$$

$$L_{1d} = \frac{1}{g} = \frac{\lambda_U}{4\pi\rho\sqrt{3}}; \tag{2.50}$$

$$L_{sat} = L_{1d} ln(\frac{9P_{sat}}{P(0)}); \tag{2.51}$$

$$P_{sat} \approx \rho Pe = \rho IE; \tag{2.52}$$

$$\rho = [\left(\frac{I}{I_A}\right) \cdot \left(\frac{\lambda_u A_u}{2\pi\sigma_x}\right)^2 \cdot \left(\frac{1}{2\gamma_0}\right)^3]^{\frac{1}{3}};\ A_U = f_c \cdot K_{rms} \tag{2.53}$$

where I is the electron beam peak current, $I_A = 17.05\,kA$ is the Alfven current E is the electron beam mean energy, $\sigma_x = \sigma_y$ are the RMS transverse beam sizes, $P(0)$ is the input power and f_c is 1 for an helical undulator and it is $f_c = \frac{K_{rms}^2}{2\cdot(1+K_{rms}^2)}$ for a planar undulator. The gain function and the total gain can be written as:

$$G(z, \delta_r) = \frac{|a_r|^2(z) - |a_r|_0^2}{|a_r|_0^2}; \tag{2.54}$$

$$G = gL_U = \frac{L_U}{L_{1d}} = 4\sqrt{3}\pi\rho N_U; \tag{2.55}$$

The quantity L_{1d} is the gain length in the 1D approximation. The saturation comes for$z = L_{sat}$. The high-gain regime is characterized by $G > 1$. In our case $\rho << 1$, so that z should be large enough, i.e., the undulator should be sufficiently long($L_U >> L_{1d}$). In the high-gain regime, the equation 2.49 is approximated, for $z < L_{sat}$, as:

$$P_L(z) = \frac{P(0)}{9} exp(\frac{z}{L_{1d}}) \tag{2.56}$$

In the high-gain regime, the line width is [39]:

$$\frac{\triangle\omega_r}{\omega_r} \approx 4\rho \tag{2.57}$$

An alternative picture of the resonance condition is given by the following statement: for each undulator period where the electron passes through, the particle slippage with respect to the wave should be equal to one wavelength of the radiation. This is equivalent to:

$$\frac{\lambda_U \left(c - v_\parallel\right)}{v_\parallel} = \lambda_r \tag{2.58}$$

Considering that $\frac{1}{\gamma^2} = 1 - \beta_\parallel^2 - \beta_\perp^2 = \frac{1}{\gamma^2} - \frac{a_U^3}{\gamma^2}$ and $|\beta_\perp| \approx \frac{a_U}{\gamma}$ it is possible to derive the resonance condition. When an electron beam starts to interact with an electromagnetic wave, all the particles are randomly distributed in phase with respect to the wave, as shown in figure 2.7a.

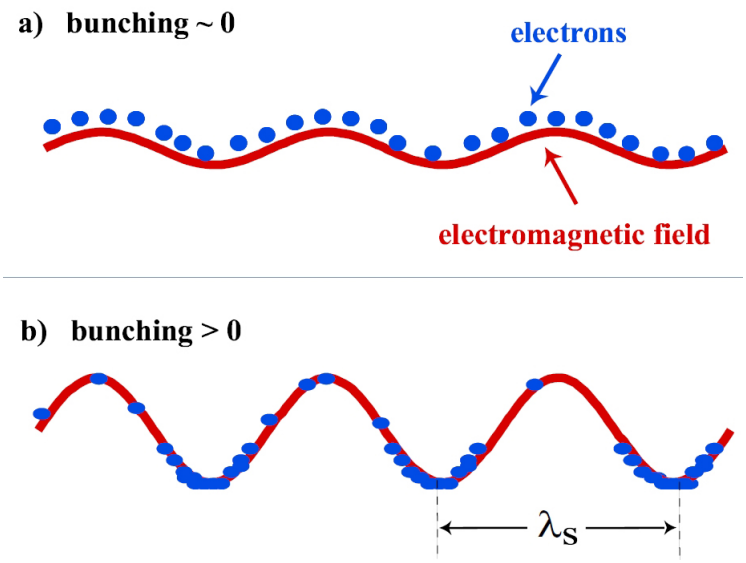

Figure 2.7: Bunching evolution. a: Electrons randomly distributed in phase (initial condition: weak electromagnetic field). b: Electrons start bunching on a λ_s scale and the wave is amplified. Courtesy of F. Curbis.

As the resonance condition is satisfied, i.e. $\tilde{v}_{\parallel} = v_p = \frac{\omega_r}{(k_r + k_U)}$ half of the particles absorb energy from the electromagnetic wave and the other half transfer energy to the wave because the particles tends to cluster where the ponderomotive phase is zero and hence the amplification is zero. But, when the electromagnetic field of the ponderomotive wave changes a lot, as in the high-gain regime, the phase velocity also changes, according to:

$$v_p = \frac{\omega - \dot{\phi}}{k_r + k_U} \tag{2.59}$$

As $\dot{\phi} > 0$, the latter relation states that the electrons act as a dielectric medium slowing down the phase velocity of the ponderomotive wave. The velocity of the resonant electrons is then $\tilde{v}_{\parallel} > v_p$ and they bunch around a phase where there is positive gain. Figure 2.8 explains

the saturation mechanism, as it occurs in the electron phase space (θ, γ). The interaction with the ponderomotive wave induces a modulation of the electrons energy. This energy modulation evolves into a spatial modulation, also called bunching. When electrons exceed the wave of a phase equal to a quarter of the ponderomotive force period there is maximum gain. As the beam proceeds further inside the undulator, the spatial modulation arises also where the ponderomotive force is positive and this causes "over-bunching". Here the process reaches the saturation because the electrons are not anymore able to transfer their energy to the wave. The saturation is not a stationary state because the system does not arrive in an equilibrium condition.

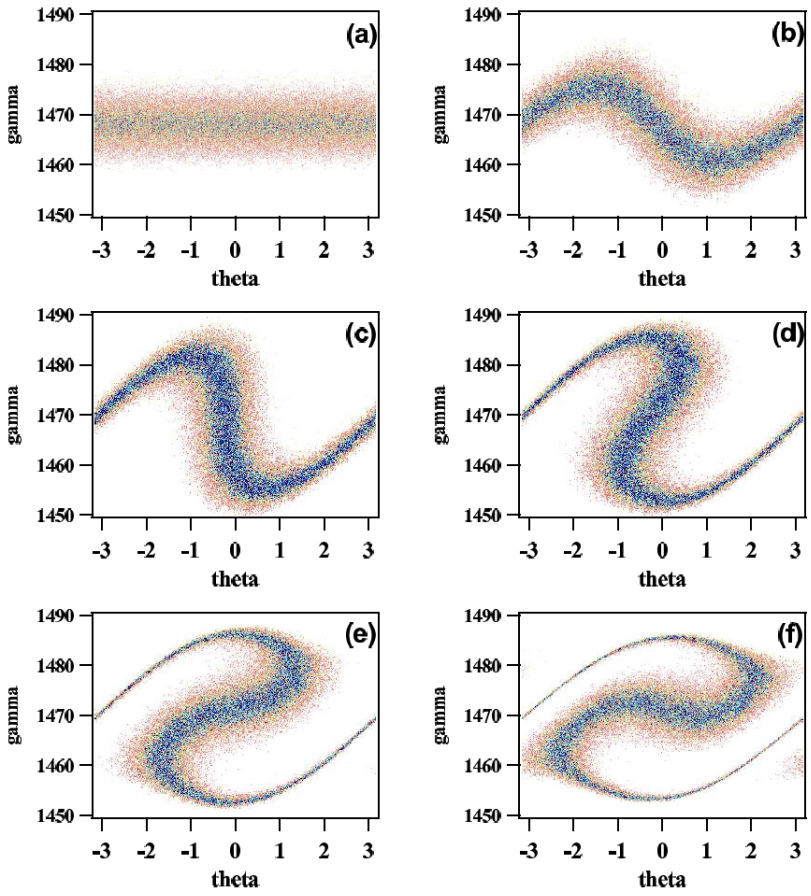

Figure 2.8: Bunching evolution. a: Electrons randomly distributed in phase (initial condition: weak electromagnetic field). b: Electrons start bunching on a λ_s scale and the wave is amplified. Courtesy of F. Curbis.

So far the transverse dimensions of the electron beam and its angular divergence have been neglected, as well as the diffraction of the light. Besides, the hypothesis of mono-energetic beam (mentioned at the very beginning of the derivation of the equations) is far from reality: an electron beam has an intrinsic energy-spread and this affects the performance of the source. The emittance ϵ [90], defined by equation 2.14, is the quantity that takes into account the transverse dimension and the angular dispersion of the electron bunch. The

1D model gives the highest possible FEL gain (shortest gain length) and can be used as a reference for the cases with non-ideal electron beam. In fact it can be shown from rigorous analysis [111, 112] that the FEL gain length can be expressed by a universal scaling function:

$$\frac{L_{1d}}{L_G} = F(\eta_d, \eta_\epsilon, \eta_\gamma); \eta_d = \frac{L_{1d}}{L_R}; \eta_\epsilon = \left(\frac{L_{1d}}{\beta}\right)\left(\frac{4\pi\epsilon}{\lambda}\right); \eta_\gamma = 4\pi\left(\frac{L_{1d}}{\lambda_U}\right)\left(\frac{\sigma_0}{E_0}\right) \tag{2.60}$$

The universal scaling function can be determined by fitting the numerical solutions of the coupled Maxwell-Vlasov equations describing FEL interaction and it is given by [55].

$$\frac{L_{1d}}{L_G} = \frac{1}{1+\eta} \tag{2.61}$$

where:

$$\eta = a_1\eta_d^{a_2} + a_3\eta_\epsilon^{a_4} + a_5\eta_\gamma^{a_6} + a_7\eta_\epsilon^{a_8}\eta_\gamma^{a_9} + a_{10}\eta_d^{a_{11}}\eta_\gamma^{a_{12}} + a_{13}\eta_d^{a_{14}}\eta_\gamma^{a_{15}} + a_{16}\eta_d^{a_{17}}\eta_\epsilon^{a_{18}}\eta_\gamma^{a_{17}} \tag{2.62}$$

and the 19 fitting parameters are given in [55]. The maximum of the scaling function corresponds to the shortest gain length in the 1D limit $\frac{L_{1d}}{L_G} = F(0,0,0) = 1$. The scaling parameters η_d, η_ϵ and η_γ measure the deviation of the beam from the ideal case. Specifically, η_d indicates the gain reduction due to the diffraction while η_ϵ and η_γ measure the gain reduction due to electron's longitudinal velocity spread caused by emittance and by energy spread, respectively. Another scaling parameter related to the wavelength detuning has been optimized to obtain the maximum gain thus eliminated to give the equations. The saturation power obtained empirically by fitting simulation results and the evolution of the

energy spread along the undulator are described by the following equations [113, 114]:

$$P_{sat} = 1.6\sigma \left(\frac{L_{1d}}{L_G}\right)^2 P_{beam};\ \sigma_\gamma(Z) = \sqrt{(\sigma_\gamma(0))^2 + \frac{9}{4}\cdot\frac{\rho}{P_{beam}}\cdot\frac{(P_{sat}-P(0))\cdot P(Z)}{P(0)-P(Z)+1.24(P(0)-P(Z))}} \tag{2.63}$$

where $P(0)$, as sad in section 1.2, is the initial radiation power and $\sigma_\gamma(0)$ is the initial energy spread. In the case of SASE $P(0)$ is provided by the shot noise and a shot noise power P_{noise} can be introduced. An approximation for shot noise power can be given by:

$$P_{noise}(W) = E\,(\rho)^2 \cdot c/\lambda \tag{2.64}$$

Chapter 3

FERMI@Elettra, LCLS, SPARC

In this chapter we describe the general layout of the three FEL facilities in which the experiments described in this thesis were performed: FERMI@Elettra, SLAC and SPARC.

3.1 FERMI@Elettra

FERMI@Elettra [13, 24] is a single-pass FEL facility located at the Sincrotrone Trieste Laboratory. The FERMI complex includes the following parts: a photoinjector generating a bright electron beam [24, 115], the main linear accelerator in which the beam is time-compressed and accelerated up to 1.2 GeV [24, 116], the system to transport the beam to the undulators, the undulators generating the FEL radiation [24, 117], the photon beam delivery system steering the radiation from the undulator to the experimental [118] area and the experimental area itself [119-121]. The whole infrastructure is installed about 5 m below ground level. Figure 3.1 shows a schematic plan (to scale) of the Elettra Laboratory.

The circular building containing the Elettra synchrotron is visible at the centre. Below, the FERMI@Elettra linac, undulator hall and experimental hall infrastructure is shown (the electron beam goes from right to left).

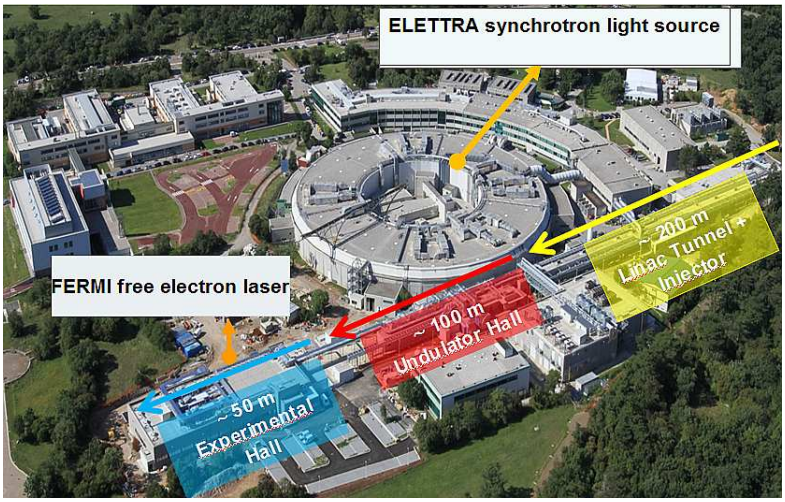

Figure 3.1: Sincrotrone Elettra laboratory with the storage ring Elettra and the free-electron laser FERMI. The circular building containing the Elettra synchrotron is visible at the centre. Below, the FERMI@Elettra linac, undulator hall and experimental hall infrastructure is shown (the electron beam goes from right to left). Courtesy of G. De Ninno.

Figure 3.2 shows the layout of the FERMI accelerator.

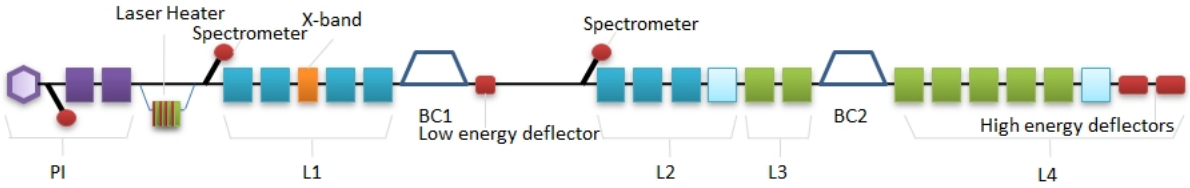

Figure 3.2: Layout of the Elettra beam accelerator of FERMI@Elettra: The electrons are generated in the gun by a copper cathode illuminated with a UV photoinjector laser and then are pre-accelerated in the photoinjector that includes two booster cavities. The first linac sections (L1) accelerate the beam and produce the chirp needed for bunch compression in BC1. Linac1 includes a harmonic cavity used to linearize the compression. A second bunch compressor, BC2, is placed after the other 5 cavities (L2 and L3). These cavities bring the beam to the final energy of 1.2 GeV (L4). The last two cavities, coloured in red, are two transverse deflectors. The linac can be run with one or two compressors switched on. Three spectrometer lines, used to measure the beam energy and energy spread after the photoinjector and along the linac, are shown. The two cyan squares indicate two additional cavities that can eventually be installed to increase the beam energy up to ≈1.5 GeV. Taken from [24].

The new low emittance RF photoinjector is based on the 1.6 cell electron gun [115] developed at BNL/SLAC/UCLA [122]. The beam is produced by the impact of a UV laser beam (261 nm) on a copper cathode. The beam is accelerated in the gun cavity, composed of a 1.6 S-band cell up to an energy of $\approx 5\,MeV$. The gun cavity is surrounded by a solenoid to compensate for the transverse defocusing action of space charge that is very strong when the beam is non-relativistic. Then the beam goes into two booster cavities, with the first placed at a distance from the gun which is imposed by the emittance compensation scheme, in which the beam is accelerated up to an energy of $\approx 100MeV$. A compact diagnostic section, equipped with a bending spectrometer, beam position monitors (BPMs), screens and quadrupoles is inserted between the gun and the booster cavity. A transfer line equipped with six quadrupoles, the laser heater system that is described in the section 4, beam position monitors (BPMs), multi-screen diagnostic stations for beam profile measurement and

a bending energy spectrometer is placed between the photoinjector and the linac [123]. The measurement of the emittance and of the Twiss parameters are made, with the quadrupole scan technique, using the last quadrupole before the laser heater chicane and the screen placed after the laser heater undulator close to the electron beam waist location. Then these data are used to determine the beam Twiss functions at the exit of the photoinjector by backtracking. The quadrupoles of the transport line are used to transversely match the electron beam to the linac. Figure 3.3 shows a 3D model of the low energy transfer line that connects the photoinjector to the linac.

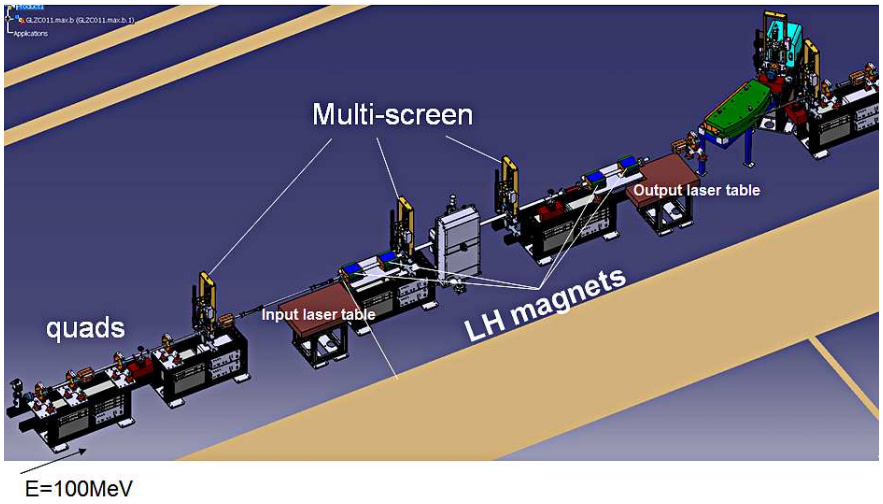

Figure 3.3: 3D model of the transfer line that connects the photoinjector with the linac. The first part of this transfer line includes four quadrupole magnets. This matching section is followed by the laser heater chicane, formed by four dipole magnets, that holds the laser heater undulator, screens for diagnostics and a BPM. A spectrometer is located in the last part of the transfer line. Courtesy of G. Penco.

The linac begins with a first stage called linac 1 (L1) composed by four CERN S-band cavities working at 2.998 *GHz*, and an 1 X-band cavity used to linearize the electron beam phase space before beam compression. The CERN cavities have an accelerating gradient

of $\approx 15 MV/m$ and the beam can reach an energy of 321 *MeV* when the RF phase, ϕ, is set to 90 degrees. A 8.0 m long symmetric chicane, shown in figure 2.4, is placed after L1. It includes four identical bending magnets all powered by one power supply, two identical quadrupole magnets in the lateral arms and four independently powered trim coils, each of them associated with one bending magnet. These are intended for a fine tuning of the dispersion bump by compensating the field-to-current calibration errors in the dipole fields. Some electron beam diagnostics and machine protection device are located in between the two inner bending magnets: one horizontal scraper, one BPM and one screen. The design of the magnetic compressor derives from LCLS [124] and has been modified with some improvements of field homogeneity and movement accuracy and reproducibility. An X-band cavity [125], working at the fourth harmonic of the S-band, is inserted in the middle of L1 to linearize bunch length compression. The harmonic cavity is operated near the deceleration crest lowering the beam energy by 20 *MeV*. Another transfer line [126] is equipped with screens, BPMs, quadrupole, correctors, an energy spectrometer and a vertical RF deflecting cavity (low energy RF deflector, LERFD) [127-129]. The beam can be deflected vertically by LERFD for beam slice measurements. The LERFD cavity is a five cell standing wave structure, sharing the same klystron with the electron gun. After the LERFD cavity, four quadrupoles and three multi-screens stations are placed for measuring the beam optics parameters and matching them after the longitudinal compression. The multi-screen stations are equipped with Optical Transition Radiation (OTR) [130] and Yttrium Aluminium Garnet (YAG) targets [131]. This diagnostic station, located after BC1, is shown in figure 3.4.

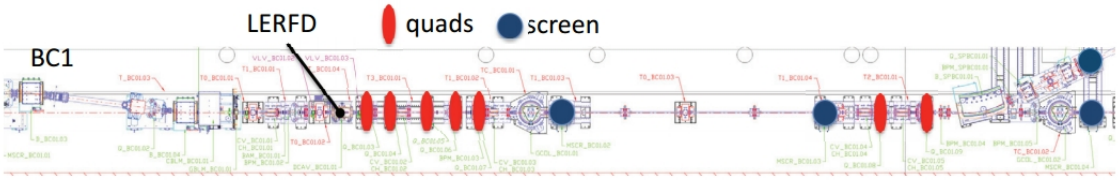

Figure 3.4: Diagnostic station after BC1. This transfer line is equipped with a transverse RF deflecting cavity (LERFD) for beam slice measurements. After the LERFD cavity, four quadrupoles and three multi-screens stations are placed for measuring the beam optics parameters and matching them after the longitudinal compression. The multi-screen stations are equipped with Optical Transition Radiation (OTR) and Yttrium Aluminium Garnet (YAG) targets. Courtesy of G. Penco.

The beam is then accelerated in three other CERN cavities and the seven Elettra cavities up to an energy of 1.2 GeV. A second bunch compressor is placed in the linac before the last five Elettra cavities (L4). The two bunch compressors allow continuously tunable compression of the bunch length by a factor 1-50. The nominal compression factor of 10 [24] can be obtained with a two stage compression or with BC1 only. The two schemes imply a different balance of the parameters characterizing the final electron beam quality, such as current and energy flatness, emittance, slice energy spread, current and time jitter. Hence, they can be used alternatively, according to specific FEL requirements. At the moment, the scheme with one compressor is used to generate FEL light with high spectral purity for users experiments. A 0.8 m long drift section, presented after each accelerating structure along the whole linac provides focusing and trajectory control. It includes one quadrupole magnet with a bipolar power supply, one BPM and two correctors. Another diagnostic area is present at the end of the FERMI linac, including a horizontal high energy RF deflecting cavity (HERFDX) [132], a vertical high energy RF deflecting cavity (HERFDY) [132] and the high energy (1.2-1.5

GeV) spectrometer beam-line, called Diagnostic Beam Dump (DBD). Figure 3.5 shows the layout of the high energy diagnostic section.

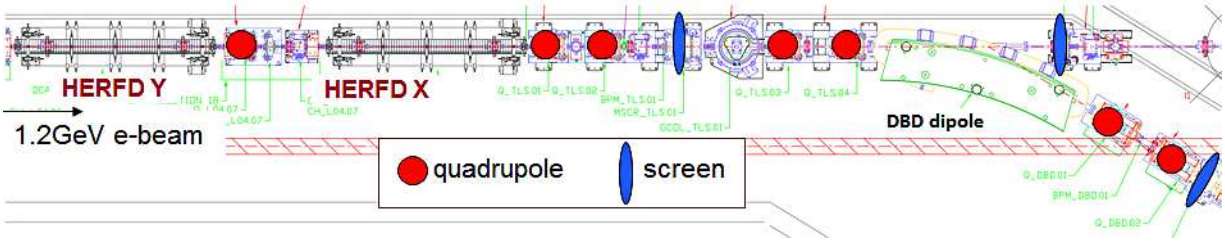

Figure 3.5: Beam diagnostic area at the FERMI linac end. This transfers line includes a horizontal RF deflecting cavity (HERFDX) [132], a vertical RF deflecting cavity (HERFDY) and the high energy (1.2-1.5 *GeV*) spectrometer beam-line, called Diagnostic Beam dump (DBD). Courtesy of G. Penco.

The electron beam can be sent into one of the two FERMI undulator lines, FEL1 and FEL2, through a system called spreader. The spreader starts with two 3 degree dipole bending magnets that deflect the beam away from the linac axis. Another pair of 3 degree bending magnets deflects the beam on the FEL2 line, which is parallel to the linac axis at a distance of 1 m. The beam, when the first of the afore mentioned bending magnets are switched off, goes to another pair of bending magnets that brings it parallel to FEL2 line at a distance of 2 meters from it into the FEL1 line. Figure 3.6 shows a sketch (not to scale) of the FERMI spreader.

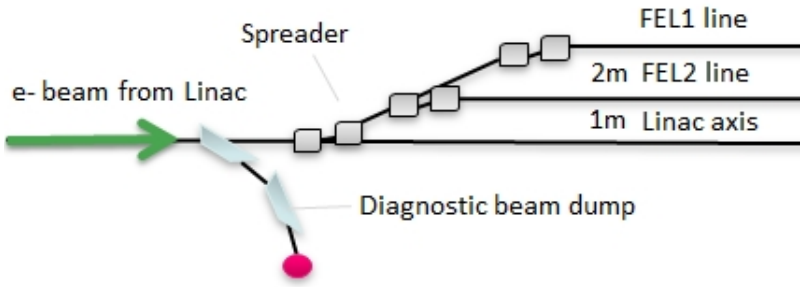

Figure 3.6: Layout of the FERMI spreader. A pair of dipoles deflects the beam away from the linac axis. One other pair of dipoles is used to bring the beam on one of the two FEL line, FEL1 or FEL2. The diagnostic beam dump for the electron beam generated in the linac is visible in the bottom part of the picture. Taken from [24].

FEL1 is a single stage HGHG seeded FEL cascade which is composed, as described in the introduction, of a modulator, a dispersive section and a radiator. The electron beam interacts with the seed in the modulator and it gains a spatial energy modulation at the laser wavelength. The energy modulation is converted to a density modulation, at the harmonics of the laser wavelength, in the dispersive section. The FEL light is produced in the radiator. Figure 3.7 shows the layout of the FEL1 line.

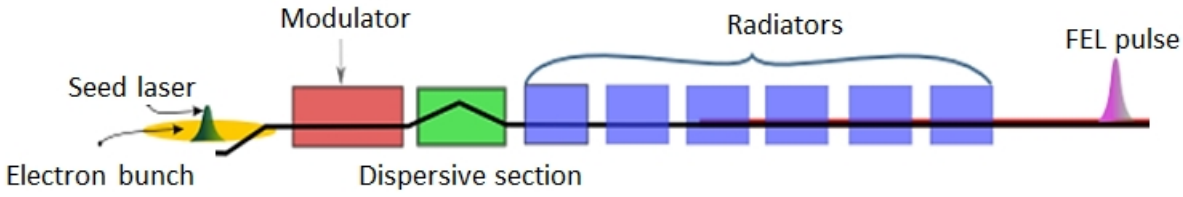

Figure 3.7: Schematic of the FERMI FEL1. The electron beam is sent to the FEL1 line. Electrons interact with the seed laser within the modulator. Here the beam energy is modulated by the laser. FEL radiation is emitted in the radiator at the desired harmonic of the seed. The radiator is composed of 6 Apple II undulators. Taken from [24].

The modulator is a single planar undulator with variable gap that contains 30 periods of 10 cm. The dispersive section is an achromatic magnetic device with a non-zero R_{56} and zero total dispersion. The R_{56} can be varied in the range $0 - 130\,\mu m$. The radiator is composed of six Apple II undulators. Each 2.4 m long radiator section has a period of 55 mm. The gap of the radiator can be changed from 10.5 mm to 220 mm to permit a wide tuning of the FEL output. The minimum wavelength on which the radiator can be tuned with $K \geq 1$, considering an electron beam energy of 1.2 GeV, is 17 nm that corresponds to the 15th harmonic of the seed laser. The Apple II type helical undulator is a pure permanent magnet structure composed of four arrays of magnetic blocks. There are four magnetic blocks per period as shown in figure 3.8.

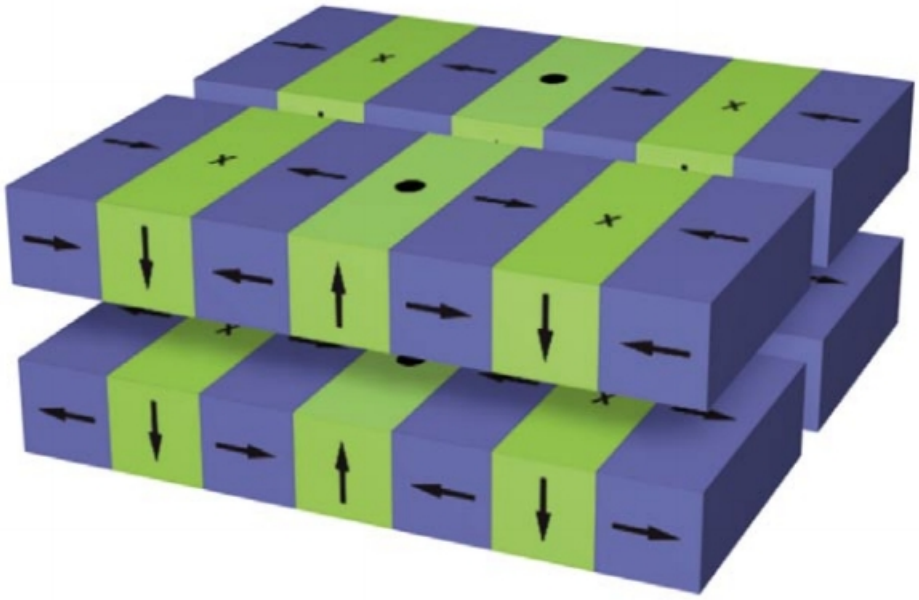

Figure 3.8: Sketch of Apple II block configuration. Each period contains 4 blocks, one for each array. Taken from [24].

The strengths of the vertical and horizontal magnetic field components can be varied, and hence the polarization of the radiation produced, by moving two opposing magnet arrays with respect to the other two along the undulator axis. The advantage of such a device is that the radiation can be polarized vertically, horizontally, and circularly by moving the arrays. Phase shifters [133] are installed in each section break between two radiator sections, to maintain the right phase relation between the electron beam and the radiation when passing from one undulator section to the next. A quadrupole for beam focusing and a RF cavity BPM [134] are inserted in each undulator break. The seed can be the third harmonic (266 *nm*) of a Ti:Sa infrared laser (780 *nm*) or the output of an optical parametric amplifier [135]. Two YAG screens placed at the two modulator ends permit the seed and the electron beam to be transversely aligned. A fast photodiode, placed few meter before the modulator, is used to measure the temporal delay between the seed and the transition radiation produced by the electron beam passing through an OTR screen and provides a clear time reference for the beams. Delays shorter than 6 *ns* are compensated with a delay line for the seed laser while for greater delay it is mandatory to adjust the electronic trigger in the seed laser. This coarse time synchronization, done with the photodiode, permits the laser and the electron beam to overlap leaving a delay between the two of less than 10 *ps*. The fine overlap can be obtained measuring the FEL pulse energy while moving the delay line over a range of $\approx 50\,ps$. After leaving the undulators, while the FEL radiation is transported to the experimental area, the electron beam is brought to a beam dump by a sequence of bending magnets. Figure 3.9 shows the FERMI beam dump between the undulator hall and the experimental hall.

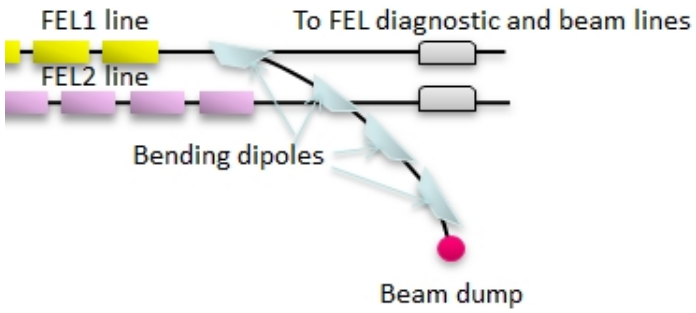

Figure 3.9: FERMI beam dump between the undulator hall and the experimental hall. The FEL radiation is transported to the experimental area, while the electron beam is brought to a beam dump by a sequence of bending magnets. Taken from [24].

The FEL system is completed by the photon diagnostics that are used to characterize the FERMI FEL pulses and that are placed just before the beamlines. The FEL intensity can be measured by means of two gas ionization cells [116, 136] placed between the undulator hall and the experimental hall. Since only a very small portion of the FEL photons ionize the gas, the method can be used online while the FEL is operating for users. The intensity of single FEL pulses can be measured with a fast photodiode [136] that intercepts all of the photons. The scheme of the layout used to measure the FEL energy is reproduced in figure 3.10.

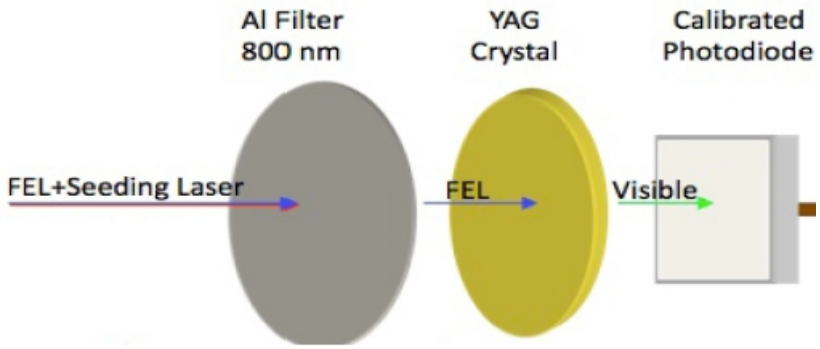

Figure 3.10: Layout of measurements of the FEL energy with the photodiode. Courtesy of M. Zangrando.

The spectral properties of the FEL are measured using a dedicated spectrometer [137] that uses the first order diffraction while the zero order beam, carrying 97% of the total energy, goes to the experimental stations. This spectrometer is an online diagnostic that does not interfere with FEL operation for users. Diffraction is generated by a planar variable spacing grating that focuses the first order diffraction onto a YAG screen with the fluorescent intensity detected by a CCD. single-shot spectra can be acquired for FEL intensities higher than a few μJ. Transverse characterization of the FEL pulses can be done using two YAG screens that intercept the FEL beam in two different locations. FEL-induced fluorescence on the YAG is sensed by CCDs. The characterized FEL can then be sent to one of the beamlines. Figure 3.10 shows the photon beam delivery system and the experimental beamline complex.

Figure 3.11: Schematic of the FERMI experimental hall including the photon beam transport system and the three experimental chambers. The first part of the FEL front hand includes, for both FEL1 and FEL2, two ionization chamber intensity monitors and a gas cell providing a wide range tunable intensity attenuation. Then, the light impinges on a variable spacing grating positioned to direct the first diffraction order, 3% of radiation power, onto a YAG screen with fluorescent intensity detected by a CCD while the zeroth order goes to one of the experimental stations. This system permits to measure the FEL spectrum during user operation. Courtesy of D. Cocco.

FEL2 [84] is a double stage HGHG seeded cascade using the fresh bunch technique described in section 1.2 and has a fundamental output in the range 4-20 *nm*. A sufficiently high flux at the third harmonic of the fundamental of the output radiator of FEL2 could reach that part of spectrum at which the water is transparent, 2-4 *nm* and that for this reason is particularly important for biological studies.

3.2 LCLS

The linac Coherent Light Source (LCLS) [61] is a SASE X-ray FEL facility in operation at SLAC since mid-April 2009 [10]. Figure 3.8 shows the layout of the LCLS.

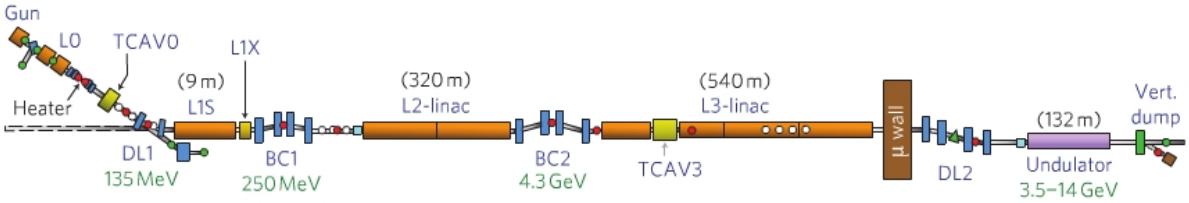

Figure 3.12: LCLS layout. The electron are generated in a photocathode gun and pre-accelerated in the photoinjector (L0). The beam is then manipulated in the laser heater to increase its energy spread. A dogleg connects the photoinjector to the linac. The photoinjector is not in line with the rest of the accelerator as it has been installed in the SLAC linac tunnel without removing the rest of the linac not used by LCLS. The first part of the linac (L1) accelerates the beam and produces the chirp needed for bunch compression in BC1. L1 includes a harmonic cavity used to linearize the compression. A second bunch compressor, BC2, is placed after the second part of the linac (L2) in a point in which the beam has an energy in range 3-5 GeV. the beam energy can be increased from 3 GeV to 15 GeV in the third section of the linac (3). The beam is then transported through a long transfer line into the undulator. The X-ray beams go to the experimental station while the electron beam is deflected by dipoles magnets and dumped. The beam bump line and the experimental station are not shown here. Taken from [10].

The injector includes a RF photocathode gun and a laser heater. The beam reaches an energy of 135 MeV and then enters the linac in which it can be accelerated up to an energy of 15 GeV and is compressed by two bunch compressors by a compression factor up to 100. Table 3.1 shows the parameters of LCLS electron beam and FEL light.

LCLS can be run with a bunch charge of 40-250 pC [138, 139, 140]. The slice emittance has a value of 0.7 $mm{\cdot}mrad$ for 250 pC and decreases with the charge to a value $<0.4 mm \cdot mrad$ for the 40-20 pC case. The 40-20 pC operations require a higher compression factor to reach a good peak current. The FEL pulse has time duration of tens of fs for the 250 pC bunch operation and it is below the $10fs$ for20-40 pC bunch. The 20-40 pC bunch operation permits the delivery of very short pulses, while the pulse energy is higher for the 250 pC

Parameter	Value
Repetition Rate	1-120 Hz
Beam Energy	4.7-14.1 GeV
Bunch Charge	20-250 pC
Bunch length	15-400 fs
Peak current	1.5-3 kA
Slice energy spread	1.5-4 MeV
Slice emittance	$\approx$0.4-1 $mm{\cdot}mrad$
Undulator length	120 m
Undulator period	3.0 cm
Undulator K	3.5-3.46
Output wavelength	0.1-4 nm

Table 3.1: LCLS parameters.

bunch.

The LCLS undulator [141, 142] is 132 m long (including breaks for quadrupole magnets) and was initially composed of thirty-three 3.4 m long planar, permanent magnet undulator segments with 3 cm period, 6.8 mm full gap (fixed) height, and undulator parameter K=3.5. The linac can be operated at any energy in the range of 3-15 GeV. This permits the undulator resonance and FEL output to be tuned in the range of $1 - 40 \cdot 10^{-10} m$ wavelength. A break occurs between each undulator magnet. A quadrupole magnet, an X-band cavity-type high resolution beam position monitor (BPM) [143], a "beam-finder wire" (BFW) and flexible bellows are located at each break. Each undulator segment and its beamline components are mounted on a remotely moveable support structure, called a girder [141]. The girder motion is remotely controlled allowing the horizontal and vertical position to be changed, as well as the yaw, the pitch and roll of the girders. Each girder hosts one undulator segment, a quadrupole, a BPM, a beam finder wire, a Cerenkov radiation detector for machine protection and supports for the vacuum chamber. For obtaining and maintaining high-gain

in the SASE process, it is important that the electron bunch has a good overlap with the radiation field and that the individual electrons maintain a well defined phase relationship with that field. The radiation field is initially produced in the first undulator segment and proceeds in a straight line, while the electron beam trajectory deviates from a straight line in the presence of magnetic and electric fields. The electron beam trajectory straightness requested by the FEL process depends critically on the wavelength and on the gain length. The electron beam trajectory through the FEL undulator must be, in the case of LCLS at the shorter wavelength of $1.5 \cdot 10^{-10} m$, straight to a level of about 2 μm over one FEL gain length ($\approx$5 m) [144]. The ideal undulator magnetic field generates the tiny wiggling motion, which is necessary for the FEL process; the first and second field integrals over each undulator segment are ideally zero. Problems arise from off-axis fields of misaligned quadrupoles and undulator segments, the earth's magnetic field [145], other environmental fields, as well as from errors in the undulator fields that create finite field integrals or increase the electrons' path lengths through the undulator Alignment of all the undulator beamline, the correction of the undulator field and the shielding and compensation of other magnetic field is important to ensure the required straight electron trajectory All the components on a girder are aligned on a coordinate measurement machine [146]. The girders are placed in the tunnel and aligned by optical methods (laser tracker). Every undulator segment is shielded against the magnetic field [145]. The remaining error-fields (off-axis fields in quadrupoles and undulator segments, the earth's magnetic field and the environmental field) are corrected through beam based alignment [144], which compensates the net effect of these fields by adjusting the transverse positions of the quadrupoles, through girder motion and by adding small dipole correction fields through trim coil adjustments. This

process removes the largest error field sources (e.g., misaligned quadrupoles), by moving the centres of the quadrupole magnets, close to a common straight line. The position of each quadrupole defined through the beam based alignment (BBA) process [144] is slightly away from a straight line, to compensate for other remaining error sources. The electron wiggle motion is in the horizontal plane. The upper and lower pole face planes are canted with respect to each other by an angle of about 5.5 *mrad*, which makes their K parameter values dependent on the electron beam's horizontal position with respect to the undulator. A horizontal girder displacement, from the position determined by BBA, permits to change the K of each undulator segment in a ≈1% range. Each segment undulator K value is tuned in this way to compensate for energy losses (wake fields, spontaneous radiation and FEL) and to optimize the FEL process. The sixteenth undulator segment has been replaced by the chicane for the self-seeding experiment. We report the layout of the LCLS undulator line modified for the self-seeding experiment in figure 3.13.

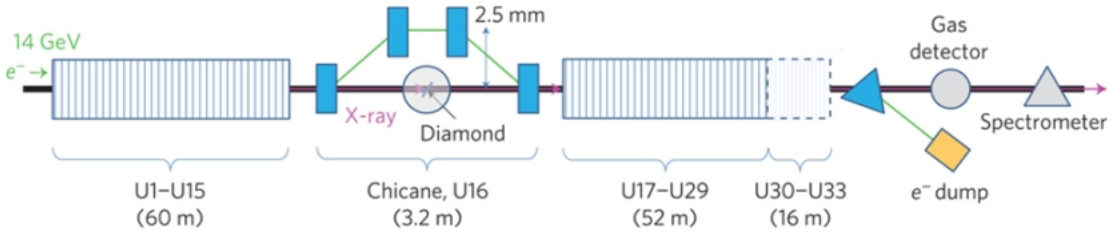

Figure 3.13: LCLS undulator line configured for self-seeding. Taken from [77].

The hardware for the self-seeding experiments is shown in figure 3.14.

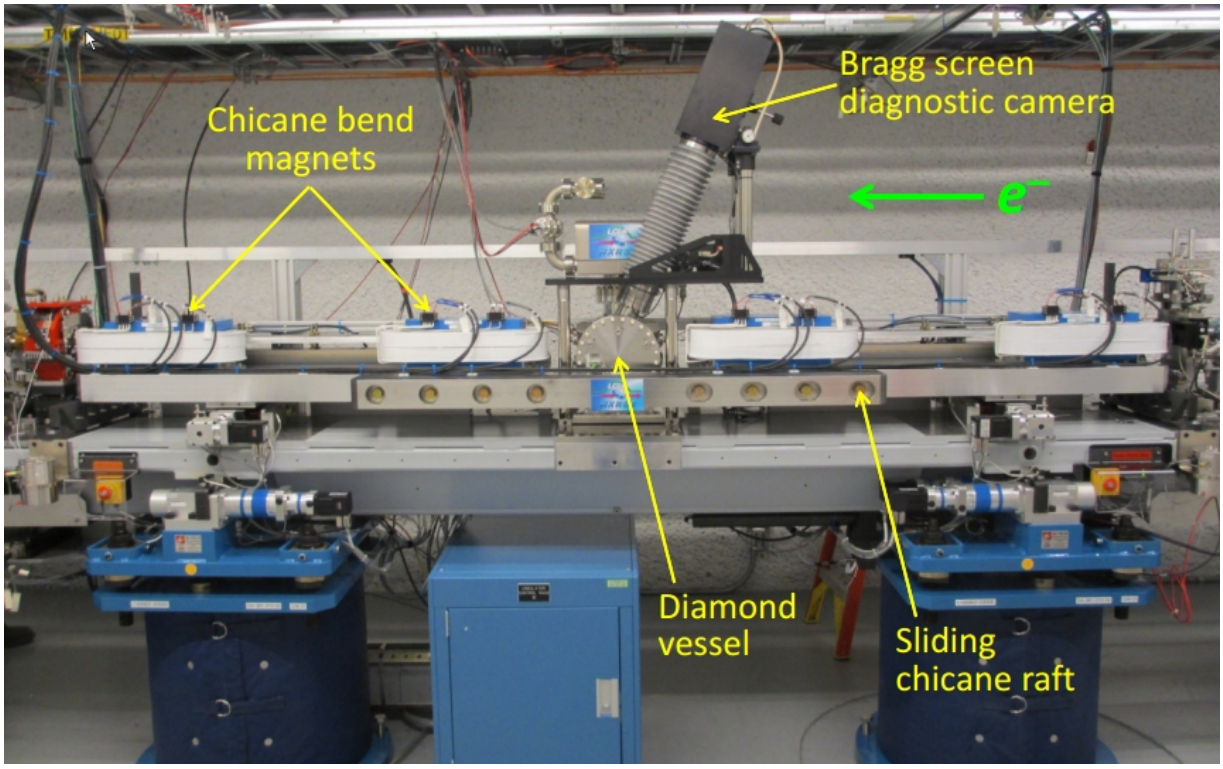

Figure 3.14: Hardware for self-seeding installed on the girder of U16. The chicane for the electron beam is formed by four magnets. The vessel containing the diamond and the diagnostics for the Bragg reflection is installed in the middle of the chicane. Courtesy of P. Emma.

The 3.2 m long magnetic chicane installed at U16 includes four dipole magnets, which displace the electrons horizontally by 2.5 mm to bypass the diamond monochromator. This also nominally delays the electrons by 20 fs so as to overlap with the delayed monochromatic X-ray seed pulse. Each chicane magnet is 36 cm long, separated from its neighbours by 58 cm and nominally bends the electron beam by 2.7 $mrad$ with a magnetic field of 0.34 T, and includes a 576-turn main coil and an independently powered 10-turn trim coil. This allows the chicane to be adjusted between two different configurations: (i) a self-seeded mode, with

the electron delay set between zero and 40 *fs* using the main coils, and (ii) a much weaker 'phase-shift' mode, using the trim coils, with a delay of zero to$10 \cdot 10^{-10} m$ (variable in $0.04 \cdot 10^{-10} m$ steps). The phase-shift mode (used during SASE operation) allows correction of the electron-to-radiation phase error introduced by the removal of the 4 *m* long undulator section at U16. This correction restores the full SASE X-ray pulse energy that was available before the undulator section was removed. In addition, the dependence of the chicane path length on electron energy, given by the R_{56} value of the transport matrix, washes out the SASE-induced microbunching after the chicane, preparing the electron beam for coherent seeding. With a typical relative electron energy spread of about σ_γ=0.01% RMS, the chicane will wash out any temporal structure of wavelength less than $\lambda \approx 2\pi R_{56}\sigma_\gamma$ ($<80 \cdot 10^{-10}$), which is very effective in erasing the $1.5 \cdot 10^{-10}$ microbunching built up by the 15 undulator sections before the chicane. The chamber for the single crystal monochromator is installed in the middle of the chicane with the diagnostics for the Bragg reflection. The monochromator crystal is a high-quality, $110 \mu m$ thick type-IIa diamond crystal plate with a thickness of 110 μm a (004) lattice orientation and a total area of 4.5 $mm \times 4.0$ mm. The diamond crystal was grown from high-purity (99.9995%) graphite at the Technological Institute for Super-hard and Novel Carbon Materials (TISNCM, Troitsk, Russia) using the temperature gradient method under high-pressure (5 GPa) and high-temperature (1,750 K) conditions. The crystal is installed inside a vacuum vessel, supported gently by a graphite holder, and connected to a remotely controlled, high-resolution rotational stage (figure 3.14) for adjusting the Bragg angle (rotation about the horizontal axis through the middle of the diamond). This is controlled by means of an in-vacuum rotational stage with a range of $\theta = 45 - 90\, degrees$. The diamond can also be remotely positioned in the horizontal (x) or

vertical (y) directions using two in-vacuum piezo-controlled translation stages.

The diagnostics for the FEL light includes a ionization gas monitor chamber, an X-ray YAG screen and two spectrometers located in the experimental area [147].

3.3 SPARC

SPARC is a test facility for FEL and beam physics studies. Several concepts of FEL and beam physics and technical tools, for example diagnostics and seed lasers, can be tested here. SPARC is based on two main components, a high brightness photoinjector that provides a high quality beam at energies between 150 and 200 MeV (table 3.2 and [148]) and a single-pass FEL, whose undulator beam-line [149] is composed of six undulator sections of 77 periods each, with a period length of 2.8 cm and a variable K value.

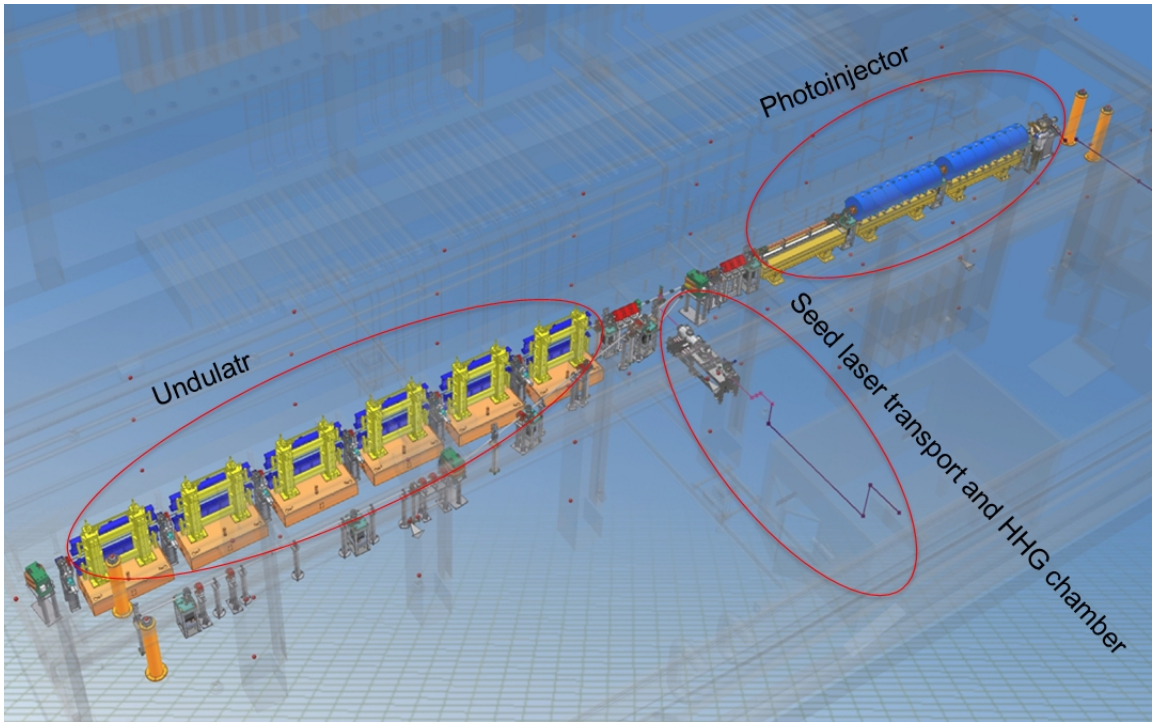

Figure 3.15: SPARC layout. The photoinjector is composed of a photocathode gun and three S-band RF sections. The first two sections are surrounded by solenoids. The beam delivered by the photoinjector is transported by a short transfer line formed by four dipoles and two quadrupole triplets to the undulator composed of six section. The four dipoles allow the beam to pass around a mirror used for the injection of the seed laser. Courtesy of L. Giannessi.

SPARC does not have a magnetic bunch compressor to increase the bunch current but can be operated using a velocity bunching scheme [150]. This leads to a higher current but leaves a big energy chirp along the bunch. SPARC is the first machine in which a compression scheme alternative to the magnetic bunch compressor has been tested [151]. The big chirp of the velocity bunching compressed scheme has permitted to test a FEL scheme in which the chirp is compensated by undulator tapering to produce a single spike pulse in the SASE mode. SPARC FEL can operate in self-amplified spontaneous emission (SASE) mode at a

Parameter	Value (Velocity bunching-chirped beam experiment)
Repetition rate	1-10 Hz
Beam energy	175 MeV (140 MeV)
Bunch charge	0.2-1.1 nC
Bunch length	4 ps (1 ps)
Peak current	70 A (300 A)
Slice energy spread	<40 keV
Slice emittance	1.5 $mm{\cdot}mrad$
Undulator length	14 m
Undulator period	2.8 cm
Undulator K	0.7-2.18
Output wavelength	116-530 nm

Table 3.2: SPARC parameters.

wavelength in the range of 400-500 nm with a saturation length of about 10-12 m with the beam parameters are listed in table 3.2.

The flexibility offered by the variable gap configuration of the SPARC undulator and the natural synchronization of the electron beam with the laser driving the photoinjector, makes the SPARC layout particularly suited for a number of experiments where the FEL amplifier is seeded by an external laser source. Several seeds have been tested at SPARC. The seed laser is driven by the same oscillator initiating the laser cascade which is used to run the photocathode and consists in a regenerative amplifier delivering 2.5 mJ at 800 nm with a pulse duration shorter than 120 fs. The infrared laser is used to produce the second and third harmonic, 400 nm and 266 nm, generated in a LBO crystals or higher harmonics in an Argon gas jet in a gas-cell [152]. Recently the same infrared laser has been used to produce UV radiation in a hollow core fibre filled with Argon [153]. These tests with different seeds are important as a reliable external seed at low wavelength would permit very short wavelength with short HGHG seeded FELs and this could be a real improvement for FEL

facilities. The main diagnostics of the FEL light installed at SPARC is a spectrometer. For some experiments a FROG and a speckles coherence monitor have been used to measure the longitudinal light phase space and the coherence of the FEL pulse [154, 155].

Chapter 4

FERMI linac

In this chapter we describe the FEL1 requirements and report about the FERMI@Elettra linac commissioning. FEL1 and FEL2 require a high brightness electron beam. The smoothness and regularity of the electron beam phase space is required to preserve the longitudinal coherence of the seed laser and a small slice energy spread allows very short wavelengths to be reached. The linearity and smoothness of the electron beam phase space at a few microns and sub-micron scales, which is fundamental to obtain a Gaussian-like spectrum, can be spoiled by the microbunching instability [95]. The implementation of a laser heater [106-108, 156] reduces this phenomenon. For this reason we dedicate this chapter to the linac commissioning describing the phase space preservation and the commissioning of the laser heater system [156] that was installed on a HGHG FEL for the first time. In the next chapter we will describe the FEL performance in relation to the electron beam quality.

4.1 Electron beam requirements

The scientific case of FEL1 includes time domain studies on non-linear phenomena in inelastic scattering, in low density samples and coherent diffraction image of nano-sized samples [24]. The required photon output is characterized by a high number of photons per pulse ($5 \cdot 10^{13}$), a short pulse duration (50-100 *fs*), a narrow bandwidth ($\approx$20 MeV), a good coherence and a good shot to shot reproducibility. All these requirements ask for a very bright electron beam as for every X-ray and VUV FEL project. The peak current has to be >500 A. Further constraints on the characteristics of the electron beam for FERMI, and therefore on the linac working point, come from the use of the seeding technique. In fact the electron beam has to be long enough to ensure a good temporal overlap with the laser beam, considering also the time jitter and the slippage length. The expected RMS arrival time jitter with respect to the seeding laser is <150 *fs* and the slippage of the FEL pulse on the electron beam is 100 *fs*. The duration of the good part of the electron bunch must be at least 300-400 *fs* full width at half maximum (FWHM) for a 100 *fs* (FWHM) long seed pulse, in order to ensure sufficient overlap between the seed and the electrons. This is quite a long beam requiring 500 pC of charge to reach a current of 500-600 A. We describe this condition in figure 4.1. The red ellipse represents the electron beam, the green ellipse is the good part of the electron beam and the blue is the laser beam. The pale blue ellipse represents the laser jitter.

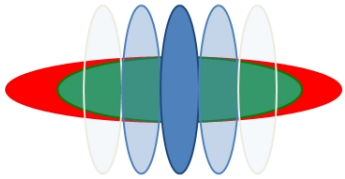

Figure 4.1: Laser electron overlap.

The optimized photoinjector delivers a 2.8 ps (RMS) long beam with a charge of 500 pC and transverse normalized slice emittance$<0.8\mu m$. A compression factor of ten gives a current of 500-600 A. This operational configuration ensures a very high number of photons per pulse even at short wavelengths ($\approx$20 nm). The HGHG schemes have particular requirements about the electron beam longitudinal phase space due to the presence of a strong dispersive section which effects the electron beam energy spread, linear and quadratic chirp to reduce the FEL output quality. The linear chirp in the bunch energy distribution mainly induces a frequency shift of the FEL radiation, while a quadratic curvature enlarges the FEL radiation bandwidth [157-159]. The local beam chirp produces a beam compression or decompression of the bunch in the dispersive section. The linear chirp in the bunch energy distribution induces a constant variation of the wavelength of the microbunching with respect to the harmonics of the seed laser and then a frequency shift of the FEL radiation, while the quadratic curvature enlarges the FEL radiation bandwidth as the frequency shift changes from negative to positive along the bunch. The influence of a quadratic chirp on the HGHG process is shown in figure 4.2.

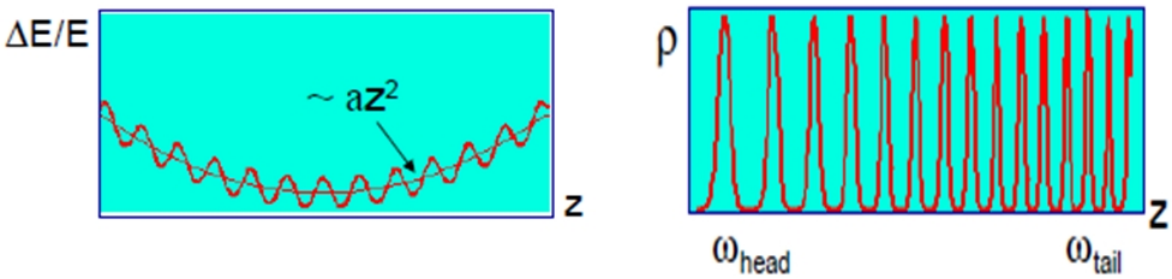

Figure 4.2: Energy chirp and bunching formation in HGHG. The energy variation along the bunch after the modulator, in presence of a quadratic chirp, is shown on the left. The electron density is shown on the right. Courtesy of W. Fawley.

In the presence of the time jitter between the electron bunch and the seed laser of about 100 *fs (RMS)*, the combination of linear and quadratic terms in the bunch energy distribution produce a jitter of the spectrum and intensity of the FEL radiation [24]. Optimization of longitudinal phase space is discussed in section 4.3.

The electron beam energy spread produces a Landau damping in the dispersion section and puts a limit on the highest harmonic that can be reached. An energy spread lower that 200 *keV* is required to reach the 13th harmonic. A low energy spread reduces the gain length in the radiator. The microbunching instability, described in section 2.3, is the principal source of increasing the energy spread in the linac and has to be limited to obtain the desired beam energy spread. The implementation of a laser heater [95, 106, 107, 156] permits the reduction of the fast phase space modulations associated with the microbunching instability (section 2.3) [95-98] and to control the slice energy spread, as described in section 4.5. The laser heater (LH), described in section 2.3, consists of a short undulator located in a magnetic chicane through which an external laser pulse enters to longitudinally modulate the electron beam. The interaction within the undulator produces

an energy modulation of the electron beam on the scale of the laser wavelength. The last half of the chicane time-smears the energy modulation leaving an effective incoherent energy spread increase.

Shot-to-shot repeatability is an important parameter associated with time domain experiments. Ideally, for non-linear phenomena experiments, the shot-to-shot RMS jitter in normalized photon number should be 5% or less. Such a low value seems unlikely with the current expected accelerator and injector parameters. A large class of FEL1 experiments can tolerate values as high as 25% by recording the shot-by-shot photon number for post-processing. This kind of operation requires a wavelength jitter below the individual shot bandwidth in order to not increase the effective time-averaged, output bandwidth as seen by the user. For both FEL1 and FEL2, calculations based on time-steady input parameters and full start-to-end time dependent simulations were performed using the 3-D numerical codes Genesis 1.3 [160] and GINGER [161]. They predict a satisfactory shot-to-shot output stability for most of the planned experiments on both FEL1 and FEL2, if the following specifications for the electron beam stability are ensured at the entrance of the undulator: emittance jitter $\frac{\Delta\epsilon}{\epsilon} < 10\%$, mean energy jitter $\frac{\Delta E}{E} < 0.1\%$ and mean current jitter $\frac{\Delta I}{I} < 8\%$.

4.2 Emittance studies

At the present, the FERMI photoinjector provides 500 pC bunches, 2.8 ps long (RMS). The injector parameters optimization is routinely performed by measuring the Twiss functions and emittance of the beam after the first two accelerating sections (L0), at about 100 MeV, using the quadrupole scan method [88]. After minimizing the projected emittance by

tuning the RF gun phase and its solenoid, the beam optics is matched with Elegant code interfaced to the Tango server through Matlab scripts [162]. Measurements of the transverse parameters and optics matching are performed in the transport line, placed after L0, that also hosts the laser heater (figure 3.3). The projected emitance measured has a value of $\approx$0.8 $mm{\cdot}mrad$ in both planes. The beam is then accelerated and propagated up to the first bunch compressor. The slice parameters of the beam after the longitudinal compression can be measured with the low energy RF deflecting cavity (LERFD), located just after the first magnetic chicane (BC1) (figure 3.4). The beam is deflected by the deflector and then sent on a screen to measure its current and slice emittance (as the screen longitudinal coordinate corresponds, after the deflection, to the beam time coordinate). Figure 4.3 (left) shows the deflected beam on the second screen (figure 3.4) [126]. The integration of this image, over the x coordinate, yields the beam current profile. Slice emittance is measured on this screen with the quadrupole scan technique by varying the strength of the fourth quadrupole in figure 3.4. The measured slice horizontal emittance is plotted on the right of figure 4.2 (blue curve) with the reconstructed current profile (red curve). The normalized emittance in all the slices is below 1.5 $mm{\cdot}mrad$ and the current in the core of the bunch is around 600 A. The compression factor is CF=10 applied on the beam in BC1.

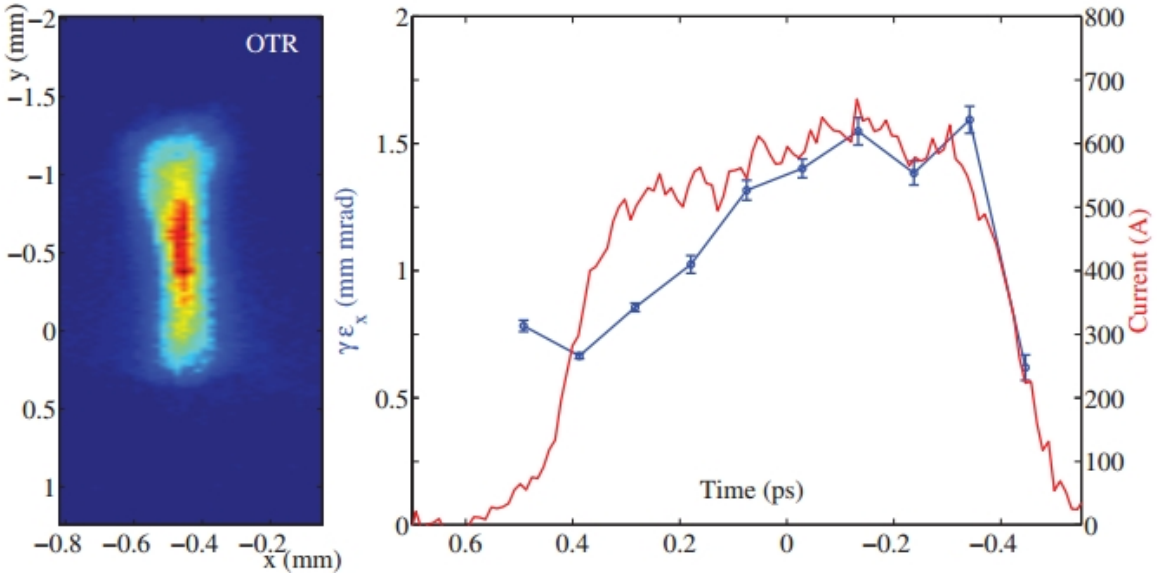

Figure 4.3: On the left: stretched beam spot acquired on the OTR target. On the right: current profile and slice emittance of bunch with a charge of 500 pC. Taken from [126].

For improving the emittance measurement accuracy we have used the OTR targets, that could provide a beam spot size estimate with 20 μm resolution. Nevertheless for high compression factors, the OTR targets suffer from coherent optical transition radiation that corrupts the beam spot image. This effect has been mitigated by the implementation of the X-band cavity that linearizes the longitudinal phase by flattening the beam current profile, and by the activation of the laser heater [108, 156] as will be described in section 4.6.

Up to this point the beam emittance meets the FEL requirement. The beam emittance can grow even after the bunch compressor due to transverse wake fields in the rest of the linac. It has been demonstrated that the trajectory in the accelerating cavity can be optimized to limit beam break up and emittance dilution [163] leading to a small growth of the projected emittance to a value of ≈1.5-2 $mm \cdot mrad$ while the slice emittance is preserved. The

spreader can also contribute to emittance growth, mostly by CSR. A scheme to compensate emittance dilution in a transfer line by CSR is described in [164] and applied to the FERMI's spreader and it allows to limits the final projected emittance to ≈2-2.5 $mm \cdot mrad$. FEL performance suggests that the slice emittance is preserved below the FEL tolerance. The limitation of the final projected emittane is important to take it close to the slice emittance. In this way the transverse matching in the undulator line is valid for all the slices.

4.3 Longitudinal phase space optimization

FEL1 operations require a regular and clean longitudinal phase space characterized by a low slice energy spread and a flat distribution of current and energy of the electrons beam over a time duration of 300-400 fs. Several elements tend to perturb the phase space. The first part of the linac, linac1 (figure 3.2), is run off crest to produce a linear chirp used to compress the beam. This introduces a quadratic chirp too as the particle acceleration is proportional to a sine function as seen in section 2.1. The main effect of the curvature in this part of the linac is to induce non-linearity in the beam compression leading to a non-flat current distribution. The curvature can be controlled with the X-band cavity. The beam energy profile and the beam current can be studied with the transverse deflector located after BC01. The beam is deflected by the vertical deflector and then sent on a screen to measure its current as the screen longitudinal coordinate corresponds, after the deflection in the deflector, to the beam time coordinate. The energy profile is imaged by vertically deflecting the beam, and sending it into a spectrometer bending magnet in which the beam trajectory is bent in the horizontal direction. This deflection maps the beam

longitudinal coordinate to the vertical coordinate on the spectrometer Yttrium Aluminium Garnet (YAG) screen, while the spectrometer magnet converts the energy of the beam to the horizontal coordinate on the same screen. Figure 4.4 shows the beam energy profile of the beam before the compressor with the X-band cavity switched off and on. The horizontal coordinate of the screen represents the energy while the vertical one is the longitudinal bunch coordinate.

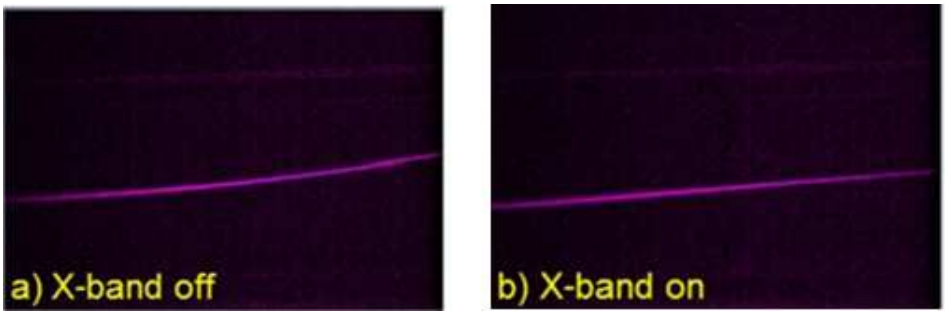

Figure 4.4: Electron beam energy profile. Courtesy of G. Penco.

We see that the energy varies linearly along the beam when the X-band cavity is switched on. The beam, vertically deflected, is then sent on the third screen in figure 3.4. The current profile reconstructed on this screen is shown in figure 4.4 for two linac configurations. The picture on the left shows the current profile obtained when the X-band cavity is switched off and compression factor is 5.6. This moderate compression factor is enough to produce a ramped current profile with a sharp horn. We will see, in section 5.1, that in this case the FEL process takes place in the ramped part of the beam in which the current is $\approx$200 A. The current profile obtained with the X-band cavity switched on and with a compression factor $\approx$10 is shown on the right. In this case the beam current is around 600 A in a flat region, around 300 fs long, good for FEL production. The beam charge is 500 pC in both

the cases shown in picture 4.5.

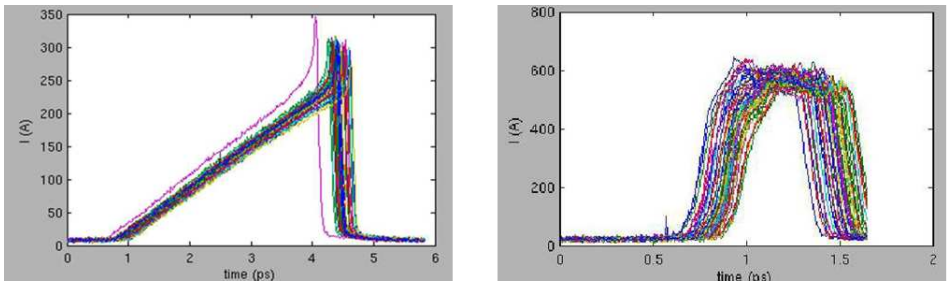

Figure 4.5: Beam current profile with X-band cavity off (left) and on (right). Courtesy of G. Penco.

As the beam propagates along the linac, its longitudinal phase space evolves under the effects of the accelerating section and collective effects such as the wake field and the longitudinal space charge. The residual linear energy chirp coming from the compression can be compensated by running the last cavities off crest. In this case these cavities can contribute to the quadratic curvature of the beam. The longitudinal wake fields in all the linac induce a strong curvature that remain on the energy beam profile at the end of the linac and can affect the FEL output. Shorter scale energy and density modulations are induced by microbunching instability and as we will see in section 4.6 can be controlled by the laser heater. It is important to measure and control the beam phase space at the end of the linac in order to preserve the FEL output performance. Measurements of the electron beam phase space are performed in the diagnostic section placed at the end of the linac described in section 3.1 (figure 3.5) (126). The beam is deflected vertically by the first HERFDY deflector, sent in the bending magnet (horizontal deflection) and imaged on the Yttrium Aluminium Garnet (YAG) screen (figure 3.5).

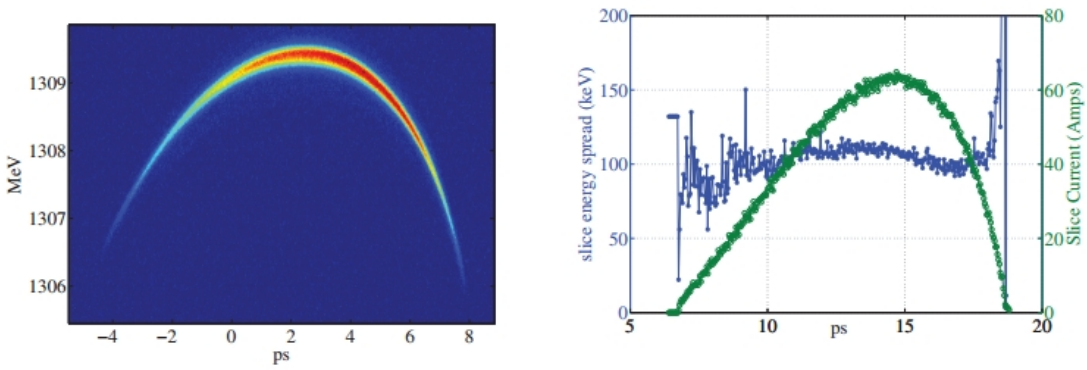

Figure 4.6: Characterization of the uncompressed bunch (500 pC): Longitudinal phase space (on the left) and slice energy spread and current profile (on the right). The energy spread reported here is obtained by screen measurements using pure chromatic approximation given by equation 2.16. Taken from [126].

Now we compress the beam and measure the phase space. Figure 4.7 reproduces the phase space (on the left) and the current and the energy spread (on the right) at the end of the linac when the beam is compressed by a factor 5.6 in BC1 without X-band cavity and laser heater. We see that part of the linear chirp, used to compress the beam, is still present. The bunch current profile presents a peak at the head of the bunch of about 380 A (on the left in figure 4.7). The high charge density around this peak induces strong energy and current modulations (i.e. microbunching instabilities) that are visible as three "hot spots" in the plot on the left. In this portion of the bunch the slice energy spread is large (about 300 keV) and the phase space is not regular and it shows current and energy modulation. This deteriorates the FEL performance in terms of spectrum and intensity, especially at high harmonics.

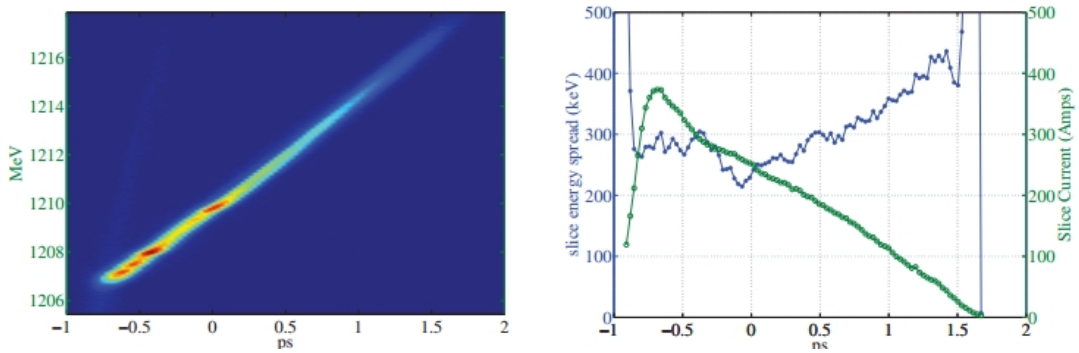

Figure 4.7: Left: longitudinal phase space at the end of the linac. The laser heater and the X-band cavity are switched off. All the RF sections, are on crest. Right: current and energy spread profile in the same linac configuration of the left figure. The energy spread reported here is obtained by screen measurements using pure chromatic approximation given by equation 2.16. Taken from [126].

Further compression, without activating the X- band cavity and the laser heater, enhances the head peak current, but at the same time increases the slope of the current profile, squeezing the good portion of the electron bunch useful for the FEL process. Also the microbunching increases. Using the X-band cavity and the laser heater, it is possible to compress the beam, preserving at the same time the phase space. Figure 4.8 reproduces the phase space, the current and the energy spread profiles at the end of the linac, when the beam is compressed by a factor of 10 in BC1 with the X-band cavity and laser heater switched on. The X-band cavity is set on the decelerating crest, linearizing the longitudinal phase space before BC1. This allows further compression, reaching a peak current of 500-600 A in a large portion of bunch. The X-band phase and tension are optimized to obtain a flat current in the core of the bunch. Furthermore the RF phase of the last two sections is set to +30deg (relative to the crest) to compensate the linear chirp. In this final configuration, a 300 *fs* long central portion of the bunch has a constant energy within 0.5 *MeV*, a good

slice energy spread (around 150-200 keV) and a peak current greater than 600 A.

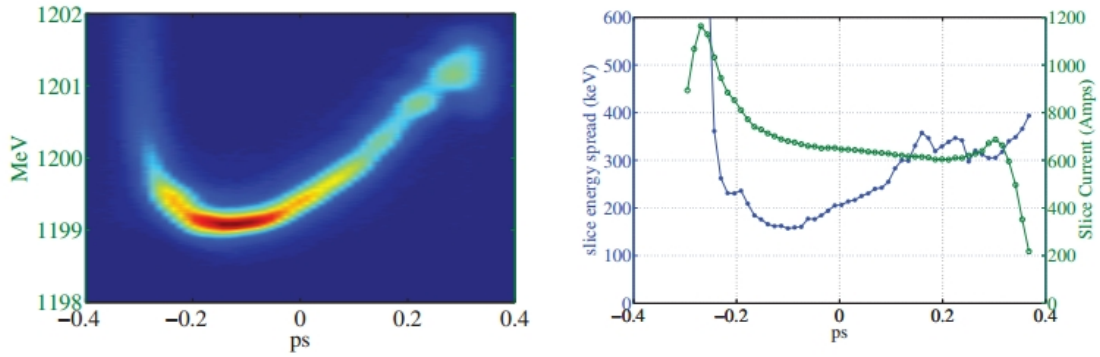

Figure 4.8: Left: longitudinal phase space at the end of the linac. The laser heater and X-band cavity are on and optimized. All the RF sections, with the exception of the last two are set to +30 deg off crest. The vertical axis of the plot on the left is scaled to resolve the residual quadratic chirp. Right: current and energy spread profile in the same linac configuration of the left figure. The energy spread reported here is obtained by screen measurements using a pure chromatic approximation given by equation 2.16. Taken from [126].

4.4 Design and implementation of a laser heater for FERMI

In this section we describe the laser heater implemented for FERMI [107, 156]. Figure 4.9 is a picture of the laser heater system installed in the linac tunnel.

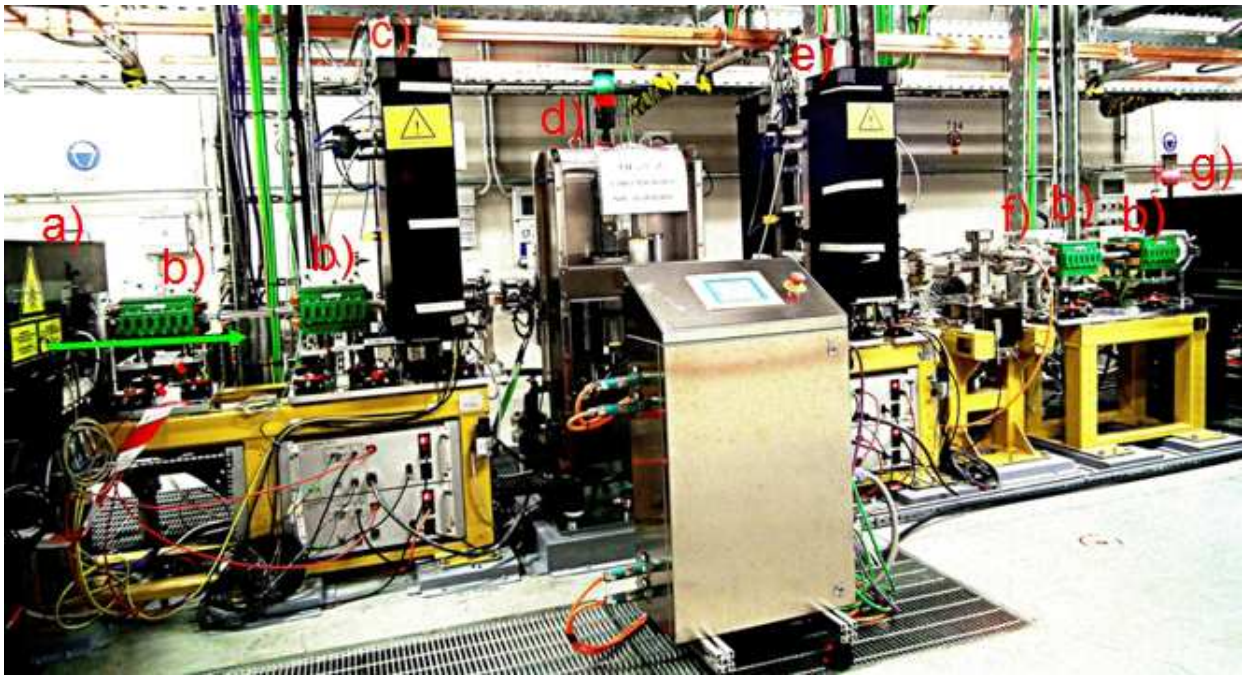

Figure 4.9: Laser heater system installed in the linac tunnel: a) input laser table, b) chicane magnet, c) multi-screen station LH01.02, d) laser heater undulator; e) multi-screen station LH01.02, f) BPM LH01.03, g) output laser table. The green arrow shows the direction of laser and electron beam.

The four dipoles shown in figure 4.9 form a chicane, shown in figure 4.10, that creates a horizontal bump in the beam trajectory. The first pair of magnets deflects the beam on a line, which is parallel to the linac axis at a distance of 0.03 m from it. Then the electron beam goes straight for $\approx$3 m before to be bent, by the second pair of magnets, on the linac axis. The undulator axis and the path of the laser used to heat the beam are collinear with the electron beam trajectory in the chicane.

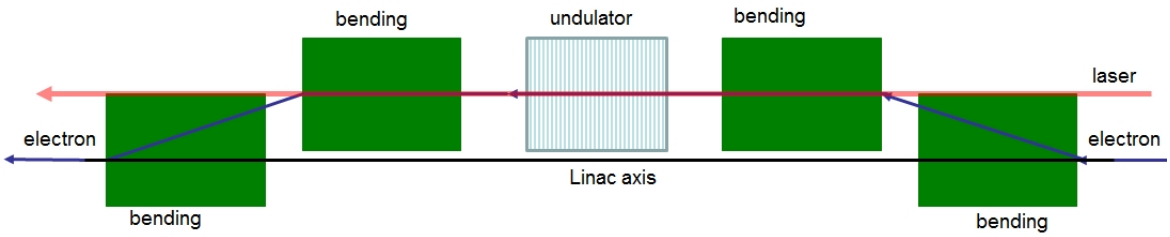

Figure 4.10: Electron beam trajectory in the laser heater chicane. The first pair of magnets deflects the beam on a line, which is parallel to the linac axis at a distance of 0.03 m from it. Then the beam is deflected again on the linac axis by the second pair of magnets.

The laser heater undulator is a simple planar permanent magnetic structure. The undulator parameters have been chosen to be resonant with the wavelength of the laser (783 nm) used to heat the beam. The electron beam energy at the heater location was not fixed, when the undulator was designed but was expected in the range from 85 MeV to 105 MeV. Therefore the undulator was designed to be resonant in this energy window with the wavelength of the laser. The resonant wavelength is determined by the undulator period, the beam energy and the K according to equations 1.4-1.5. We can use the following relation between the K_0 and the undulator gap for a planar undulator [24]:

$$K_0 = 160.77 \cdot B_r(T) \cdot \lambda_U e^{-\frac{\pi \cdot g}{\lambda_U}} \tag{4.1}$$

where B_r is the remnant field characterizing the permanent magnets used to build the undulator. In our case $B_r = 1.2\,T$. We calculate, from equations 1.4-1.5 and 4.1, the beam energy for which the undulator is resonant, at the laser wavelength, as function of the undulator gap for several values of the undulator period. The result is shown in figure 4.11 [107].

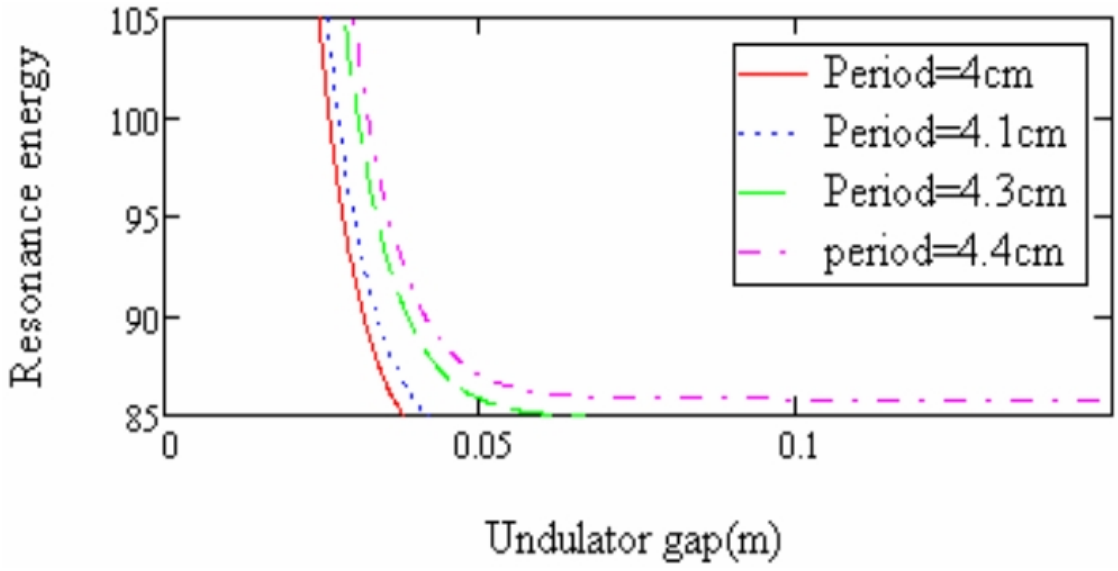

Figure 4.11: Resonance energy in vs. undulator gap. The undulator tunability has been evaluated for different undulator period lengths.

The undulator period determines the minimum energy at which the undulator is resonant and the minimum gap needed. In figure 4.10 we see that the undulator is not resonant at beam energy of 85 MeV for periods longer than 4.3 cm. We see even that periods shorter that 3.9 cm require a gap shorter than 20 mm. In this case the height of the vacuum chamber should be $\leq 18\,mm$. A period 4 cm long has been therefore chosen to allow using a slightly larger vacuum chamber that was easier to integrate in this part of the machine. The expected gap operation range is 24-32 mm. The number of periods has to be limited in order to have a large energy acceptance but large enough to ensure good efficiency as the energy spread added by the heater is proportional to the square root of the laser power and in a first approximation, neglecting laser diffraction, linear with the number of periods as shown in the equation 2.36. The actual number of periods of laser heater undulator is 12. This corresponds to a bandwidth of $\approx$8%. Simulations have been performed to validate

Parameter	Value
Undulator period	4 cm
Number of periods	12
Parameter K	0.9
Laser wavelength	783 nm
Laser energy	$1.4\mu J$
Laser peak power	0.130 MW
Laser pulse duration	10 ps (FWHM)
Laser beam sise	$200\mu m$
Electron beam size	140 μm
Electron beam energy	97 MeV

Table 4.1: Laser heater parameters used for simulations and theoretical calculation reported in figure 4.10.

the undulator parameters chosen and to estimate the laser energy needed to heat the beam adequately to suppress microbunching according to the calculation shown in figure 2.6 [97]. The simulations are performed with the parameters of table 4.1.

The figure 4.12. shows the results of simulations performed with the code elegant [165] and Genesis 1.3 [160]. elegant is a code that tracks the 6-D electron beam distribution across accelerator elements such as RF cavities and magnets. Collective effects, such as wake field CSR and longitudinal space charge, can be included. The simulations, done with elegant, of the laser heater don't include the FEL dynamics with gain and bunching. The code Genesis 1.3 can simulate the FEL process in an undulator starting from noise or from a coherent seeding and it is the widely code for the FEL simulations. elegant simulations of the laser heater have been validated with Genesis 1.3. The black points are obtained with elegant. The red curve reports results of the simulations done with Genesis 1.3. The blue line shows the expected theoretical behaviour of the induced energy spread after the laser heater, as function of the undulator length, expressed by the following equations:

$$\sigma_\gamma(L_U) = \sqrt{(\sigma_{\gamma_0})^2 + (\sigma_\gamma(L_U))^2_{Laser\,heater}} \tag{4.2}$$

$$(\sigma_\gamma(L_U))_{Laser\,heater} = \int_0^{L_U} \sqrt{\frac{\sigma_r^2(s)}{\sigma_x^2 + \sigma_r^2(s)}} \sqrt{\frac{P_L}{P_0}} \frac{K}{\sigma_r(s)\,\gamma_0} JJ(K) ds \tag{4.3}$$

See section 2.3 for the notation used here. The first term of the sum in equation 4.2 is the initial slice energy spread of the beam coming from the photoinjector. The second term is the energy spread added by the heater. The integration is on the longitudinal undulator coordinate. The electron beam dimension is constant to a good approximation along the undulator. Equations 4.2 and 4.3 are obtained from equations 2.36 and 2.38 and further modified to take into account the laser diffraction in the undulator. In equations 2.36 and 2.38 any quantity is considered constant along the undulator and the energy spread grows linearly along the undulator while in equation 4.3 the transverse dimension of the laser beam changes according to diffraction and integration permits to sum the contributions to the energy spread at any undulator location.

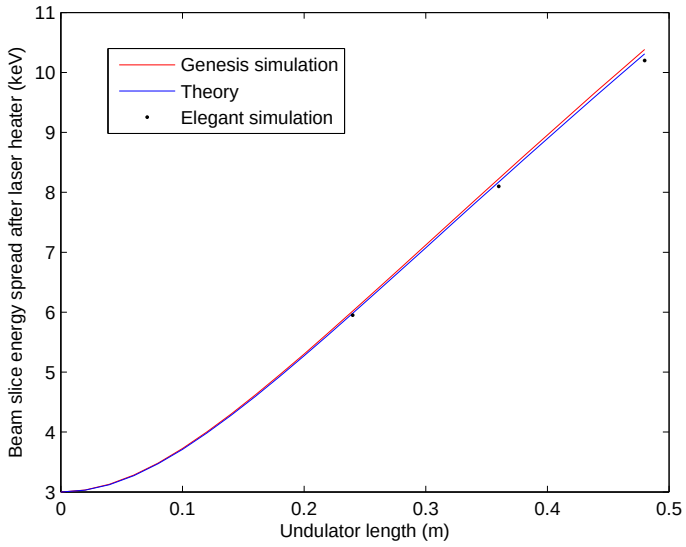

Figure 4.12: Behaviour of the energy spread added by the laser heater along the undulator. The red curve reports results of Genesis 1.3 simulation, The blue curve is obtained by the equation. The black points are obtained with elegant. The results of the three methods are in good agreements.

The results of the simulations with the two codes are in good agreements with the theoretical calculations. The results of simulations and theory shows that the chosen parameters of the undulator give the required energy spread, needed to suppress microbunching (figure 2.5), with a small laser energy of $\approx$1.4 μJ. It is then possible to use a portion of the photocathode infrared drive laser picked up before the crystal that produces the UV beam for the photocathode. The FWHM duration of the laser pulse is $\approx$*12 ps* and it is close to be twice the electron beam ($\approx$6.5 *ps* FWHM). Up to 160 μJ of energy are available for the heater after the beam transport corresponding to a peak power of $\approx$16 MW. This level of laser energy gives a measured energy spread of $\approx$*100 keV*; that is 10 times the optimum one fixed by simulations and linear theory (figure 2.5). The laser is transported on an optical

table placed in the linac tunnel, near the electron beam vacuum pipe and before the LH chicane. Two mirrors located on this table steer the laser beam to overlap with the electron beam trajectory. Another optical table is placed on the other side of the chicane to host additional diagnostics and the laser dump. Three CCD cameras looking at three screens permit to have replicas of the beam spot at the two ends of the undulator and at the centre of the undulator and this allows the laser position and spot size to be monitored. Sufficient space for two multi-screens, the undulator, the undulator correctors coils and one BPM has been allocated in the drift between the two pairs of dipoles. The chicane provides a useful temporal smearing of the laser-induced energy modulation, resulting in a random energy spread with no temporal structure. This smearing effect can be explained by analysing the beam dynamics in the second half of the laser heater chicane with the matrix formalism introduced in section 2.1. The longitudinal bunch coordinate (i.e., referred to the beam centre of mass) of a particle in a point f is related to the position at a starting point i, located just after the undulator, through the following first order equation:

$$z(f) = z(i) + R_{51}x(i) + R_{52}x^{'}(i) + R_{56}\frac{\Delta_L(r)sin\left(k_L z(i)\right)}{\gamma_0} \tag{4.4}$$

All the quantities appearing in equation 4.4 were defined in section 2.1 and 2.3. For a symmetric achromatic chicane the relevant coefficients across the half-chicane are $R_{51} = 0$ and $R_{52} = -\eta$ where η is the dispersion in the middle of the chicane and it is equal in a first approximation to the displacement between the linac axis and the beam trajectory in the middle of the chicane. This gives, $\eta \approx -0.03\,m$ in the centre of the laser heater chicane.

The smearing of the time-energy correlation (2.30) occurs because the path length from the chicane centre, where the energy modulation is induced, to the chicane end depends on the electron's x' coordinate across the non-zero chicane transport element R_{52} introduced in section 2.1. Particles, with different x' of a finite emittance beam ($\epsilon \neq 0$), move on different paths across the second half chicane. At coordinate i there is no x'-z correlation and at any longitudinal coordinate z there is an angular spread due to finite emittance. Particles at an initial longitudinal coordinate z(i), with different x', are spread on a slice of the bunch with an RMS length of $R_{52}\sigma_x^{'}$. The smearing of time-energy correlation (2.30), with the characteristic wavelength scale given by the radiation wavelength λ_L, occurs if the condition $R_{52}\sigma_x^{'} > \lambda_L/2\pi$ is satisfied. Where $\sigma_x^{'} = \sqrt{\frac{\epsilon_x}{\beta_x}}$ is the beam angular spread at the centre of the chicane. The angular dispersion at the centre of the chicane is $37\,\mu m$ and the dispersion is 30 mm for the FERMI case. So all the modulations with a reduced period much shorter than $\approx$1 μm are smeared while the reduced wavelength for the laser modulation is ($\lambda/2\pi = 126\,nm$). The laser heater energy modulation takes place in a dispersive region such that in principle it can produce a beam emittance growth. The laser energy modulation produces a growth of the longitudinal phase space area occupied by the beam dynamics as the energy spread is increased. The chicane dispersion couples the longitudinal dynamics to the transverse dynamics as the beam goes from the undulator's axis to the linac axis (see figure 4.10). So the area occupied by the beam in the transverse plane, i.e. the transverse emittance, is increased. The horizontal beam dimension after the chicane is:

$$\sigma_x = \sqrt{(\sigma_x)^2_{Twiss} + \left(\frac{\eta \cdot (\sigma_\gamma)_{Laser\,heater}}{\gamma}\right)^2} = (\sigma_x)_{Twiss}\sqrt{1 + \left(\frac{\eta \cdot (\sigma_\gamma)_{Laser\,heater}}{\gamma \cdot (\sigma_x)_{Twiss}}\right)^2} \quad (4.5)$$

Taking the values of the parameters in table 4.1 and a dispersion $\eta \approx 0.03\,m$ we obtain an increase in the beam dimension of 0.01% due to laser heater energy modulation and chicane dispersion. This level of emittance dilution is very small and completely acceptable. Two screen diagnostic stations, one on each side of the undulator, lie within the LH chicane. Both diagnostic stations are equipped with Cromox (Al2O3:Cr) screens on which it is possible to image both the laser and the electron beam in order to superimpose them transversely.

4.5 Commissioning of the FERMI laser heater

At the begin of laser heater commissioning the laser central wavelength had to be matched with that of the undulator spontaneous radiation and the electrons and laser beam had to been aligned transversely and superimposed longitudinally in the laser heater undulator. The relative bandwidth of undulator radiation is ≈8%, while the electron beam energy is known with an error of less than 1% and the undulator magnetic field, at which the parameter K is proportional, is measured with at error of 0.3%. Therefore it is very easy to find the resonance with an acceptable accuracy, as the reduction of induced energy spread due to these errors is less than 10% as can be seen in figure 4.21. The mechanic undulator gap control, allows the vertical position of the undulator axis to be changed to centre the undulator axis on the beam. We have then aligned vertically the axis of the undulator on the beam trajectory looking at the trajectory downstream both with undulator open and with undulator closed. Since both the electron beam and the external laser originate from the photocathode infrared drive laser, they are naturally locked in time but with a constant temporal offset: After the beam splitter that takes out the portion of laser used to heat the

beam, they follow two different paths to meet again after about 20 m. This temporal offset can be measured with an accuracy of about 300 ps, by recording with an oscilloscope the signal coming from a photodiode located at the LH input laser table and a signal of one beam position monitor (BPM) located near the chicane. The fine temporal overlap is then found by scanning a delay line to superimpose the two beams temporally, while checking the beam heating on the beam spectrometer as we will see later. Three remotely controllable mirrors, one in the laser room and two on the optical table at the chicane entrance, permit the adjustment of the laser centroid position relative to that of the electrons with 100 μm accuracy, as shown in figure 4.13. The laser transverse profile imaged on the two screens at both the ends of the undulator is shown on the left while on the right we can see the two images of the electron beam.

The BPM placed in the chicane allows any change in the electron beam energy to be monitored. When the electron beam and the laser beam are aligned in space and time, the laser-electron interaction in the undulator generates significant energy spread that is easily detected using the spectrometer placed after the first bunch compressor (figure 3.2). The beam is deflected vertically with a vertical RF deflector [126-128] before entering into the spectrometer. The magnetic lattice produces a momentum-dispersion $\eta \approx 0.58\ m$ and a betatron function $\beta \approx 1\ m$ at the YAG screen location. On the screen placed after the spectrometer dipole it is possible to reconstruct the beam longitudinal phase space, so enabling the measurement of the uncorrelated energy spread in each longitudinal slice of the bunch. Figure 4.14 shows a representative longitudinal phase space when the LH is switched off (left) and when the beam is heated (right), at full energy (160 μJ). The minimum slice energy spread, measured in pure chromatic approximation (equation 2.16) when the LH was

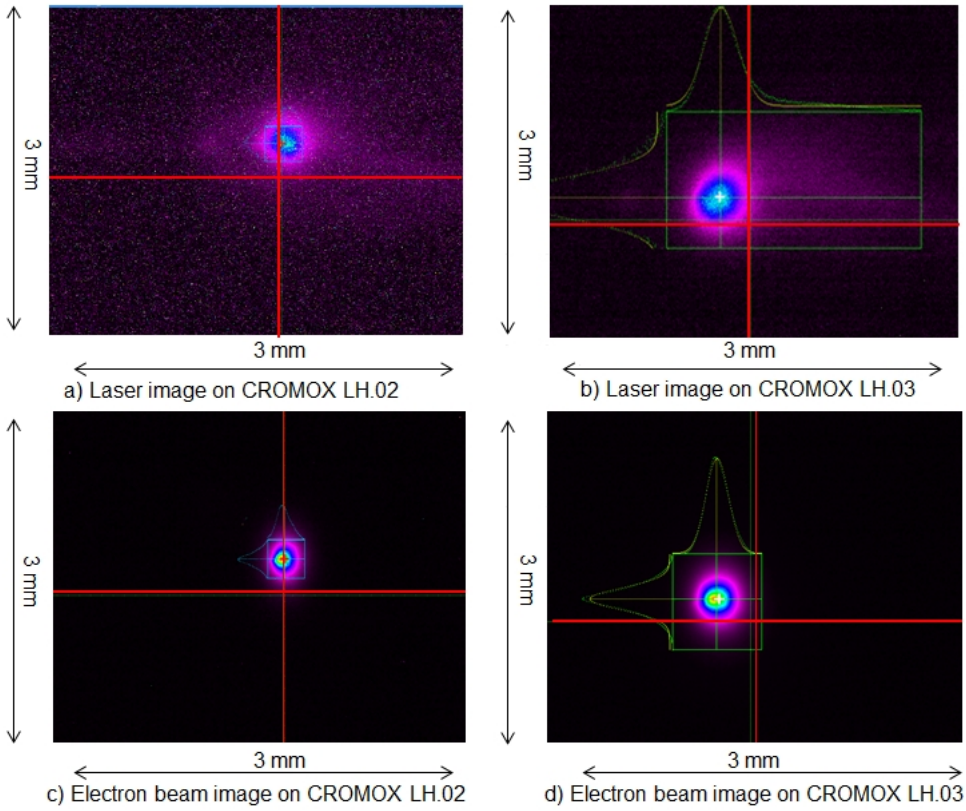

Figure 4.13: Image of laser (a and b) and electron beam (c and d) on two CROMOX screen targets at the undulator entrance (a and c) and exit (b and d). The red cross indicates the centre of the screen.

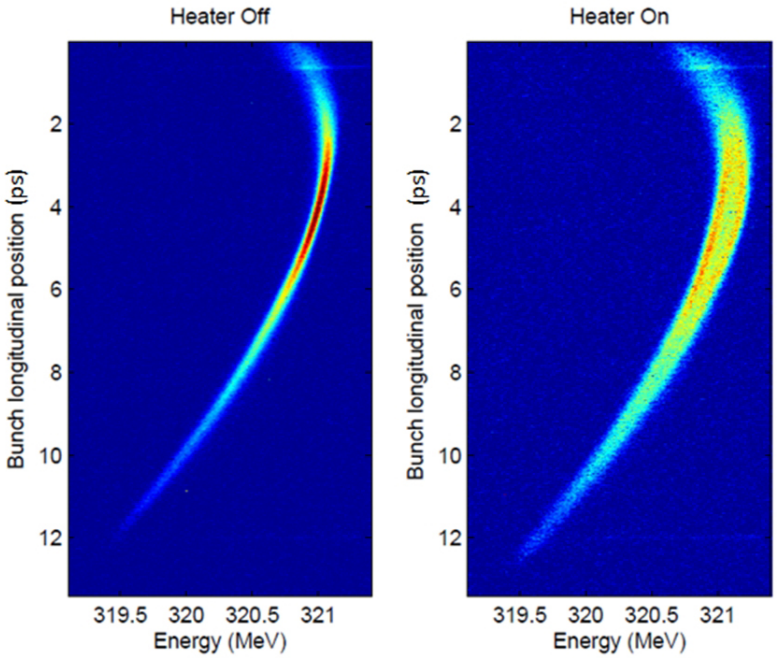

Figure 4.14: Longitudinal electron beam phase space reconstructed on the spectrometer screen with the RF deflector on. The left image is taken with the laser heater off. The right image shows the beam phase space with the heater on with a laser energy of 160 μJ.

off, is $\approx$40 keV. The nominal lattice geometry resolution is $\approx$*20 keV*, the screen resolution gives $\approx$20 keV and deflector adds $\approx$28 keV [129]. The transverse RMS dimension of the laser beam in the undulator is around $\approx$200 μm, while the electron beam size is $\approx$140 μm. The heated beam is expected to show a double horn energy distribution [95, 107] when the laser transverse profile is larger than the electron beam, as shown in figure 2.4. The energy distribution is more Gaussian-like when the laser matches the electron beam size in the undulator. This configuration has been shown to be more effective in suppressing the microbunching instability [95] as seen in section 2.3. In spite of this, we started with a large laser spot to more easily overlap the electron and the laser beam.

Figure 4.15 shows the longitudinal behaviour of the slice energy spread along the beam

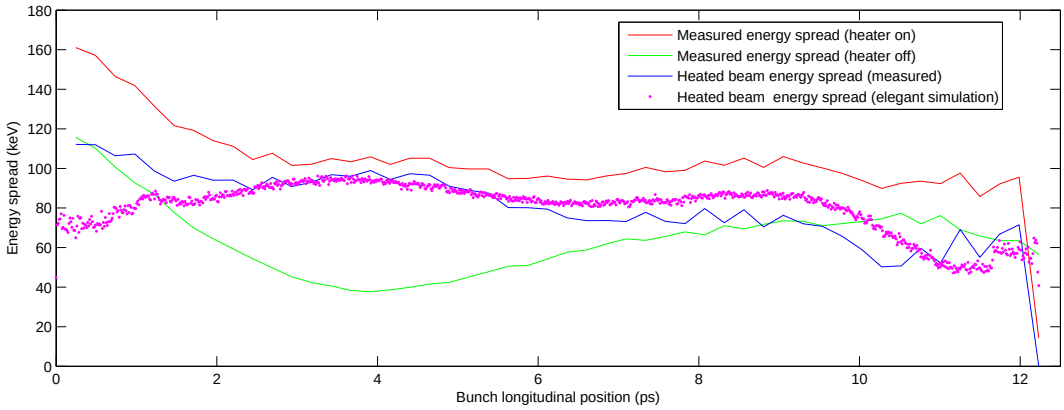

Figure 4.15: Slice energy spread along the longitudinal beam profile. The green curve shows the energy spread measured with the LH off, the red curve reproduces the energy spread of the beam heated at the maximum laser energy of 160 μJ and the blue curve is obtained subtracting in quadrature the green curve from the red one. The magenta line shows the slice energy spread along the longitudinal electron beam profile obtained with elegant.

profile. The green curve shows the energy spread measured with the LH off, the red curve reproduces the energy spread of the beam heated at the maximum laser energy of 160 μJ. The blue curve is the LH induced energy spread only, obtained by subtraction in quadrature of the first two. We see that the variation of the beam heating is about 20% on a central portion of the beam with a duration of $\approx$7 ps. This seems a good uniformity of the beam heating on the region of the beam on which the FEL pulse is produced. The magenta line shows the energy spread slice profile as obtained from an elegant simulation. It is again in good agreement with the experimental result (blue curve).

Figure 4.16 shows the evolution of the energy spread of a central slice of the beam as a function of the laser energy. The values shown by the blue experimental points are obtained by subtracting in quadrature the energy spread measured with LH off from the value measured with LH on. Doing so, one ideally obtains the energy spread added by the

laser heater only. The magenta line shows the expected theoretical behaviour (equation 4.3). The error bars are obtained from statistical measurement errors on 15 shots.

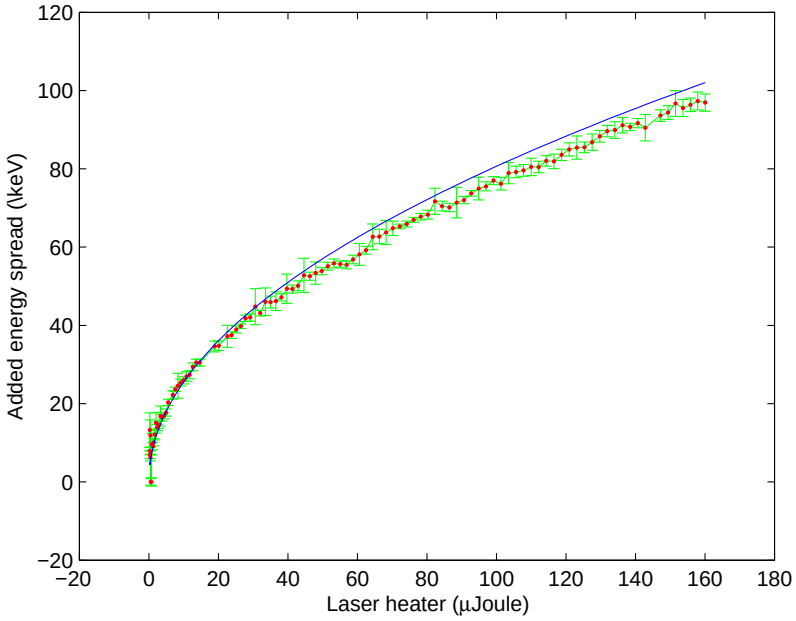

Figure 4.16: Laser heater added slice energy spread vs. laser energy.

Figure 4.16 shows a good agreement between theory and the measured data. The measurements reported above are taken with the gap optimized for the maximum beam heating. In figure 4.17 we show the behaviour of the added energy spread with a laser energy of 160 μJ as a function of the undulator gap. The blue curve shows the theoretical expected behaviour. The green points in figure 4.17 with the error bars are the measured values of the energy spread, added by the laser heater to a central slice, for several values of the undulator gap. The blue curve reproduces the theoretical behaviour of the energy spread, that is proportional to the sinc function of the detuning between the laser wavelength and

the undulator resonance wavelength [32, 33], as a function of K (see equations 1.4-1.5):

$$\sigma_\gamma(g) = \sigma_\gamma(g_L) \left| \frac{sin\left\{\frac{\pi N[\lambda(g)-\lambda_L]}{\lambda_L}\right\}}{\frac{\pi N[\lambda(g)-\lambda_L]}{\lambda_L}} \right| \tag{4.6}$$

$$\lambda(g) = \langle \lambda_\theta(g) \rangle_\theta \tag{4.7}$$

$$\langle \lambda_\theta(g) \rangle_\theta = \left\{ \frac{\lambda_U}{2\gamma_0^2} \left[1 + \frac{K(g)^2}{2} \right] \right\} + \frac{\epsilon_n \gamma_0}{\beta} \left(\frac{\lambda_U}{2\gamma_0^2} \right) \tag{4.8}$$

Here g is the undulator gap, ϵ_n is the normalized beam emittance and β is the average betatron function in the undulator. Equation 4.6 is valid for a beam propagating along the undulator axis without an angle. In reality, every particle has an angular divergence with respect to the straight reference axis, due to the beam finite emittance. The mean resonance frequency $\lambda(g)$ is then obtained mediating on the beam angular divergence and is shifted with respect to the case of a 1-D beam, by a term determined by the emittance and the betatron function in the undulator. This shift is the second term in 4.6. The beam in the LH has a normalized emittance $\approx$1 $mm{\cdot}mrad$, and $\beta\approx$2.5 m. The wavelength shift due to the finite emittance is then $<$0.01% of the wavelength resonance for a zero emittance beam. The magenta line in figure 4.17 is obtained by shifting the blue curve to match the experimental points. This shift corresponds to an electron beam energy of 97.2 MeV instead of 97.7 MeV. This shift is compatible with the expected error of the undulator calibration curve and of beam mean energy error measurement.

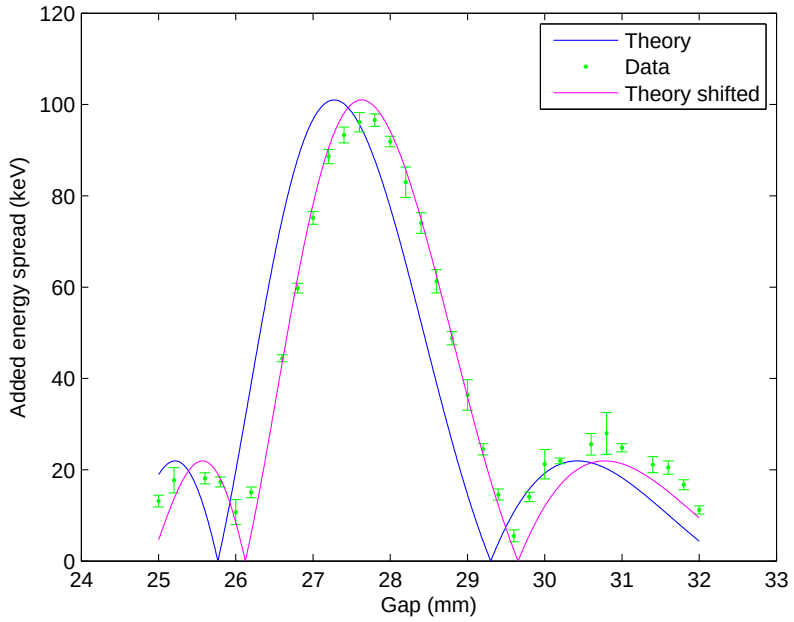

Figure 4.17: Electron beam slice energy spread added by the heater vs. undulator gap (mm).

4.6 Microbunching suppression

Now we analyse the effect of the LH on the electron beam dynamics downstream of the compressor. Clear evidence of microbunching instability effects can be seen when the linac is set to a compression factor greater than 3 as both the current and energy spectrum of the beam appear to be modulated. Figure 4.18 shows the electron beam energy profiles imaged on the screen of the spectrometer line in the diagnostic beam dump (DBD in figure 3.5), placed at the end of the linac.

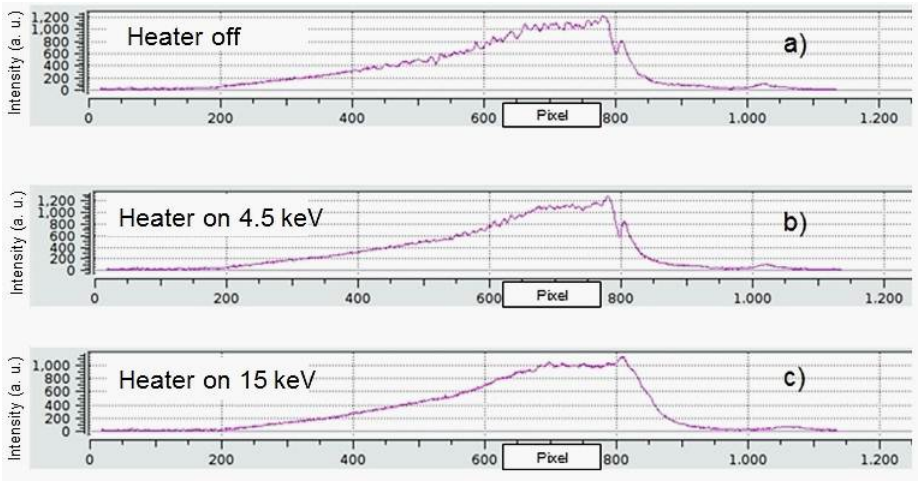

Figure 4.18: Beam energy profiles imaged on the screen of the spectrometer in the diagnostic bean dump (DBD) for three levels of beam heating. a: 0 heating. b: 4.5 keV heating. c: 15 keV heating.

These data were acquired for a 500 pC beam charge with a compression factor of about 5.5 using only BC1. The X-band RF cavity (so-called linearizer) upstream of BC1 was switched off so that a non-linear magnetic compression produced a triangular current distribution. The magenta curve in figure 4.18a displays the energy profile measured with the LH switched off. It shows high frequency modulations that we attribute to the microbunching instability,

together with a longer time-scale structure produced by non-linearities during the magnetic compression. When the LH is turned on with a laser energy of $\approx$0.25 μJ, the high frequency structures start to be reduced in amplitude (figure 4.18b), whereas the macroscopic current structures were almost untouched by this small level of heating. When the laser energy was increased to a level of $\approx$2 μJ or greater, even the longer scale structures were smeared out, as shown in figure 4.18c.

The suppression of the phase space modulation, seen as a smoothing of the beam energy spectrum in figure 4.18, can be seen clearly by deflecting the beam with the vertical deflector and then bending it with a horizontal dipole magnet [164]. Figure 4.19 shows the beam phase space imaged on the spectrometer screen. We see, on the left of the picture, that the LH suppresses the microbunching structures located at the head of the beam.

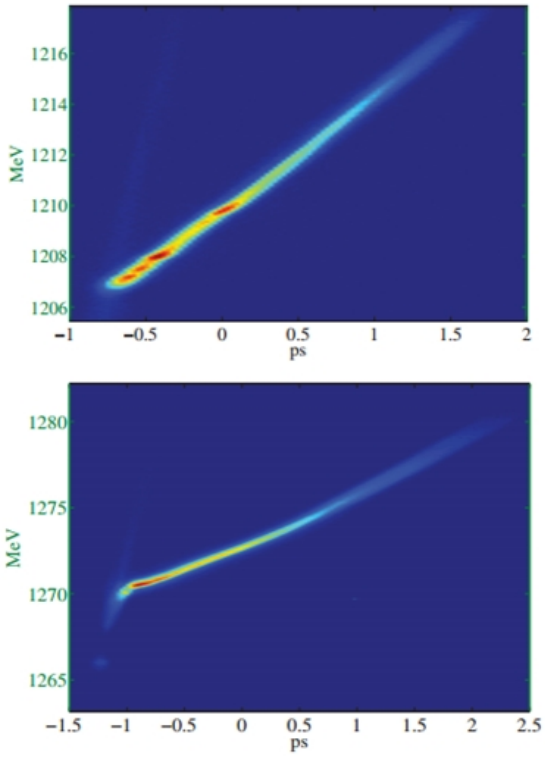

Figure 4.19: Beam longitudinal phase space at the linac end. Top: no LH and no X-band cavity, all RF sections on crest, 500 pC. Bottom: LH on but without X-band cavity, all RF sections on crest, 500 pC. Taken from [126].

Further evidence of microbunching instability gain is the coherent optical transition radiation (COTR) produced when the beam passes through OTR target screens [130, 166, 167]. The LH reduces and eventually suppresses these COTR signals. Figure 4.20 shows the OTR signal from screen SFEL01.02 placed just upstream of the FEL1 undulator as a function of LH energy. One sees a strong suppression of the signal for laser energies exceeding 1 μJ. The data reproduced here are taken with 350 pC charge, a compression factor close to 10 and the X-band cavity switched on to have a more regular final current profile. The beam is compressed using only BC1. The COTR from SFEL01.02 is strongly suppressed,

with a charge of 500 pC and a compression factor of 10. The signal, from this screen, can sometimes remain 10%-20% higher with respect to the incoherent level if CSR, microbunching and dispersive effect are not completely controlled in the spreader [97]. This level of coherent radiation however corresponds to a very small persistent microbunching.

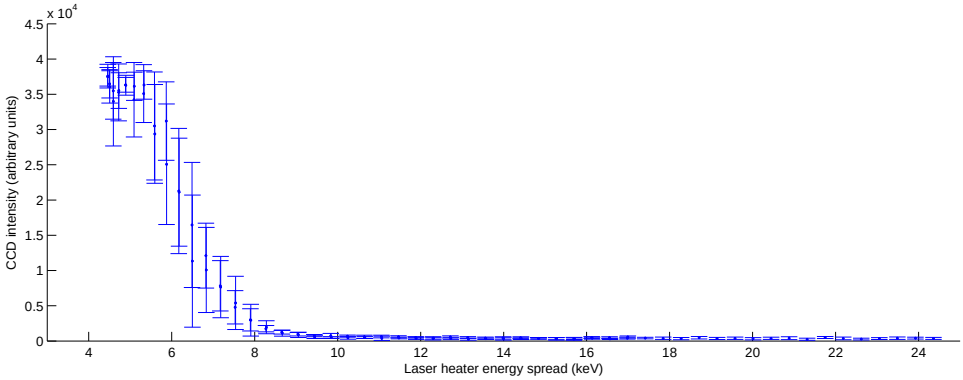

Figure 4.20: OTR intensity vs. laser heater energy.

The intensity decays as the laser energy is increased and approaches a constant level when the laser energy is above 1.0 μJ. This constant intensity is equal to the incoherent level obtained by inserting an upstream OTR screen on the beam path. We therefore conclude that the LH can suppress almost completely, in this linac configuration, the COTR produced on this screen when the laser energy is >1.0 µJ. More precisely, by adding an uncorrelated energy spread larger than 8 keV RMS, one removes completely any beam modulations detected by the CCD (within the wavelength range 0.2 μm - 0.9 μm). We then increased the beam charge to 500 pC, keeping unchanged the remaining linac setting and we studied the effect of the LH on the intensity of the OTR radiation produced by the third screen placed on the straight line after BC01. Figure 4.21 depicts the intensity of the signal collected by a CCD that looks to this OTR screen.

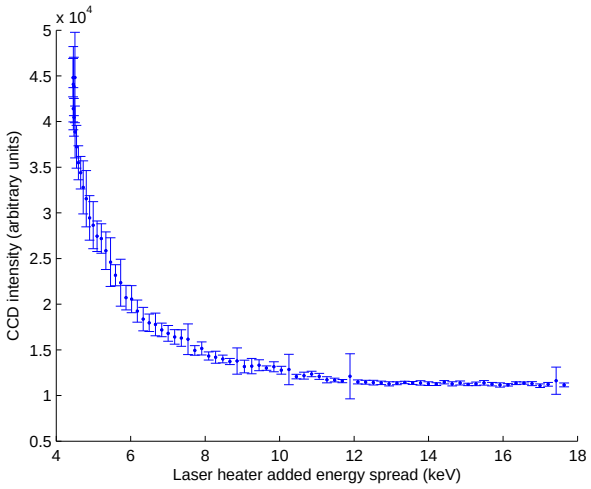

Figure 4.21: OTR intensity vs. laser heater energy.

The intensity decreases as the laser energy is increased and approaches a constant level when the laser energy is above 1 μJ. As in the aforementioned case, we conclude that the LH can suppress almost completely any beam modulations, between 0.2 μm and 0.9 μm, when the energy spread added by the LH is >8 keV. We see that complete suppression of microbunching in the linac allows the use of the OTR screens rather than lower resolution YAG targets for measurements of the transverse and longitudinal particle distribution. Figure 4.22 shows the transverse beam profile imaged on the screen BC01.03, located downstream of BC1, on which the transverse emittance is measured.

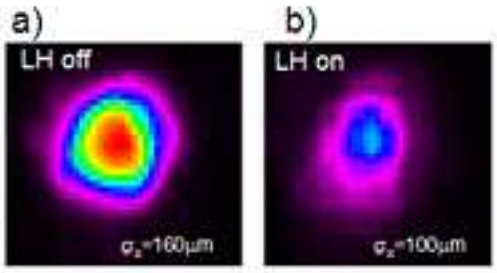

Figure 4.22: Transverse beam profile imaged on the screen BC01.03, respectively with LH off (left) and on (right). Picture from [162].

All the measurements reported above, about the laser heater and microbunching suppression, were performed with a laser spot larger than the electron beam. After this first operations the laser spot was reduced to about $130\,\mu m$ to better match the electron beam producing a more homogeneous energy distribution. This is more useful in suppressing the microbunching but it makes more difficult to get and maintain the overlap between the electron and the laser beam. The figure 4.23 shows the characterization of the laser heater with the laser matched to the electron beam.

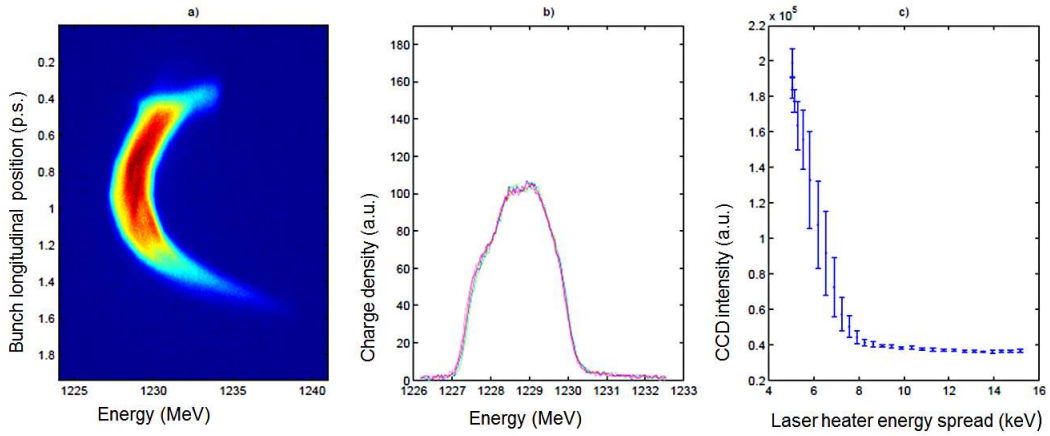

Figure 4.23: Characterization of the laser heater with the laser transversely matched to the electrons. a: Beam longitudinal phase space at the linac end (DBD spectrometer in figure 3.2). The beam is heated and the energy spread is increased to 75 keV by a laser with an energy $65\,\mu J$ and a transverse spot of $130\,\mu m$. The beam is compressed by a factor about 10 in BC1. b: Energy distribution of four central slices of 75 fs around the position at 0.9 ps of figure 4.23a. c: Intensity of OTR screen at the linac as function of the beam heating.

The data reproduced here are taken with 500 pC charge and a compression factor close to 10. The beam was compressed using only BC1 and the X-band RF cavity to have a more regular final current profile. Figure 4.23a shows the beam longitudinal phase space imaged on the DBD spectrometer (figure 3.2). The beam is heated and the energy spread is increased to 75 keV by a laser with an energy of $65\,\mu J$ and a transverse spot of $130\,\mu m$. This high level of heating clearly shows the shape of the energy distribution of the heated beam despite the finite spectrometer resolution of $\approx$75 keV. The energy distribution of four central slices of about 15 fs around the position at 0.9 ps is shown in figure 4.23b and it has a shape close to that expected for a beam heated by a laser matched to the electron beam (figure 2.4). Figure 4.23c shows the intensity of OTR screen at the linac as function of the beam heating. We see a complete suppression of the coherent optical radiation, and

of the density modulation, at the wavelengths visible to the CCD, 0.2-0.9 nm, for a heating higher than 8 keV. All these measurements show that this laser heater setting is working well despite the practical difficulties to take and keep a good alignment, between the laser and the electron beam, with a so tight laser spot. This spot size has been maintained for the last measurements shown in this chapter, for the FEL measurement shown in the next chapter and during FEL user operations. We measure the beam slice energy spread in the diagnostic area placed at the linac end (figure 3.2). We have done measurements of the final slice energy spread while compressing the beam with only the first compressor and even with both compressors. The single compressor scheme permits to obtain a smaller value of slice energy spread with respect to the double compressor scheme and this confirms the theoretical and numerical calculation reported in section 2.3. A minimum slice energy spread of about 100 keV has been measured, in the single compression scheme, for a compression factor of 10-12 and with an energy spread added by the heater $<$10 keV [168]. In this configuration the expected minimum (figure 2.6) of the final energy spread versus the added energy spread was not seen during measurements due to the finite experimental resolution. We will see in the next chapter that the FEL output power is maximized for a proper value of the beam heating revealing, probably, a minimum of the slice energy spread. On the other hand the microbunching is stronger in the double compression scheme and, for this reason, the minimum of the final energy spread obtained for the proper value of heating is more visible. Figure 4.25 shows the beam slice energy spread as function of the energy spread added by the heater in the double compressor configuration. Each energy spread value is the mean of seven measurements. The expected spectrometer resolution is $\approx$50 keV; another contribution of 50 keV to the measured energy spread is expected by the deflector

while the CCD pixel dimension is equivalent to 20 keV on the measurement resolution. We suppose that these independent contributions can be added in quadrature to give the measurement resolution. So we subtract in quadrature a total of 75 keV from the measured energy spread to produce the values shown in figure 4.25. We suppose an error of 5 keV on this experimental resolution. The error bars in figure 4.25 are the result of statistical measurement error over seven shots.

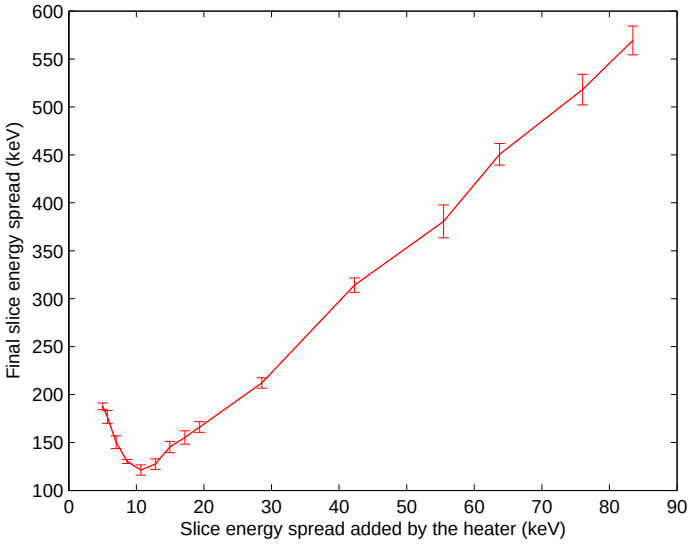

Figure 4.24: Slice energy spread as function of the energy spread added by the heater in the double compressor configuration.

The reduction of the slice energy spread, as result of microbunching suppression by the laser heater, is evident in the low heating part of the curve. The microbunching is suppressed for an optimum slice energy spread added by the heater corresponding to about 10 keV. The slice energy spread, corresponding to this value of the energy heating, is 120±10 keV. A further increase in heating results in more energy spread due to beam compression and

phase space conservation. The measurements taken at high values of added slice energy spread are less affected by the measurement errors and by the initial beam energy spread. The measured energy spread, at high values of beam heating, is the result of the compression of the heated beam. From the last six points appearing in figure 4.24 it is possible to derive a compression factor of about 7. This is in good agreement with the current measured in the linac condition at the moment of data collection. In fact we measured an initial current of $\approx$60 A and a compressed current of $\approx$400 A.

In conclusion we have shown that it is possible to control the microbunching instability in the FERMI linac using the laser heater. A reduction of density and energy modulation due to the laser has been observed as well as a reduction of the slice energy spread.

Chapter 5

FERMI FEL1 commissioning

Here we report a detailed characterization of recent results obtained with FEL1. The X-band cavity and the laser heater were not available during the first year of FEL commissioning. The compression is non-linear without the X-band cavity and this lead to a current ramp distribution. During this first period the beam compression factor used was around 5.6. The clean longitudinal phase space allows a very good control of the FEL bandwidth, however the low current used in this period implies a quite low photon flux. With the use of the X-band cavity and of the laser heater it has been possible to increase the beam current and thus the photon flux. By following the evolution of the FEL performance in terms of the spectrum and FEL power it is possible to study the influence of the phase space on the FEL characteristics. We have observed that the ramped current distribution obtained by gently compressing the 500 pC bunch in the absence of the X-band cavity and of the laser heater allows a clean, narrow and stable spectrum but a mild-low photon flux. Increasing the compression factor to 10-13 with the laser heater and the X-band cavity preserves the

beam quality while giving a increase in the pulse energy (almost a factor 10-15) preserving the spectral quality.

5.1 High-gain harmonic generation

The harmonic radiation produced in the FEL process reaches a power level considerably lower than that of the fundamental component which decreases as the harmonic number increases [37]. A more efficient scheme to produce coherent radiation at the harmonics of the seed can be realized using two undulators with the first undulator, the modulator, tuned to the same wavelength of the external laser and the second one, the radiator, tuned to the selected harmonic of the seed. A dispersive section, in which particles with different energy travel along different paths is placed between the two undulators. The energy of the particles at the end of the first undulator is correlated with the phase of the electromagnetic field of the laser, because the sign of the energy exchange due to the Lorentz force depends on this phase, and with the electron position within the bunch. The interaction between the external laser and the electron beam in the first undulator produces a sinusoidal energy modulation with the period of the seed laser and a modulation amplitude as described in section 2.3. The magnetic field of the dispersive section forces electrons with different energies to follow different paths. Therefore, the beam energy modulation with the spatial period equal to the wavelength of the seed laser is converted into a density modulation. The Fourier analysis of the beam current shows that components at the harmonics of the seed are present. The bunching factor at any harmonic of the wavelength of the seed laser has, at the exit of the dispersive section, the following expression:

$$b_n = J_n(nkR_{56}\frac{\triangle\gamma}{\gamma_0}) \cdot exp(-\frac{n^2k^2R_{56}^2}{2}\frac{\sigma_\gamma^2}{\gamma_0^2}) \tag{5.1}$$

The bunching at the nth harmonic is proportional to the Bessel function of the nth order with an argument that represents the harmonic phase shift performed by the electrons in the dispersive section. The Bessel function of the nth order has its maximum when its argument is comparable with its order number, then a relevant bunching comes for $kR_{56}\frac{\triangle_L}{\gamma_0} \approx 1$. The exponential factor shows that energy spread reduces microbunching when $nkR_{56}\frac{\sigma_\gamma}{\gamma_0} \approx n\frac{\sigma_\gamma}{\triangle_L} > 1$, so for a given energy spread it is possible to produce a good bunching down to the nth harmonic of the seed with $n_{max} < \frac{\triangle_\gamma}{\sigma_\gamma}$. The beam thus goes into the second undulator, the radiator, that is tuned to one of the harmonics of the seed laser. The beam is just bunched on the fundamental wavelength of the radiator and coherent emission starts without lethargy time. In the first part of the radiator, shorter than one gain length, the beam distribution does not change and a series of bunches radiate coherently producing a linear growth of electric field amplitude and a quadratic growth of the power. After one gain length the radiation emission produces a relevant energy modulation and after a couple of gain lengths even the beam modulation begins to evolve. Now the growth of the radiation is followed by growth in the bunching coefficient at the fundamental harmonic of the radiator and of the emitted radiation. The radiation is now growing exponentially along the undulator up to saturation. The field dynamics in the radiator is controlled by the Pierce parameter ρ and by the gain length defined in section 2.4. The amplitude of the relative energy modulation gained by the electron beam in the modulator has to be

smaller than the Pierce parameter of the radiator otherwise many particles fall outside of the resonance too early and the FEL interaction is reduced. The limitation on the harmonic order that can be reached becomes $n_{max} < \frac{\sigma}{\sigma_\gamma}$ and the energy modulation induced in the modulator has to be in the range of $n\sigma_\gamma < \triangle_\gamma < \sigma$ where n is the harmonic number to which the radiator is tuned. A bunching of few per cent, on the harmonic to which the radiator is tuned, is enough to overcome the shot noise and ensure an increase of the radiation in the second undulator. Another stage with a modulator a dispersive section and a radiator, using the radiation coming from the first radiator as seed, can follow the first one. The radiation production in the first stage can decrease the beam quality increasing the slice energy spread. This unwanted phenomenon occurs mainly on the part of the beam that interacted with the seed in the first stage as seeded FEL can be optimized to evolve faster than SASE. Then it is enough to add a delay line for the electron beam, between the two stages to put the seed produced in the first stage on a fresh part of the electron bunch. This technique is called fresh bunch and it will be explored for the first time on FERMI's FEL2 line.

5.2 Low compression scenario

For the FEL1 experiments reported in this section the seed laser was the third harmonic (260 *nm*) of the Ti:Sa laser. The seed laser pulses had a duration of 150 *fs* (FWHM), a peak power of about 100 *MW* and a bandwidth of about 0.8 *nm*, which is about a factor 1.2 larger than the Fourier limit, assuming perfectly Gaussian pulses. The electron beam had a charge of 450-500 *pC* and was compressed by a factor 3-4 in BC01, without the

Parameter	Value
Energy	1.24 GeV
Slice energy spread (RMS)	<150 keV
Emittance (projected)	~ 4 $mm\cdot mrad$
Charge	400 pC
Peak current	200-300 A
Beam size	150 μm
Pierce parameter	1.3 10^{-3}

Table 5.1: Measured electron-beam parameters used to operate FEL1 in the experiments reported in this paragraph.

X-band cavity and the laser heater. The measured values of electron-beam parameters used to operate FEL1 in the reported experiments are listed in the table 5.1

The beam phase space is shown in figure 4.7. The temporal coarse alignment and spatial alignment were done, as described in section 3.1, before establishing seeding operation. The dispersive section was switched on to a value of $50 - 70\,\mu m$, the gap of the modulator and of the radiator were tuned respectively to the nominal value for the seed wavelength (the modulator) and of the desired harmonic (the radiator). Then, the seeded FEL was switched on by scanning the delay line. Figure 5.2 shows the FEL output energy versus the seed delay. This scan gives an indication of the temporal duration and shape of the electron beam region involved in the photons production. We will see later that it is possible to demonstrate that the interaction happens in the tail of the bunch for positive delays in figure 5.1 and in the head for negative delays.

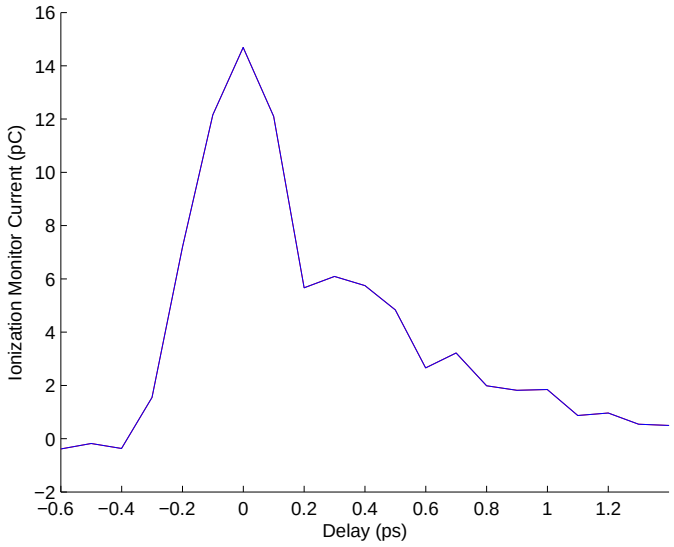

Figure 5.1: Seed delay scan. The temporal delay between the seed and the electron beam is scanned while recording the FEL intensity on a diode. In this way it is possible find the perfect time overlap between the two beams.

The curve reproducing the FEL intensity vs. the seed delay is asymmetric and inherits the principal characteristic from the beam current (green curve) and energy spread profile (blue curve) shown in figure 4.7. The FEL energy, as the seed is moved from the tail to head, increases almost proportionally with the square of the beam current. The growth of the FEL power stops before the current peak shown in figure 4.7 (green curve) as this part of the beam is spoiled by the microbunching that increases the energy spread and modulates the phase space as can be seen in figure 4.7. The FEL energy goes down rather quickly with the current. The full width half maximum (FWHM) duration of the curve in figure 5.1 is about 300 *fs* and this can be considered as the temporal duration of the part of the beam that fits the requirements of FEL.

We obtained several tens of microjoules of FEL emission from the fourth harmonic of the

seed down to the thirteenth harmonic (20 *nm*) in the range specified for FEL1. Figure 5.2 highlights the transverse and longitudinal quality of the radiation at 20 *nm*. The FEL spot, imaged on a YAG screen placed at about 52.4 m downstream of the last undulator, is reproduced in figure 5.2a. The RMS transverse size is about 1.4 *mm* in both planes and this is in good agreement with expectations for a Gaussian beam with a beam waist at the exit of the last undulator of 200 μm consistent with the electron beam size at that point. Figure 5.2b shows a single-shot spectrum at 20 *nm*. The bandwidth (FWHM) is ≈0.009 nm and this gives a time-bandwidth product of about 0.56 that is ≈1.3 times the one for a Gaussian beam and this indicates the good longitudinal coherence of the FEL.

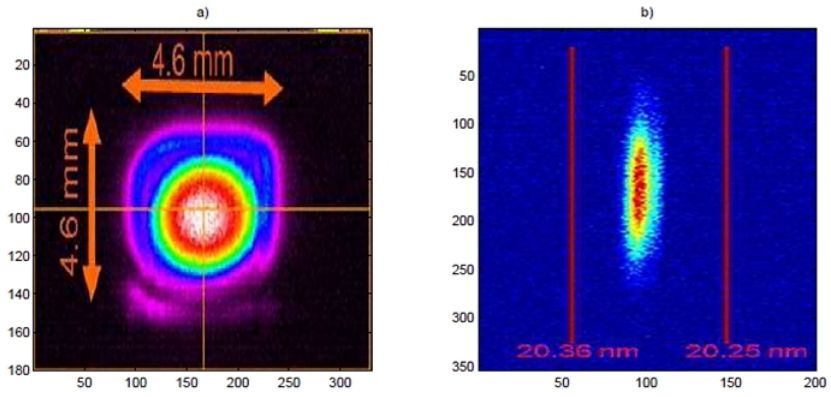

Figure 5.2: Transverse and spectral characterization of the radiation at 20 *nm*. a) Image of the radiation at 20 *nm* on a YAG screen placed at ≈ 52.4 m downstream of the radiator. b) Single-shot spectrum of the radiation at 20 *nm*. Courtesy of E. Allaria.

Clear evidence of coherent emission was observed at the fifteenth harmonic (17 *nm*) exceeding the harmonic conversion factor fixed for FEL1. This indicates a very bright electron beam. For each harmonic, the FEL has been optimized by tuning the amplitude of energy modulation produced in the modulator (controlling the seed power) and the strength of

the dispersive section. The optimization procedure generally leads to a setting with a R_{56} in the range between 40 and 70 μm. A complete characterization of the light produced at the eighth harmonic of the seed laser (32.5 nm) is reported in the following. We obtained similar results in the whole spectral range between 26 and 65 nm. After optimization of the FEL process to maximize the output energy from the whole radiator (6 sections) tuned at 32.5 nm, we measured the energy, with the photodiode and the layout shown in figure 3.10 [127], as a function of the number of sections contributing to the coherent emission. The FEL power has been estimated from the pulse energy, considering that the simulations predict for these conditions an FEL pulse of about 85 fs FWHM. Figure 5.3a shows the measured FEL power evolution along the FEL1 radiator, for both planar and helical undulator configurations. In the inset, the same data are reported on a logarithmic scale, clearly showing the different gain lengths associated with the two polarizations. Fitting the data with an exponential curve yields a gain length (defined in sections 1.2 and 2.4) of about 2.5 meters for planar polarization and 2.0 meters for circular polarization. This result is in good agreement with both the gain length calculated using the FEL parameter and the formula by Ming Xie [55] evaluated with the electron beam parameter reported in table 5.1. As expected, in the case of circular polarization, a shorter gain length and a higher output power is obtained due to better coupling between the electromagnetic field and the electrons, compared to the case of linear polarization. The measured FEL evolution is also in good agreement with the numerical simulation performed using the GINGER numerical code. Figure 4.1a reports the predicted output power obtained by simulations. The measurement of the gain length is not affected by the absolute calibration of the detector, as that of the pulse energy. So performing these measurements it is possible to validate,

with good precision, the expected brightness of the electron beam. The agreement of the actual FEL growth with the expected one allows even to state that the electrons-radiation coupling along the radiator is not much spoiled by an imperfect tuning of the undulator and by imperfections of the electron beam trajectory. It is worth noting that FERMI FEL achieved a power close to the level of SASE saturation with a radiator that is about 6-8 gain lengths, while for a SASE FEL generally about 20 gain lengths are needed. The SASE process (sections 1.2 and 2.4) starts from a very low bunching (0.01%-0.05%) while typically in HGHG scheme a bunching of a few per cent (1%-5%), produced in the dispersive section, drives the growth of FEL radiation in the radiator. Then SASE process needs a longer undulator to reach the same power level compared to HGHG.

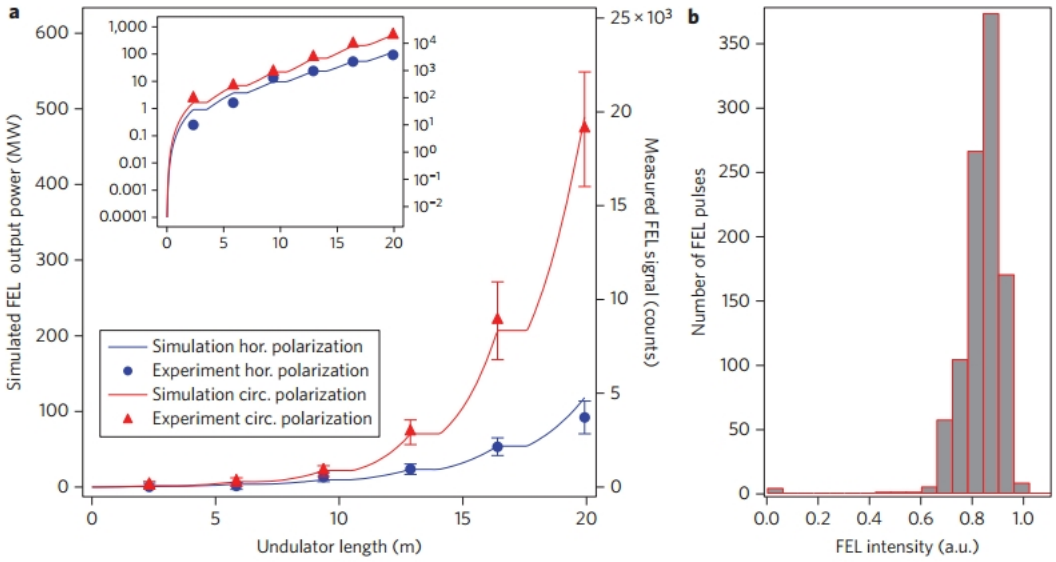

Figure 5.3: Measured FEL intensity at 32.5 *nm*. a: Measured FEL energy per pulse (symbols, right axis) as a function of the number of undulator sections used in the radiator, and predicted FEL power from numerical simulations [37] (lines, left axis). Data are shown for both circular (red symbols) and horizontal (blue symbols) polarization of the radiator sections. Error bars reflect the statistical distribution of results obtained from several consecutive pulses. In the inset, the same data are reported in a logarithmic scale. b: Typical shot-to-shot distribution of the pulse energy per for 500 consecutive FEL pulses. The quasi-Gaussian distribution characterized by a standard deviation of about 10% reflects shot-to-shot fluctuations in the electron-beam parameters. Taken from [13].

Moreover as shown in figure 4.1b, the measured FEL energy fluctuations are of the order of 10%, following an approximately Gaussian distribution. These results show how the use of an external seed allows us to keep the power fluctuations under control, without the need to enter deeply into the saturation regime, as is necessary in the case of SASE. Since it has been predicted that some of the desirable FEL properties, such as transverse and longitudinal coherence, can be degraded when a SASE FEL is operated in the saturation regime SASE FELs may require operation under conditions that strike a compromise

between maximum output power, reduced fluctuations and high coherence. This compromise has been demonstrated to be less critical for FERMI where these properties can be controlled simultaneously. It is also important to point out the different origins of power fluctuations in SASE and HGHG FELs. The HGHG process is deterministic with power fluctuations deriving from shot-to-shot fluctuations in the electron-beam and seed parameters. In principle, in the HGHG process reproducibility can be improved at will, the limit being only technological. The SASE process is, instead, inherently stochastic, so that the statistical distribution of the FEL pulse parameters can only be modified by acting on the exponential or saturated operating regime [169]. Due to the fact that the seed laser imprints its coherence properties onto the electron beam, the FEL radiation produced by the HGHG is expected to have a very good transverse coherence at the very beginning of the process. Figure 5.4a,b shows the measured transverse FEL profiles of the FERMI FEL operating at 32.5 nm in horizontal polarization. Data analysis shows that the FEL pulses are very close to a diffraction limited Gaussian beam. The FEL spot size measured on the two screens is in good agreement with expectations for a Gaussian beam with a beam waist at the exit of the last undulator of 200 μm consistent with the electron beam size at that point. Moreover, very good transverse coherence is also confirmed by results of a Young's double slits experiment shown in figure 4.2c. A preliminary analysis indicates that more than 90% of the diffraction pattern intensity is maintained at a slit separation of 0.8 mm.

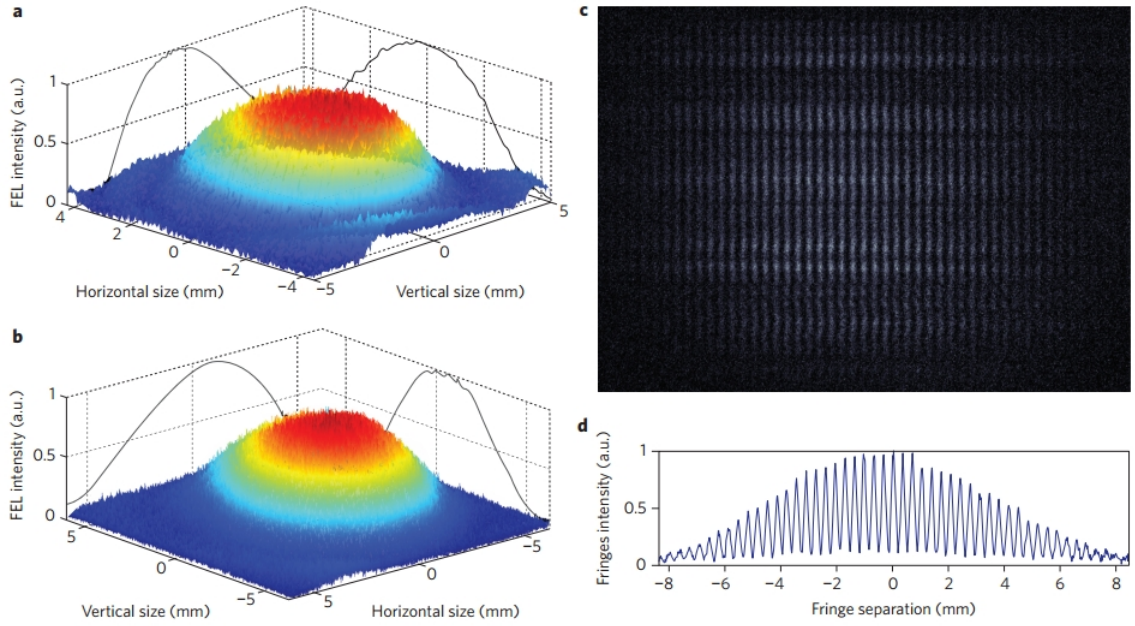

Figure 5.4: a: FEL spot size measured on a YAG screen positioned 52.4 m downstream from the radiator exit. The main signal is well reproduced by a Gaussian profile and is characterized by a second moment of about 2 *mm* in both the vertical and horizontal directions. b: FEL spot size measured on a second YAG screen positioned 72.5 m downstream from the radiator exit. In this case the measured horizontal and vertical beam dimensions are 2.6 *mm* and 2.4 *mm*, respectively. c, d: Image and projection of the interference pattern recorded on the second YAG screen when the FEL beam propagates through two 20 μm slits, separated by 0.8 *mm*, placed about 8.5 meters before the screen. Taken from [13].

One of the most attractive features of seeded FELs, including those employing HGHG, is the possibility of obtaining highly-stable output spectra. The spectral properties of the pulses produced by an HGHG FEL are strongly related to the spectral properties of the seed laser. The results obtained at FERMI are shown in Figure 5.5, where both a single-shot spectrum (figure 5.5a) and a sequence of 500 consecutive single-shot spectra (figure 5.5b) are reported. Figure 5.5a also shows the measured spectrum of the seed laser pulse. For both pulses the spectra are displayed in meV around the central photon-energy, i.e., 4.8 eV (260 nm) for the

seed and 38.5 eV (32.5 nm) for the FEL. The measured FEL bandwidth is 20 meV (RMS), yielding a relative bandwidth of about $5{\cdot}10^{-4}$. This number should be compared with the FEL ρ parameter (see table 5.1), which approximately corresponds to the expected bandwidth of SASE emission in the same experimental conditions. Experimentally, the relative spectral bandwidth measured at FERMI is about an order of magnitude smaller than that observed at SASE FELs operating in the VUV and soft X-ray regime [169, 10]. Figure 5.5a shows that the FEL bandwidth in eV is larger than that of the seed laser. However, we believe that this increase is not associated with a degradation of the longitudinal coherence of the FEL pulse, but rather with a natural shortening of the FEL pulse duration relative to the seed pulse; this effect has been theoretically predicted [170] and also seen in numerical simulations for our conditions. We obtain, for the FEL pulse, a time-bandwidth product (equation 1.3) of 0.53 considering a time duration of 85 fs. This is about 1.2 times the value of time-bandwidth product of a Gaussian beam and this is an indication of a good longitudinal coherence.

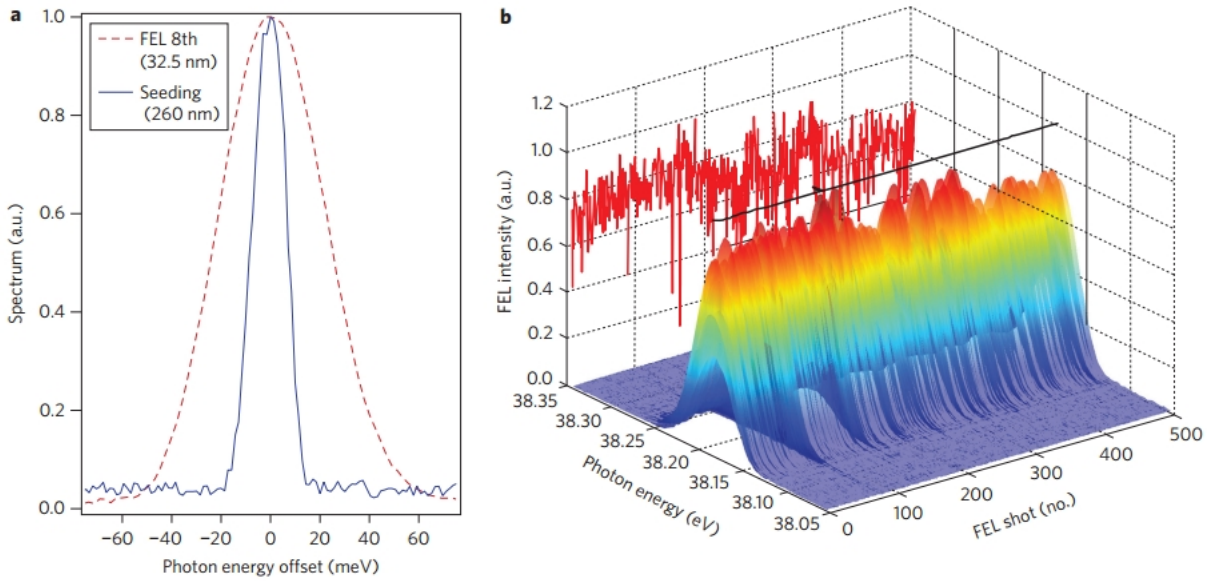

Figure 5.5: Single-shot and multi-shot spectra at 32.5 *nm*. a: Measured FEL and seed laser spectrum (dashed red and continuous blue lines respectively). b: Acquisition of five hundreds consecutive FEL spectra. Taken from [13].

Another very important property of light sources to be used for energy-resolved experiments is the wavelength (or photon-energy) stability. The FERMI measurements shown in figure 5.5b indicate that the normalized photon-energy stability is of the order of $7.5{\cdot}10^{-5}$, a noticeable improvement when compared to previous SASE FEL results obtained in the same photon-energy range [10, 169, 171].

In this beam configuration it is possible to determine which part of the electron beam is producing the FEL light using the screen in the main beam dump located after the undulator. The longitudinal beam coordinate is mapped, in the presence of a linear energy chirp, on the abscissa on the screen. Figure 5.6 shows, on the bottom, the image of the electron beam on the beam dump screen (figure 3.9) with the seed laser switched off. The

abscissa is the beam energy as the screen is in a location in which the dispersion created by the dipole is >1m. The beam has a chirp and the tail has energy higher than the head. The head and the tail of the beam fall in different parts of the screen. The y coordinate of the beam is imaged on the ordinate of the screen. The horizontal profile of the screen image, shown on the top of figure 5.6, reproduces the longitudinal profile of the beam. Here the y coordinate is the total image intensity at fixed x and is proportional to the beam charge density.

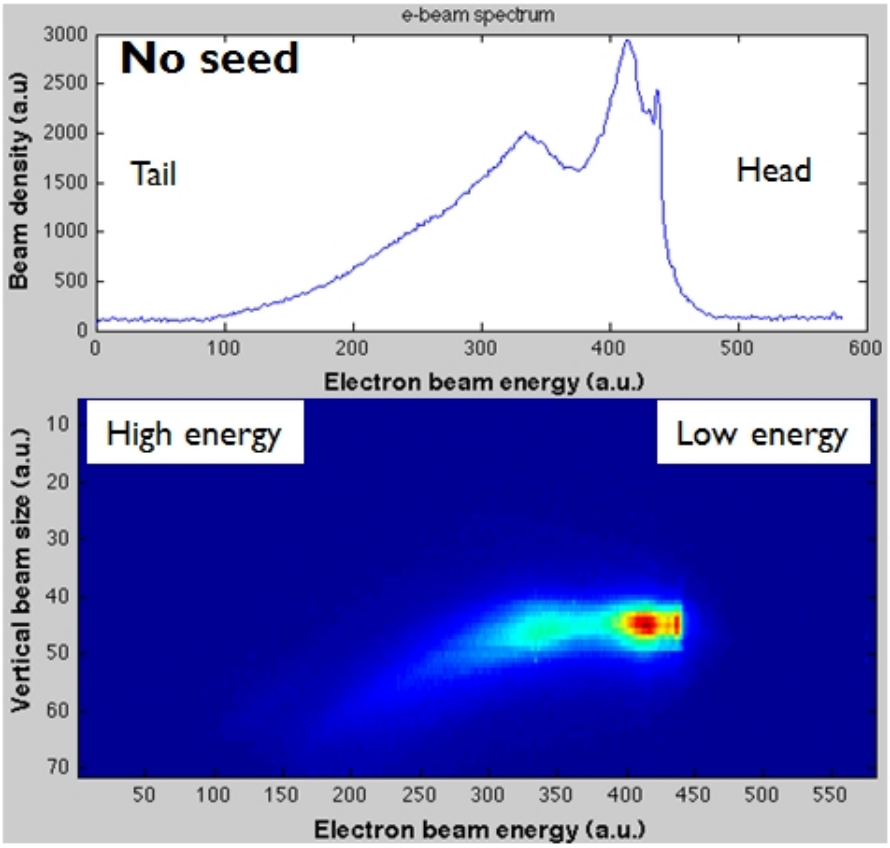

Figure 5.6: Beam energy spectrum reconstructed using the main beam dump dipole (up). Beam image on the main beam dump screen (down).

We obtain a current profile shape close to that shown in figure 4.7 with a peak on the head and a ramped shape. Part of the electron beam is heated when the laser beam interacts with the electron beam in the modulator. The portion of the electron beam, in which the FEL light is produced, is visible as a "hole" in the energy spectrum on the main beam dump screen. Figure 5.7 shows the energy spectrum for three positions of the delay line. From the left to the right we see the interaction region moving from the head to the tail of the beam. The beam energy spectra identified by the star, the square and the diamond are obtained at delays of the seed laser, referring to the figure 5.1, of -0.2 -0.1 and 0.5 *ps* respectively.

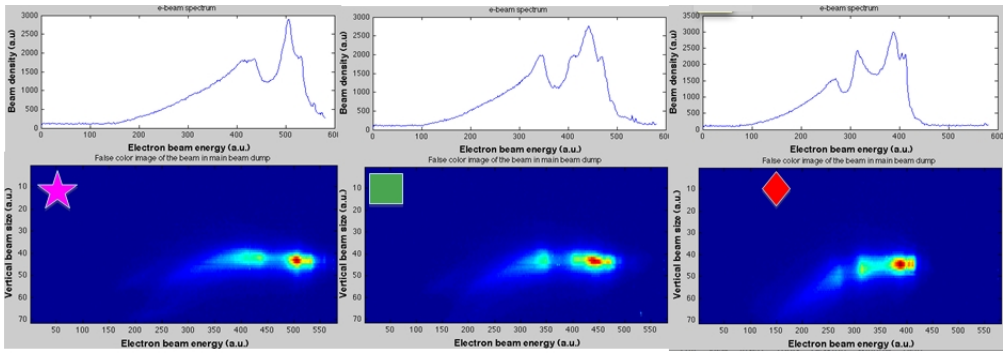

Figure 5.7: Beam energy spectra for three different delays of the seed.

We measure the FEL pulse energy while moving the delay and recording the corresponding horizontal coordinate of the interaction region on the screen. In this way it is possible to see the optimum beam region for the FEL process. Figure 5.8 shows the FEL energy vs the position of the interaction region on the screen. The identifiers of the three subplots of figure 5.7 are reported on the figure 5.8.

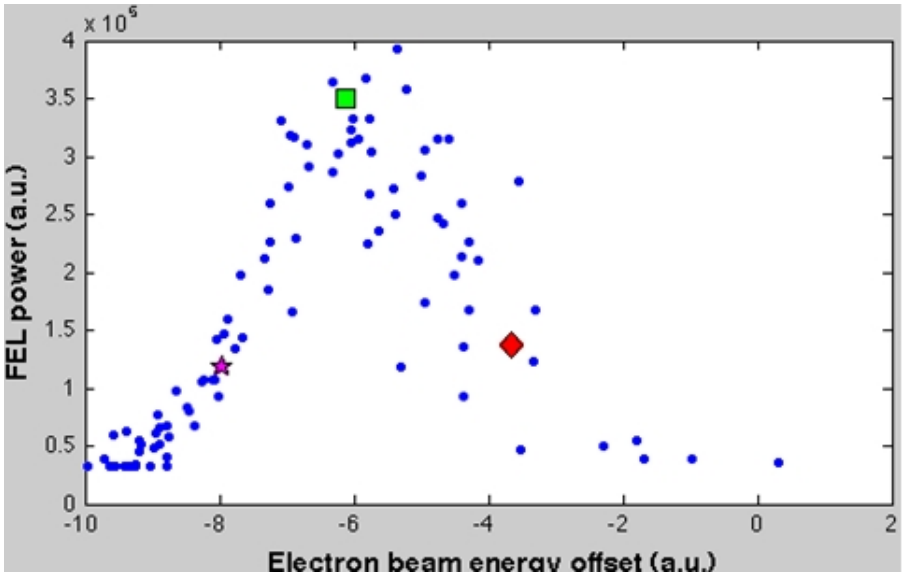

Figure 5.8: FEL power vs position of the hole observed in the beam energy spectrum.

From figure 5.7 and 5.8 we can see that the part of the electron beam in which the FEL radiation production is more effective is located before the current peak. The higher current peak created by compressing the beam without the X-band cavity and the laser heater is not useful for the FEL as the beam quality at this point is lower. This is even more evident when increasing the beam charge and the beam compression factor. Figure 5.9 shows the spectrum as a function of the position of the FEL on the electron beam for a beam charge of 500 pC and a compression factor of about 5.6.

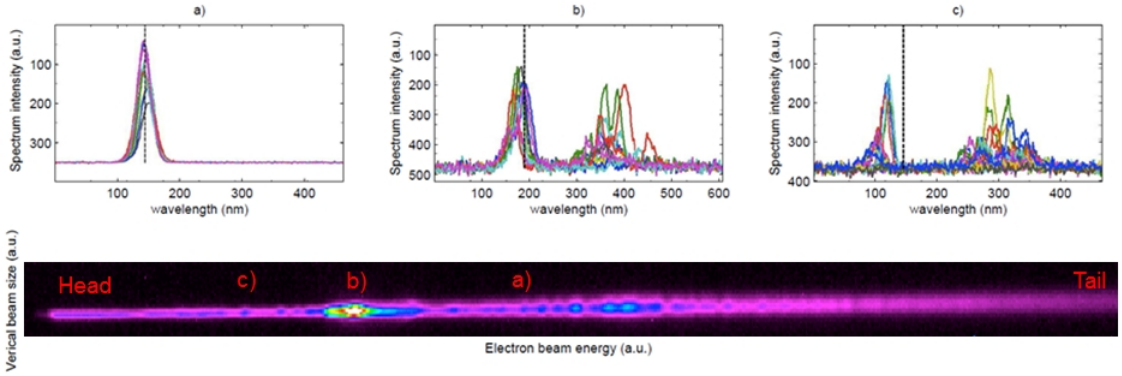

Figure 5.9: FEL power vs. position of the hole observed in the beam energy spectrum. The subplots a, b and c indicate the three series of ten single-shot spectra each collected as the FEL is produced in the three regions of the electron beam identified by the corresponding letters on the electron beam spectrum. Courtesy of E. Allaria.

We can see that the FEL radiation produced by the peak is characterized by a noisy and spiky spectrum as the phase space in this region is spoiled by the microbunching. Then it is necessary to use the X-band cavity and the laser heater in order to preserve the beam phase space quality while compressing the beam, as seen in the previous chapter, and in this way it is possible to improve the FEL performance as we will see in the next section.

5.3 Mild compression scenario

The availability of the X-band cavity and the laser heater has permitted the use of a higher beam current, while preserving beam quality and phase space properties on a good portion of the electron beam as seen in the sections 4.3 and 4.6. This has permitted to increase the FEL pulse energy by a factor ≈10-15 on the whole spectral range covered by FEL1. We report a long sequence of FEL pulse energy measurements with the ionization gas monitor

at 52 *nm* (fifth harmonic of the seed wavelength of 260 *nm*) and 26 *nm* (tenth harmonic).

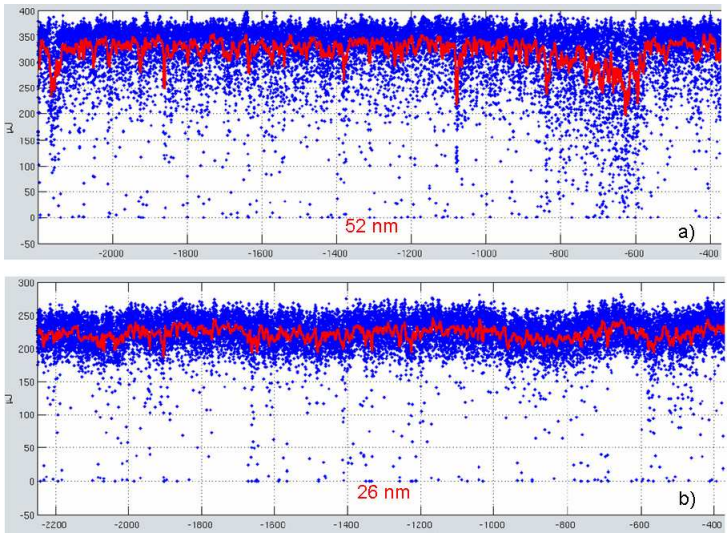

Figure 5.10: Gas ionization monitor measurements of FEL pulse energy at 52 *nm* and 26 *nm*.

The mean pulse energy is about 350 μJ at 52 *nm* and 220 at 26 *nm*. The pulse stability is around 15-20%. In this beam condition (500 pC , CF=10, X-band and laser heater on) a pulse energy of ≈100 μJ, with a stability of 15-20% was obtained at 20 *nm* (thirteenth harmonic). The use of the X-band cavity and laser heater, as seen in section 4.6 allows the beam current to be increased without spoiling the beam quality and phase space linearity. In this condition it is possible to increase the FEL pulse energy without affecting the spectral purity. We report a series of 400 spectra at 35.4 *nm* (seventh harmonic of the seed wavelength of 248 *nm*) in figure 5.6.

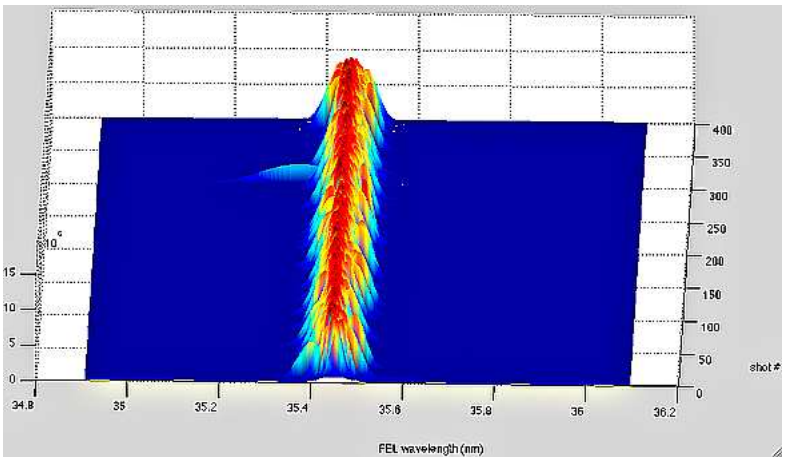

Figure 5.11: Single-shot spectra at 35.4 *nm*.

The mean RMS bandwidth is $0.022 \pm 0.006\,nm$. The central wavelength is $35.45 \pm 0.016\,nm$. The relative bandwidth is $6.5 \cdot 10^{-4}$ and the central frequency jitter is in the bandwidth.

5.4 Laser Heater and FEL1 performance

The capability to increase the beam current while preserving the low energy spread and the regularity of the phase space allows the FEL flux to be increased while preserving the spectral purity and stability as seen in the previous section. Beneficial effects of the laser heater have been observed on both FEL pulse energy and spectrum for several configurations of the FERMI linac and at different harmonics of the seed laser. The FEL pulse energy at 24.3 *nm* (10th harmonic of the seed produced by an optical parametric amplifier tuned at 243 *nm*) measured on a downstream gas cell vs. the seed laser energy is shown in figure 5.12 for three different settings of the laser heater.

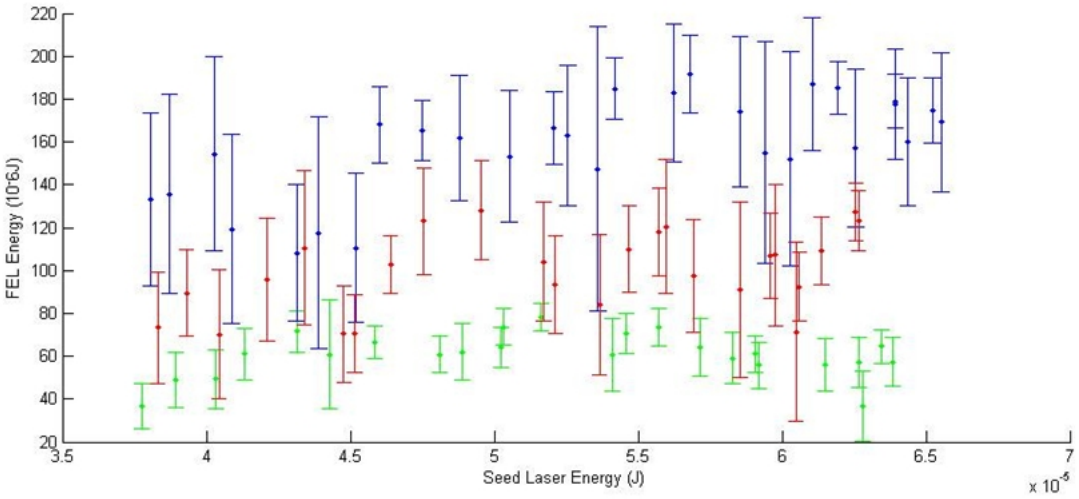

Figure 5.12: FEL energy vs. seed energy for several laser heater settings.

The green points are taken when the laser heater is switched off, the red points refer to a beam heating of 14 keV while the measurements shown by the blue points are taken for a beam heating of 7 keV for which the maximum FEL pulse energy is obtained. The data are obtained with a 500 pC electron beam compressed by a factor close to 10 in BC1. The error bars comes from the statistical fluctuations on 30 shots. The X-band cavity is on to produce a linearized compression. The maximum energy obtained when the laser is set properly is almost 3 times the energy available when the laser heater is switched off. This confirms that the laser heater increases the electron beam quality and it suggests that a reduction of the slice energy spread is induced by a proper amount of beam heating, as predicted by theory and simulation [99, 100]. The laser heater is also responsible for cleaning of the FEL spectrum at any harmonics of the seed laser. The level of cleaning of the spectrum induced by the laser heater depends critically on the microbunching afflicting the beam when the heater is off. Now we show some data taken in condition of particularly strong

microbunching. Figure 5.13 shows 100 spectra taken with the laser heater switched on (on the top) and 100 spectra taken with the laser heater off (on the bottom). The black lines in the two plots are the two mean spectra. The electron beam used has a charge of 500 pC and the compression factor is around 10. The radiator is tuned on the 8th harmonic of the seed laser.

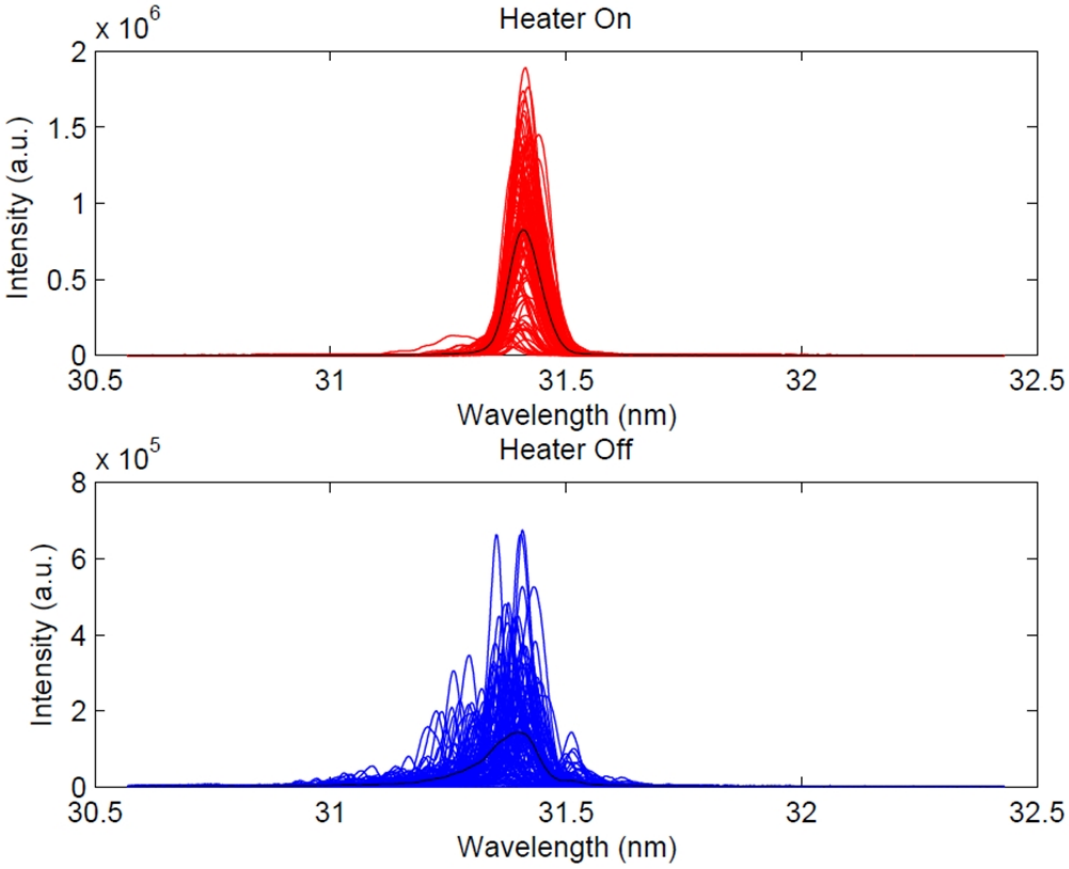

Figure 5.13: FEL output spectra at the 8th harmonic of the external seed laser. Top panel: heating on; bottom panel: heating off.

The FEL spectrum has a spiky aspect with multiple peaks when the laser heater is switched off. The spectrum appears to be more clean with a Gaussian-like shape and the central

wavelength is more stable when the laser heater is switched on. The mean bandwidth varies, in this set of data, from 0.052 nm to 0.029 *nm*, while the stability of the central frequency goes from 0.055 *nm* to 0.015 *nm* when the laser heater is switched on. The effect of the laser heater on the FEL spectrum is evident also at higher harmonics. Figure 5.14 shows 60 spectra taken with the laser heater switched on (on the top) and 60 spectra taken with the laser heater off (on the bottom). The black lines in the two plot are the two mean spectrum. The electron beam used has a charge of 500 *pC* and the compression factor is around 10. The radiator is tuned on the tenth harmonic of the seed laser.

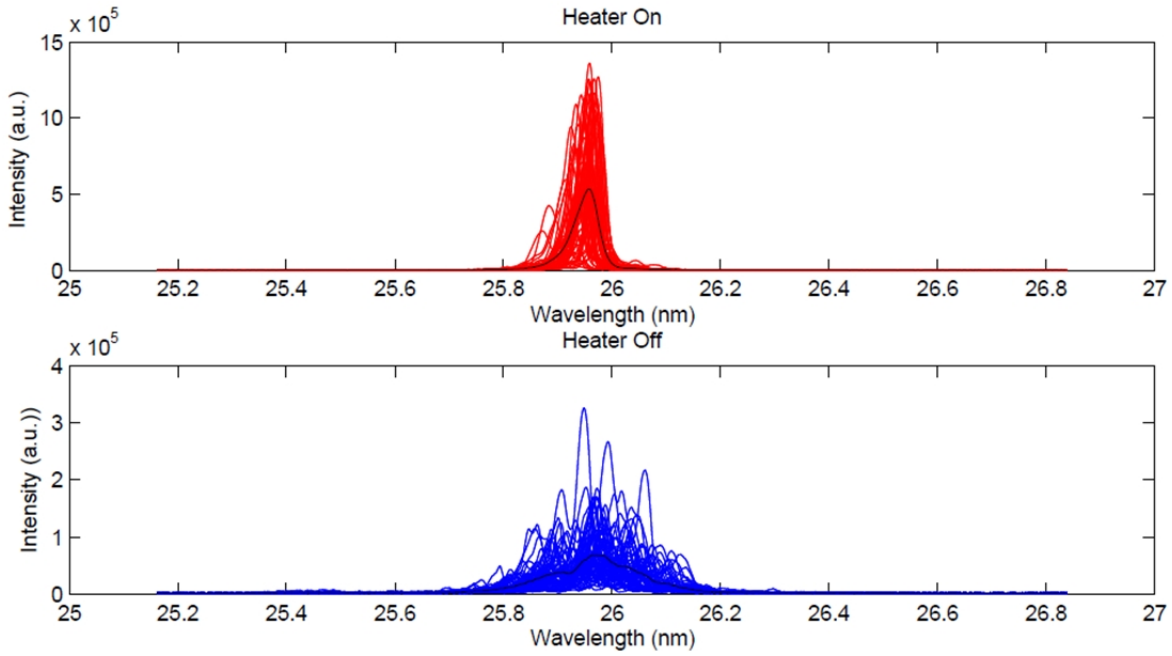

Figure 5.14: FEL output spectra at the 10th harmonic of the external seed laser. Top panel: heating on; bottom panel: heating off.

In this case the mean bandwidth varies from 0.063 *nm* to 0.015 *nm* while the stability of the central frequency goes from 0.035 *nm* to 0.015 *nm* when the laser heater is switched

on. The transverse RMS dimension of the laser pulse in the laser heater undulator used is around 130 μm for these measurements.

5.5 Extremely high harmonics

It is possible to tune the radiators of FEL1 with the resonance to shorter wavelengths, beyond the nominal interval of operation. As expected a pulse energy decreasing with the harmonic number is obtained, but the radiation spot on the diagnostic CCD can be detected at surprisingly high orders, as shown in section 5.15, up to the twenty-ninth harmonic (h29) corresponding to a wavelength of about 9 nm.

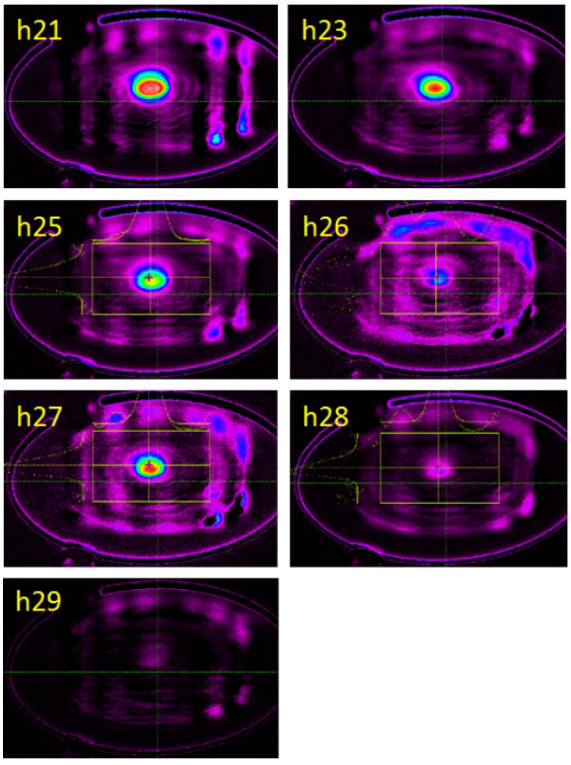

Figure 5.15: Spot of the FEL mode at higher harmonic orders.

In figure 5.16 the spectrum for twenty-sixth harmonic is shown. The spectrum is acquired by integrating for 5 seconds, corresponding to a sequence of fifty laser shots.

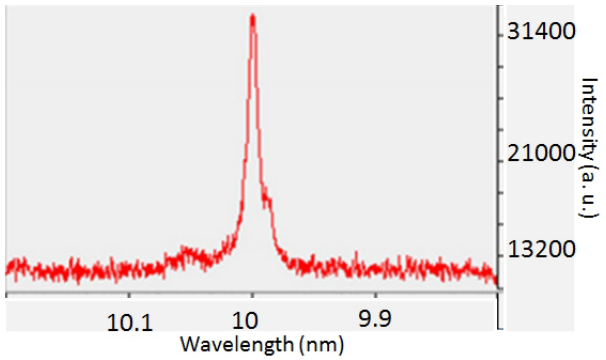

Figure 5.16: Spectrum of FEL1 tuned at 10 *nm*.

No signal was observed at harmonics higher than the twenty-ninth with the single stage cascade FEL1 figure 5.15. However the undulator of FEL1 may be configured as a double stage cascade following, in the radiator, a layout similar to those used in [172, 173] and represented in figure 5.17. In this configuration the first undulators of the radiator are tuned to one harmonic of the seed, as in the nominal configuration of FEL1, and the last undulators are tuned to one harmonic of the previous ones. The FEL growth, in the last stage, starts directly from one harmonic of the bunching produced in the previous radiator. In the case shown in figure 5.17 we tuned the first four undulators of the radiator to the thirteenth harmonic of the seed and the last two to the second harmonic of the previous one (twenty-sixth harmonic of the seed).

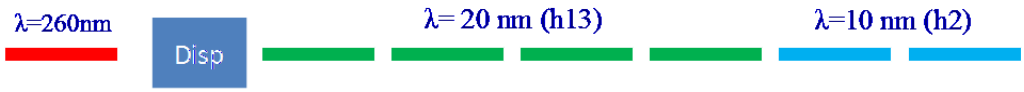

Figure 5.17: FEL1 in double stage cascade configuration. In this configuration the first undulators of the radiator are tuned to one harmonic of the seed, as in the nominal configuration of FEL1, and the last undulators are tuned to one harmonic of the previous ones. In the example shown the first undulators of the radiator are tuned to the thirteenth harmonic of the seed and the last undulators are tuned to the second harmonic of the previous ones. Courtesy of L. Giannessi.

The stronger amplification of a lower order harmonic in the first undulator part, leads to a stronger bunching and emission in the second part. This configuration tuned to reach the same final wavelength of 10 *nm*, was tested in the same e-beam condition of those used to measure the spectrum in figure 5.16. The relevant spectrum is shown in figure 5.18.

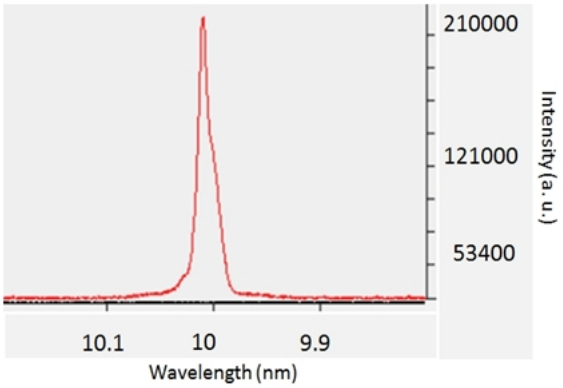

Figure 5.18: Spectrum of FEL1 configured as a double stage cascade as shown in figure 5.17.

Despite the fact that the spectrometer was not calibrated in energy, the acquisition in the two cases of the figures 5.16 and 5.18, is done in the same conditions. We can therefore compare the counts on the vertical scale in the two cases, and observe that the intensity

in the double stage cascade was about seven times higher than that relevant to the single stage. The same double stage cascade can be used to get wavelengths shorter than the one corresponding to the twenty-ninth harmonic of the seed. The spectrum at 6.67 *nm*, obtained in the configuration in figure 5.17 by tuning the last two modules at the third harmonic of the previous one, is shown in figure 5.19.

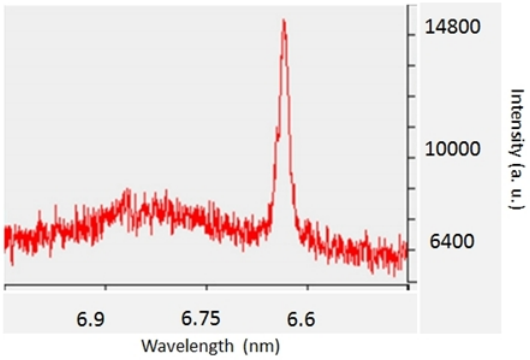

Figure 5.19: Average of 50 spectrum collected with the first four radiators tuned to the thirteenth harmonic of the seed and the last three tuned to the thirty-ninth harmonic of the seed.

We then configured the undulator like an harmonic cascade of the type studied in [174]. In this configuration the last radiators are not tuned to a harmonic of the first ones, but have a common higher order harmonic. In the specific case, still maintaining the radiators 1-4 (green in figure 5.20) with the resonance at 20 *nm*, we have tuned the last two radiators to 8 *nm*. The two sets of undulators have a resonance in common at one of their higher harmonics, at about 4 *nm*. This is the fifth harmonic of the first four undulators and the second harmonic of the last two. This configuration is shown in figure 5.20.

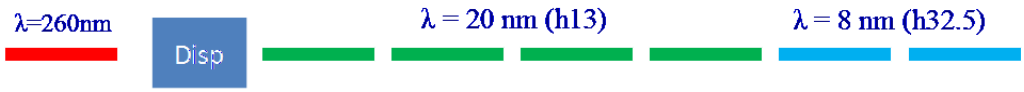

Figure 5.20: FEL1 in a harmonic double stage cascade configuration. The first four undulators are tuned at 20 *nm* and the last two undulator are tuned to 8 *nm*. The fifth harmonic of the first stage is tuned to the second harmonic of the last two undulators. Courtesy of L. Giannessi.

The spectrum obtained in this configuration is shown in figure 5.21.

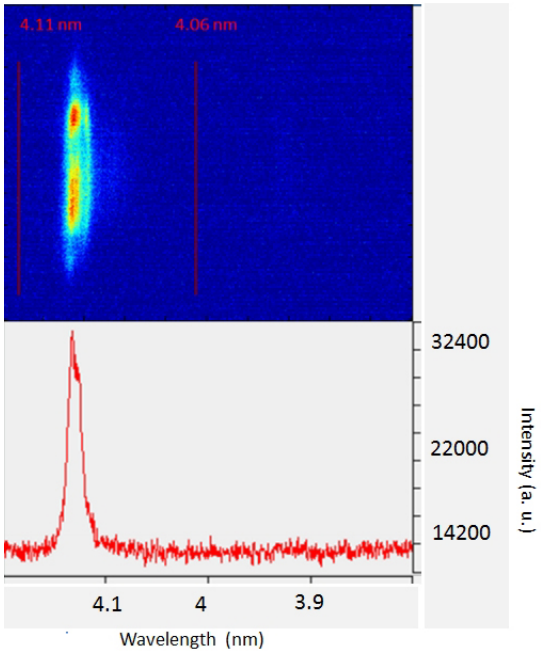

Figure 5.21: Spectrum of FEL1 in a harmonic double stage cascade configuration.

The upper image represents the spectrometer CCD raw data. The vertical axis is not dispersed in frequency and provides information about the vertical intensity distribution at the spectrometer. The double lobe structure of the y trace is typical of the even harmonic emitted off-axis in a circularly polarized undulator.

Chapter 6

Self-seeding

In the previous chapter we have seen that seeded FELs based on the HGHG scheme can provide powerful, nearly Fourier transform limited, radiation pulses from the VUV down to the soft X-ray regime. The highest harmonic of the seed laser wavelength, 260 *nm*, obtained at FERMI is the 65th, i.e. 4 *nm*. Pushing the harmonic number further to reach hard X-ray regime seems, at the moment, difficult. A powerful and reliable seed source at short wavelengths $\approx$10 *nm*, is not available at the moment. For this reason other mechanisms, alternative to external seeding, to obtain coherent pulses in the hard X-ray region have to be found. Due to the absence of a short wavelength seed laser it seems reasonable to start from SASE. In this chapter we describe the so-called self-seeding technique and we present the first hard X-ray self -seeding experiment done at LCLS with relative simulations.

6.1 SELF-SEEDING

The SASE configuration works by amplifying shot noise and for this reason it is considered the natural option to produce short and powerful radiation pulses in the soft and X-ray region where laser source for external seeding are not available. LCLS, SACLA and FLASH, the three SASE FELs working in the VUV and X-ray regime, have demonstrated at least ten orders of magnitude of increase in brightness with respect to the third generation of light sources delivering sub-picosecond pulses. The operations of these machines have confirmed the poor longitudinal coherence and intrinsic wide bandwidth of SASE FELs. A straightforward scheme, called self-seeding, to improve the longitudinal coherence of SASE has been proposed in [76]. Self-seeding consists of two long undulators separated by an electron beam chicane in which a monochromator is installed. The first undulator works in SASE configuration without an external seeding. The radiation produced in the first undulator is purified by the monochromator and then used as coherent seed for the second undulator. The monochromator can produce a delay of the light with respect to the straight line and the electron path in the chicane has to be adjusted to provide synchronization between the two beams in the second undulator. The beam coming from the first SASE undulator has a density modulation with a broad spectrum content resulting from the shot noise amplification within the FEL bandwidth in the first undulator. The presence of energy and density modulation in the FEL bandwidth can spoil the longitudinal coherence and spectral quality of the light amplified in the second undulator. The R_{56} of the chicane and the energy spread of the electron beam washes out the microbunching produced in the first undulator.

The first article about self-seeding presented an application of the technique at 6 *nm* wavelength and was devoted to soft X-ray regime. In this spectral range, the type of monochro-

mator used to purify SASE can be based on a grating. The time delay of the light with respect to the electrons depends on the number of mirrors and on the geometry used and is in the range 800 *fs*-5 *ps*. A conventional 4-crystals monochromator can be used to extend the self-seeding technique to the hard X-ray regime but the time delay of the light cannot be shorter than 10 *ps*. This delay requires, in the single bunch configuration, a long chicane in which the light produced by one bunch in the first monochromator is amplified by the same bunch in the second undulator. Such a chicane can degrade the electron beam quality through incoherent and coherent synchrotron radiation. Recently a straightforward technique to achieve self-seeding in the hard X-ray regime with a single bunch has been proposed [175] and successfully demonstrated in LCLS [76]. This technique uses a single crystal in forward Bragg diffraction (FBD) [176] geometry on which the SASE pulse produced in the first undulator impinges. The layout of this scheme is shown in figure 6.1.

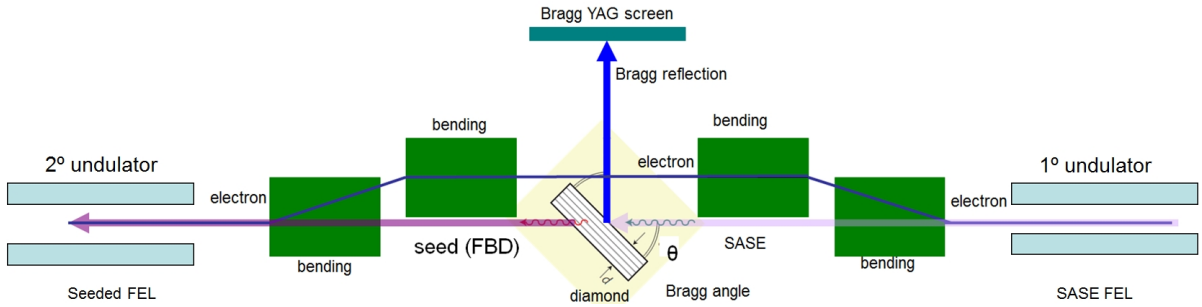

Figure 6.1: Scheme of the hard X-ray self-seeding based on the crystal monochromator. The first undulator is separated from the second one by a chicane for the electron beam. A crystal, placed in Bragg geometry in the chicane, intercepts the SASE (pale magenta beam) radiation produced in the first undulator. Part of the radiation component satisfying the Bragg condition is reflected (blue beam). The rest of the radiation satisfying the Bragg radiation, that is not reflected, is transmitted with a delay with respect to the SASE components that not satisfies the Bragg condition. The position of the reflected radiation on the screen, shown in the picture, identifies the angle θ.

The angle between the crystal and the SASE propagation direction is chosen to satisfy the Bragg condition for one component of the SASE spectrum. This component experiences multiple scattering in the crystal and it is partially reflected. The spectrum of the reflectance exhibits a narrow line width and the transmission spectrum exhibits an absorption resonance. The crystal acts like a band pass filter. The Bragg angle satisfies the condition [177]:

$$2d_s sin\theta = \lambda_r \tag{6.1}$$

where d_s is the spacing between crystallographic planes, θ is the angle between the crystal and impinging radiation and λ_r is the wavelength that experiences Bragg reflection. The forward scattered radiation acquires a phase shift required by causality and that can be calculated by the Kramer Kronig [178-180] relation from the transmittance spectrum. This shift produces a delay in the time domain. The rest of the SASE spectrum that does not satisfy the Bragg condition is transmitted without delay and is followed by a monochromatic wake formed by the component identified by the Bragg condition. The time duration of the wake is inversely proportional to the bandwidth of the absorption line. The wake exhibits multiple peaks of decreasing intensity for increasing time delay. The delay at which the maxima are located and the duration of bumps depends on the crystal structure. The properties and underlying physics of FBD relevant to this application are discussed in detail in [176]. Here, we only highlight that the time dependence t of the radiation envelope of FBD, G00(t), which represents the crystal response to a very short incident pulse, can be

parameterized with the characteristic timescale T_0:

$$|G_{00}(t)|^2 \propto \left[\frac{1}{T_0}\frac{J_1\left(\sqrt{\frac{t}{T_0}}\right)}{\sqrt{\frac{t}{T_0}}}\right]^2 \tag{6.2}$$

with $T_0 = \frac{\Lambda^2 sin\theta}{2\pi^2 cd}$ were Λ is the extinction depth [177] and d is the crystal thickness. The delay of the first maximum is of the order of 10-20 *fs* and then a very gentle chicane is enough to delay the electron beam to establish the seed amplification in the second undulator. This chicane provides the room for the crystal and is useful to wash out the microbunching produced in the SASE radiator. For the single crystal wake monochromator, the ratio between the peak power in the first bump and the SASE power can be related to the pulse duration of the SASE pulse, the SASE coherence length and the location of the first maximum:

$$\frac{P_{seed}^{max}}{P_{SASE}} = \frac{L_{SASE}L_{coherence}}{c\tau_1^2} \tag{6.3}$$

This scheme has been successfully demonstrated in LCLS in the first self-seeding experiment.

6.2 LCLS experiment: results

Here, we describe some initial results from the HXRSS experiment at LCLS. The LCLS nominally operates at 150–250 pC of charge in a single electron bunch at a repetition rate

of 120 *Hz*. However, the machine can also be run in a low-charge mode [140] where only 20–40 pC of charge is used to generate a much shorter pulse length of 5–10 *fs*, but with proportionally fewer photons ($0.2 \cdot 10^{12}$ photons per pulse at 8 keV). This short pulse provides good overlap with the short seed wake pulse produced by the diamond monochromator and is used for the self-seeded mode of operation. As described above, the low-charge SASE mode of operation produces very limited longitudinal coherence and a broad, noisy photon spectrum with a relative spread of 0.25% full-width at half-maximum (FWHM; 20 eV). The self-seeded mode is designed to dramatically improve the bandwidth and coherence. The self-seeded mode is established by inserting the diamond crystal in the SASE X-ray beam path to generate the monochromatic seed pulse and using the chicane to delay the electrons by 20 *fs* to overlap the seed. The Bragg angle of the diamond crystal is chosen for the desired seeding wavelength. By adjusting the electron energy, the SASE spectrum produced by the first undulator stage should fully cover this seeding wavelength. An angle θ=56.538 (see figure 6.1) corresponds to the Bragg reflection condition from the (004) atomic planes of diamond for 8.3 keV photons near the K-edge of nickel. The energy of the electron beam is adjusted to 13.71 GeV to be resonant with the seed. The extinction depth for the 004 reflection of our crystal is $\Lambda = 22.6\mu m$, so that we obtain from equation 6.2 $t_s = 19\,fs$ for the location of the first maximum of the monochromatic field with respect to the incident pulse. The crystal time response $\propto |G_{00}|^2$ equation 6.2 is plotted in figure 6.2.

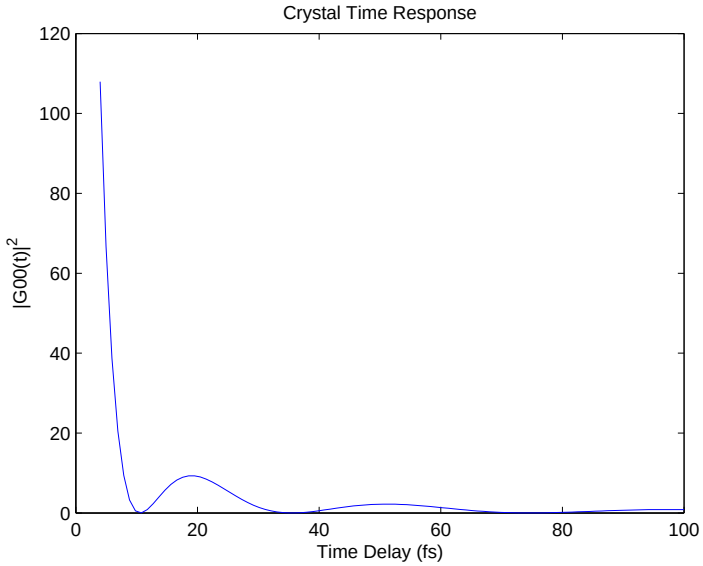

Figure 6.2: Time responses $|G_{00}|^2$ to excitation with a short X-ray pulse in FBD. Reflection from the atomic planes (004) of diamond. Results for diamond crystals with thickness d=0.1 *mm*.

The unfiltered SASE pulse is superimposed on the monochromatic wake in the first 10 *fs* of the time scale in figure 6.2. The first monochromatic bump, useful for self-seeding, has a time duration of ≈*15-20 fs*. The transverse overlap between the seed and the electron beam can be optimized by slightly varying the electron position and angle using the undulator girder position remote control at the beginning of the second undulator stage.

The peak power available in the monochromatic seed can be estimated by equation 6.3. The coherence length is around 60 *nm* and the pulse length is around 5 *fs* and, with these parameters the maximum power of the first bump is 0.25% of the SASE power. We calculate the evolution of the FEL pulse along the SASE undulator using the equation 2.45 for the high-gain regime replacing L_G with L_{1d} (equation 2.50). From the previous considerations and calculations we find that the peak seed power at the end of the fifteenth undulator is:

$$P_{seed} \approx \frac{0.0025\cdot}{9} exp(\frac{14 \cdot L_U}{L_G}) \cdot P(0) \approx \frac{0.0025\cdot}{9} exp(12) \cdot P_{noise} \approx 35 \cdot P_{noise} \tag{6.4}$$

where the number of the undulators has been reduced, in equation 6.2, by one to take into account the lethargy and a mean gain length of 4 m has been considered [140]. The shot noise equivalent power is indicated as P_{noise} (2.64). Therefore the seed power generated in the first fifteen undulators easily overcomes the shot noise, ensuring the seed power requirements for the self-seeding experiments.

Although up to 15 undulator segments upstream of the seeding section (U1–U15) can be used to generate SASE, which is then 'filtered' by the diamond for seeding, too much SASE radiation actually induces a large growth of the electron energy spread, which then inhibits the gain process for the seeded FEL in the second stage. There is therefore a trade-off between seeding power and seeded FEL gain. Experimentally, we find that using only 13 SASE undulator segments (U3–U15) seems to produce the most seeded FEL power at the end of the LCLS undulator line. The typical SASE pulse energy produced by 13 undulator segments is 10 μJ with 40 pC of bunch charge. Another 13 undulator segments (U17–U29) downstream of the seeding section amplify the seeded signal. Figure 6.3 shows the gas detector signal (X-ray pulse calorimeter), located well after U29, when the chicane was operated in the self-seeding mode. The left side of this time plot was taken when the diamond crystal was retracted from the X-ray beam path, showing a 19μJ mean SASE background, while the right side was taken when the diamond crystal was inserted, showing a 53 μJ mean seeded FEL signal, including the 19 μJ SASE background. Because the seed power is generated from the random SASE process and fluctuates close to 100% before saturation and when a single longitudinal mode is selected, the output FEL energy fluctuates

nearly as much for this linear amplifier. In addition, electron energy jitter of 0.05% r.m.s also contributes significantly to the FEL intensity fluctuation. Peak seeded intensities in excess of *200* μJ have been observed at a bunch charge of 40, but, to date, the variations in shot-to-shot intensity remain larger than 50%.

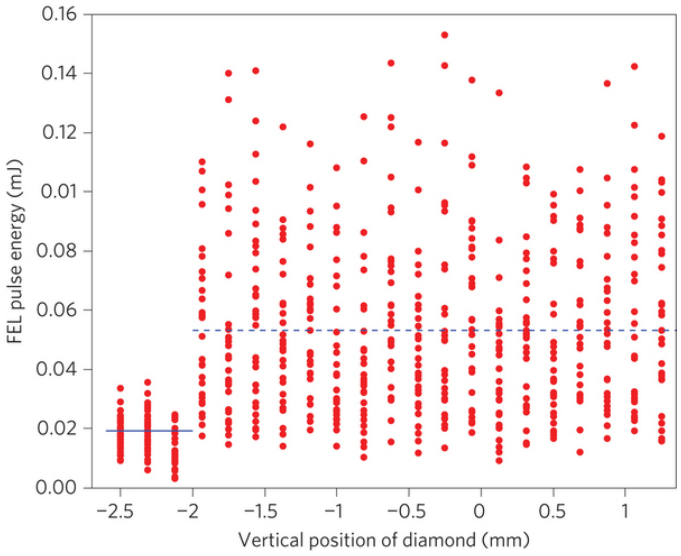

Figure 6.3: Each data point is an FEL X-ray pulse total energy measurement made using the gas detector and plotted against the vertical position of the diamond crystal (y). The X-ray beam falls off the crystal edge at y=-2 *mm*, showing the SASE background at y<-2 *mm* with a mean pulse energy of 19 μJ (solid blue line). The seeded signal (plus the SASE background) is shown at y>-2 *mm* with a mean energy of 53 μJ (dashed blue line) and peaks at 150 μJ. This does not show the best seeded performance but does reflect the large power fluctuations observed. The chicane is switched on here, which greatly reduces the SASE power from that of normal SASE operation. Taken from [77].

Figure 6.4a shows the single-shot SASE and self-seeded spectra recorded on a Si (333) bent crystal spectrometer [76] with an estimated resolution of 0.1 eV. The zero point in the horizontal axis refers to the mean photon-energy of 8331.5 eV (0.14881 *nm*). The SASE spectrum is produced with all 28 undulators, that is, with the chicane off and diamond

retracted. In this case, the optimized SASE pulse energy is 300 μJ with 20 eV FWHM bandwidth. The seeded signal reaches 240 μJ, and shows a single spectral spike of 0.4 eV (FWHM). The relative FWHM bandwidth is $5 \cdot 10^{-5}$ at 8.3 keV, which corresponds to a Fourier-transform-limited X-ray pulse of 5 fs (FWHM). Figure 6.4b shows the average SASE spectra for 20,000 shots taken on a Si (111) spectrometer, with a wider range to accommodate the electron energy jitter (on the order of 8–10 eV RMS). The FWHM of the average SASE bandwidth is 27 eV without energy jitter correction (as shown) and becomes 20 eV by correcting the electron energy on a shot-by-shot basis. It also shows the average seeded spectra over 200 shots taken on an Si(333) spectrometer under good seeding conditions. The FWHM bandwidth of the average seeded spectrum is 1 eV. The broadened average bandwidth comes from shot-to-shot spectral variations due to electron energy jitter and other factors. The seeded FEL has a Gaussian spatial mode with excellent transverse coherence. The simulations, as we will see in the next section, indicate that the seeded FEL spectra are quite sensitive to the detailed longitudinal phase space distribution of the electron beam and suggest further improvements in the seeding performance.

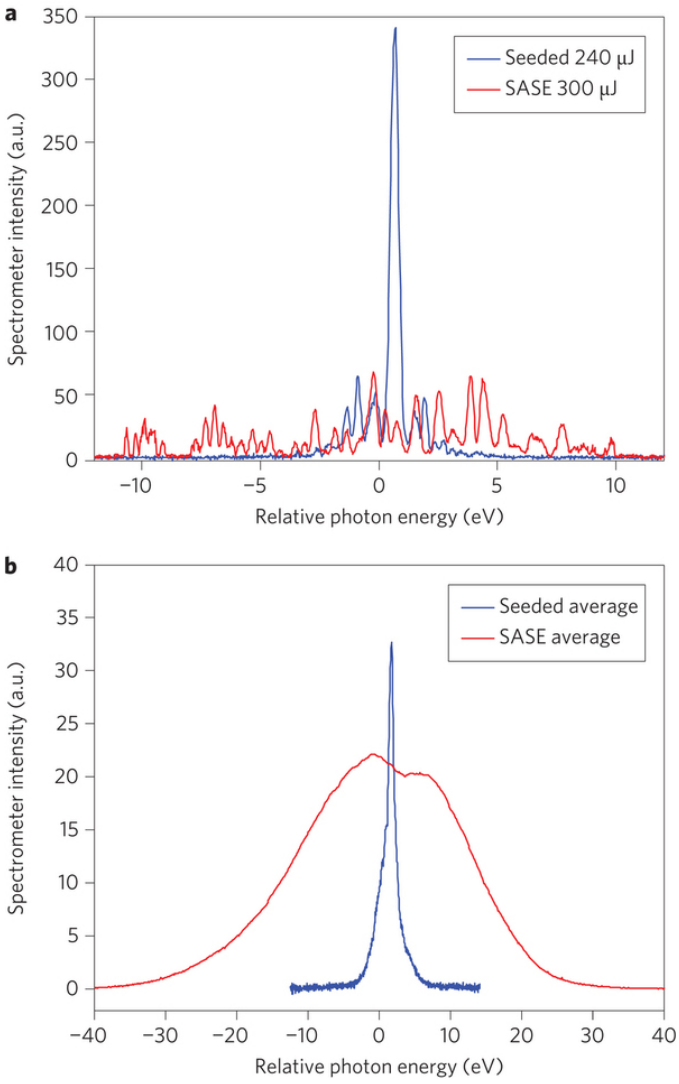

Figure 6.4: Single-shot (a) and averaged (b) X-ray spectrum in SASE mode (red) and self-seeded mode (blue). The FWHM single-shot seeded bandwidth is 0.4 eV, whereas the SASE FWHM bandwidth is 20 eV. Vertical scales have the same arbitrary units in both a and b. The chicane is turned off for the SASE measurements, but necessarily switched on for the self-seeded mode. Taken from [77].

The chicane strength has also been varied to scan the electron delay so as to trace out the monochromatic wake pulse generated by the diamond crystal. Because the gas detector

contains significant SASE background, we use the spectrometer signal and zoom into the narrow-bandwidth seeded spectra for this study. Figure 6.5 shows the seeded FEL intensity as a function of the chicane delay, reflecting the time dependence of the FBD intensity envelope, in reasonable agreement with FBD theory predictions. The peak seeded signal is reached at a chicane delay of 19 *fs*, in agreement with the value calculated by equation 6.2. The relatively large error bars for the data (standard deviation) indicate the fluctuating nature of the seeded power, as discussed above.

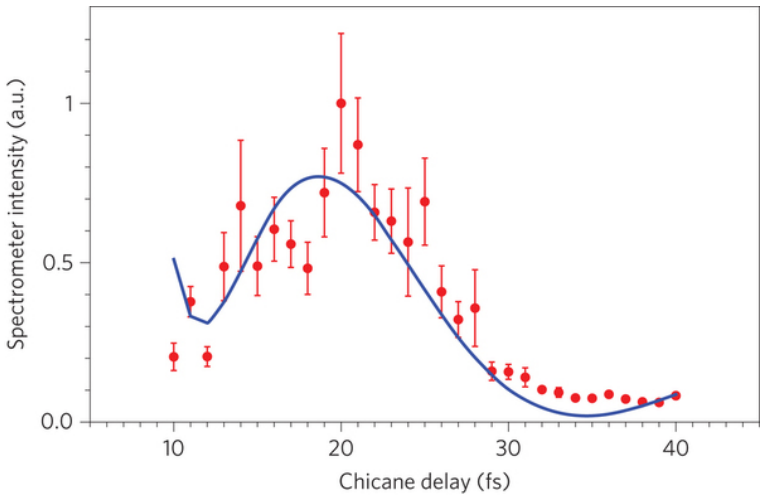

Figure 6.5: Seeded FEL intensity as a function of chicane delay, measured using the intensity of just the narrow seeded line on the X-ray spectrometer. The points are the spectrometer signal and the solid curve is the convolution of the diffraction theory prediction of equation (1) with the X-ray pulse duration. Crystal thickness and X-ray pulse duration are taken to be fitting parameters. The best fit is obtained when d=104 μm with a flat-top X-ray profile of 5.5 *fs*. Taken from [77].

Finally, in figure 6.6, we show the measurements of the gain length in the SASE undulator and in the seeded undulator.

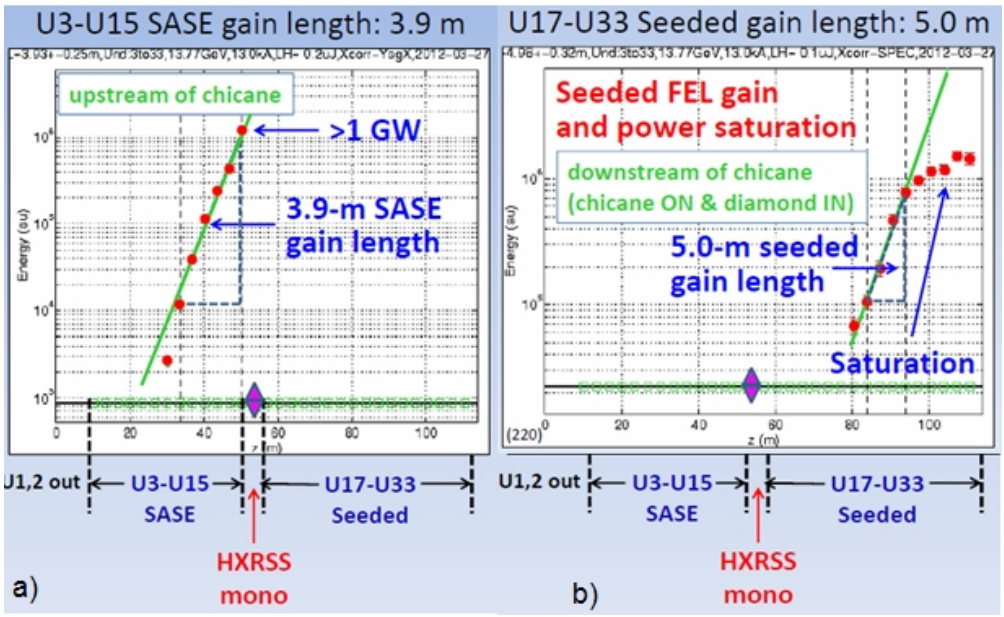

Figure 6.6: Gain length measurements in SASE undulator and seeded undulator. Courtesy of D. Ratner.

6.3 LCLS self-seeding experiment: simulations and results analysis

In this section, we present detailed simulations that can help to understand the system performance and optimization. The results of the self-seeding experiments are determined by the electron beam properties and by the energy and peak power of the seed amplified in the second undulator. Both are not completely known. The knowledge of the current beam profile and other beam slice properties is extremely difficult to obtain for the 20 pC and the 40 pC mode as the bunches have a duration of 10 fs. The current beam profile can be measured, with limited resolution, through a modification of the zero phase

technique described by [181]. The process of seed generation in the crystal has been studied in [175, 176]. Both these two studies predict, starting from two different approaches, a similar level of power. A measurement of the seed characteristics, even if not possible with the current experimental setup, seems to be very important for the understanding of experiments results. The seeding efficiency can be reduced by a misalignment or an angle between the electron beam and the seed. Knowledge of the global seeding efficiency and of the interplay between electron beam proprieties and the obtained FEL power and bandwidth it is important for planning regular users' utilization in LCLS and in the development of other machines [182]. In the present work, we try to derive as much as possible about the evolution of the FEL pulse in the two undulators from the experimental data using basic physics concepts. We can guess the fundamental characteristics of the electron bunch and the seed power from the experimentally derived model. Then we compare the result of these studies with start to end simulations starting from beam generated in the photoinjector by IMPACT-T [183] and tracked in the linac with elegant [165]. The simulations of the FEL process in the undulator are done with the code Genesis 1.3 [160]. Some beam parameters can be checked with measurements of current beam profile. Recently a technique based on a high energy resolution spectrometer has been implemented in LCLS to measure the longitudinal current profile of the 20 pC and 40 pC electron bunch. The third linac section operates at 0 degree RF crossing phase with no net acceleration to provide a linear energy chirp during the measurements of the beam profile. It has been shown that it is possible to have a one to one relationship between the longitudinal coordinate after the second bunch compressor and the energy coordinate after the third linac if a third chicane is located between the second bunch compressor and the third linac when the R_{56} of this third chicane

satisfies the following relation [181]:

$$1 + hR56 = 0 \tag{6.5}$$

where h is the linear chirp that the beam acquires in the third linac section. When this condition is satisfied the relation between the longitudinal coordinate after the second bunch compressor and the energy coordinate after the third linac is simply:

$$hZ_i = \delta_i \tag{6.6}$$

where Z_i and δ_i are the longitudinal and the energy coordinate of the i particle with respect to the centre of mass and to the mean energy respectively. The energy coordinate at the end of the linac depends only on the longitudinal coordinate of the particle in the beam after the bunch compressor. The beam is sent into a high resolution energy spectrometer and the energy is converted in the horizontal coordinate. The horizontal coordinate of the spectrometer screen corresponds to the longitudinal coordinate of the beam while the vertical coordinate of the screen corresponds to the vertical coordinate of the beam (see the top of the figure 6.8). Projection of the image along the horizontal coordinate yields the beam current profile. At this point the x profile recorded on the spectrometer screen is a magnified image of the beam longitudinal profile after the second compressor. The R_{56} of the second chicane is increased by a term that satisfies the relation (6.5) in the implementation of the method in LCLS. This is equivalent to adding a third chicane and it does not require hardware modifications. The profile of the beam is recorded as a function of the phase of the second linac. Figure 6.7 shows the bunch current profile measured with the technique

described above for two consecutive electron beam shots. The linac setting during these measurements is the same as that used during the FEL self-seeding experiments. We can see that the current profile changes significantly from shot to shot.

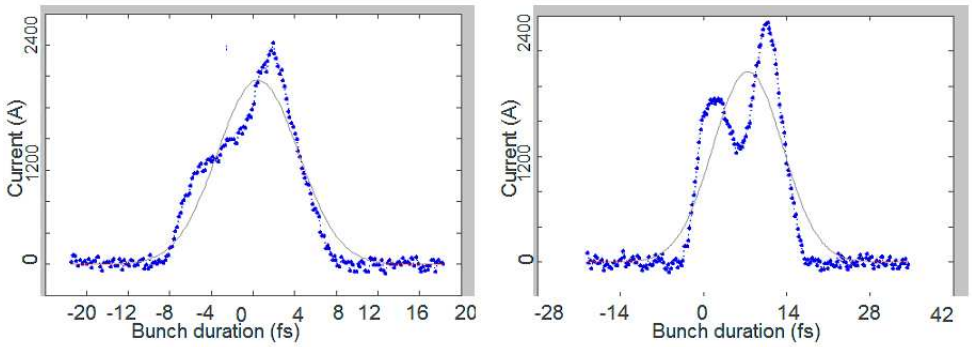

Figure 6.7: Bunch profile of two consecutive shots. The head of the bunch is at negative time.

An energy chirp is still present on the beam at the linac end and therefore the bunch can be compressed by the negative R_{56} of the transfer line leading to the undulator line. For this reason, the beam profile in the undulator is not exactly the one that it is measured by the described method. A correspondence can be established between the measured profile and the actual one in the undulator. In figure 6.8 we show the images on the spectrometer screen (on the top) and the corresponding current in the undulator obtained from linac simulations (on the bottom) for three different compression settings. The horizontal coordinate of the screen corresponds to the beam energy and to the longitudinal coordinate of the beam through the relation 6.5 while the vertical coordinate of the screen corresponds to the vertical coordinate of the beam. We can see that the shape of the electron beam current seen in the screen is preserved.

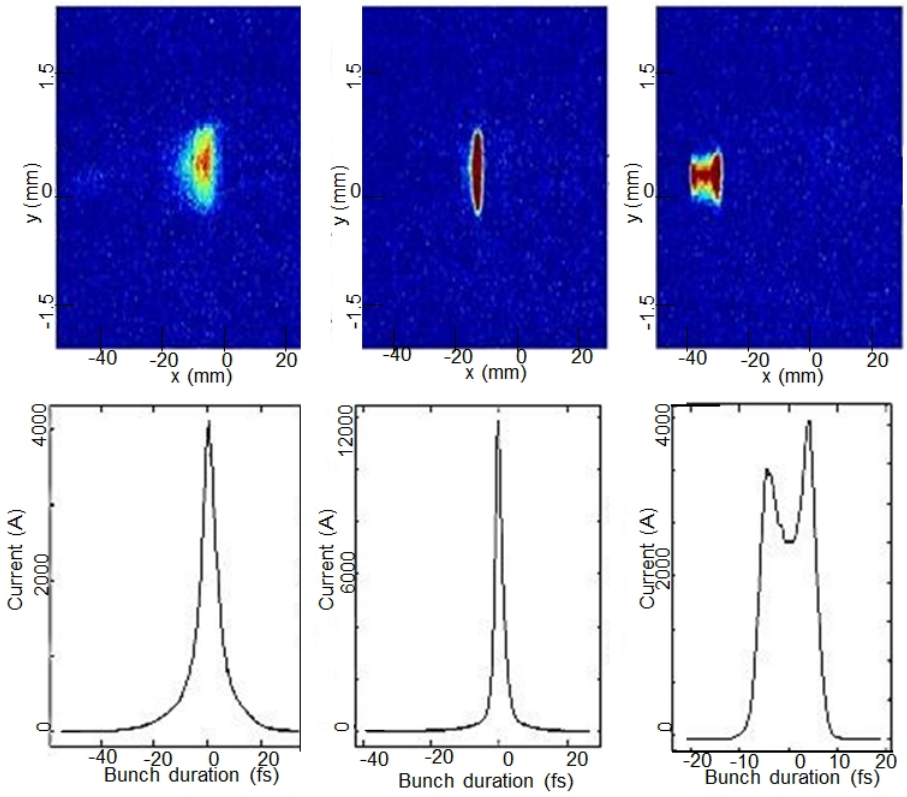

Figure 6.8: On the top: Three images of the electron beam on the spectrometer screen for three different compressions. On the bottom: The corresponding current in the undulator obtained from linac simulations for the same three compression settings used for the measurements shown above (courtesy of J. Wu).

A large number of pulses are characterized by a double horns distribution. We use such a beam produced in injector-linac simulations as starting point for the FEL simulations with Genesis 1.3. The current profile of the beam used and other slice parameters used in the start to end simulations are shown in figure 6.9. Figure 6.9a shows the beam current profile. Figure 6.9b shows variation of the mean energy of each slice along the beam, $\langle\gamma\rangle$, with respect to the mean beam energy γ_0 along the beam. Figure 6.9c reproduces the

variation of the slice energy spread along the beam.

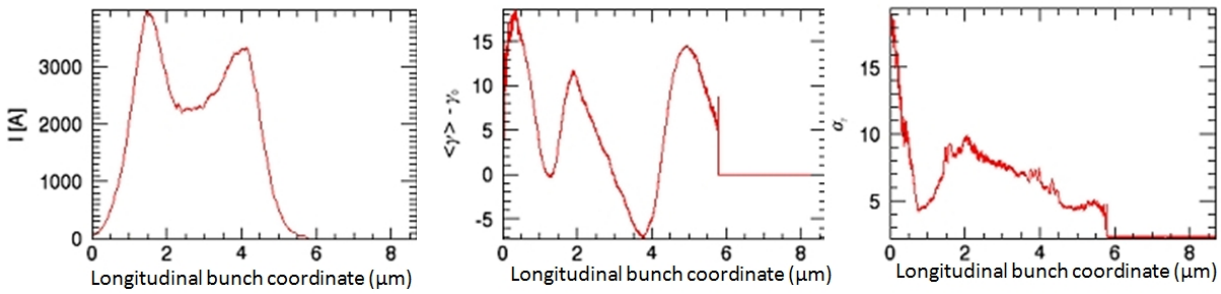

Figure 6.9: Current profile (a), energy profile (b) and energy spread profile (c) of the beam used in start to end simulations. The head of the beam is on the right.

Figure 6.10 shows the gain length calculated along the beam from Ming Xie's formula (2.43, 2.49, 2.50 and 2.51) [56] considering the energy spread, emittance and current from the elegant simulation. We see that the gain length in the high current horns is close to 2.5-3 m while in the core of the bunch it is about 4m.

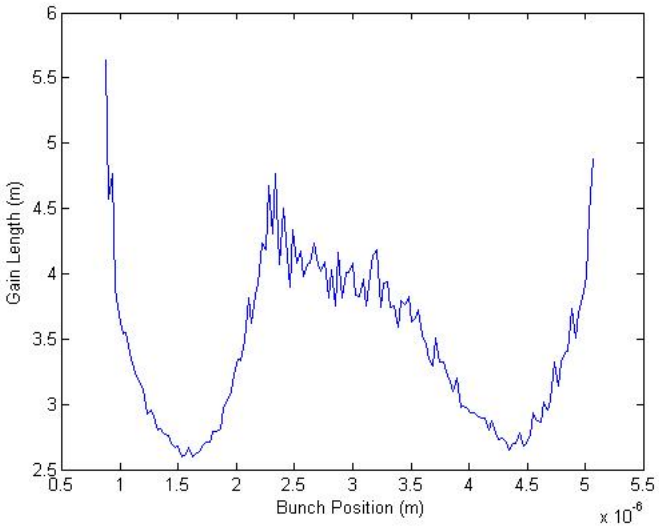

Figure 6.10: Gain length along the longitudinal coordinate of the bunch calculated using Ming Xie's formula [56] considering the energy spread, emittance and current from the elegant simulation.

Starting from an estimated value of the equivalent shot noise seed power [56] we calculate the evolution of the FEL pulse and energy spread in high-gain regime along the SASE undulator using the equation 2.63. Figure 6.11 reports the finally obtained slice energy spread (figure 6.11a) and FEL pulse for several lengths of the SASE undulator (figure 6.11b).

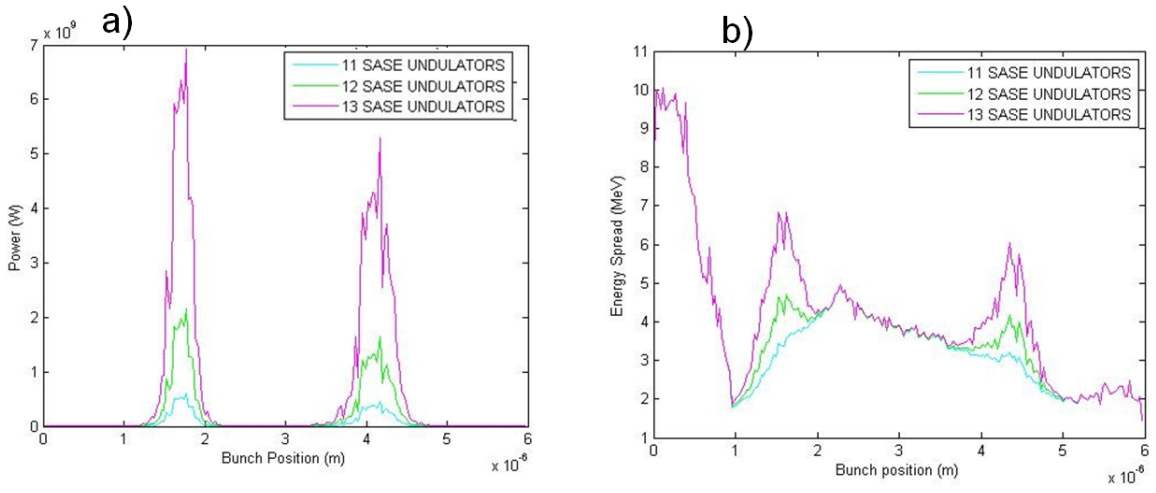

Figure 6.11: a: Energy spread. b: FEL power evolution along the SASE undulator. Cyan curve refers to eleven undulators, green is for twelve undulators and magenta is for thirteen undulators.

The variation of the gain length along the bunch profile affects the evolution of the energy spread and of the FEL power along the undulator. Twelve undulators are equivalent, in the horns and in the core of the bunch, respectively, to about 15 and 10 gain lengths. The energy spread is increased in a significant way only in the horns. The horns produce a great part of the total FEL power too. Then we calculate the value of seeded FEL pulse mean power as function of the number of the SASE undulator sections. The power shown in figure 6.11b) is multiplied for several values of monochromatic efficiency and used to evaluate the evolution of the seeded power according to the equations 2.56 and 2.63. The seed is considered as flat with a constant power completely covering the electron beam. For each number of SASE undulators used, we have several values of the power obtained at the end of the second undulator according to the considered efficiency. The results are shown in figure 6.12.

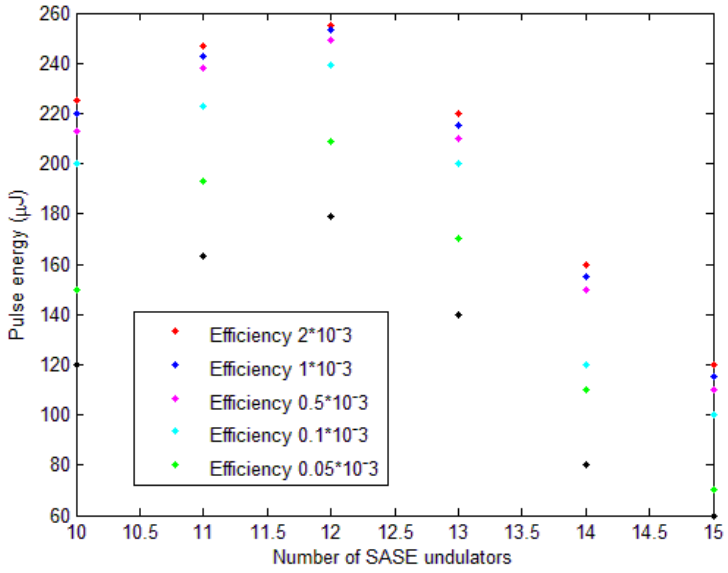

Figure 6.12: Seeded main power versus the number of SASE sections for several monochromatic efficiencies.

This analytical model predicts that the maximum output energy is produced using only twelve undulator in the SASE section.

Now we performed FEL simulations of the SASE undulator with the code Genesis 1.3 using the beam illustrated in figure 6.9. Figure 6.13a shows the growth of the pulse energy along the SASE undulator averaged over thirteen simulations performed with different seeds for the shot noise [56]. The gain length is $\approx$3.5 m. The pulse energy after thirteen undulators is 7$\pm$3 μJ. The typical temporal shape of the FEL pulse produced in thirteen SASE undulators is shown in figure 6.13b. The SASE pulses have a shape characterized by two narrow peaks. The energy spread profile after twelve, thirteen and fifteen SASE undulators is shown in figure 6.13c.

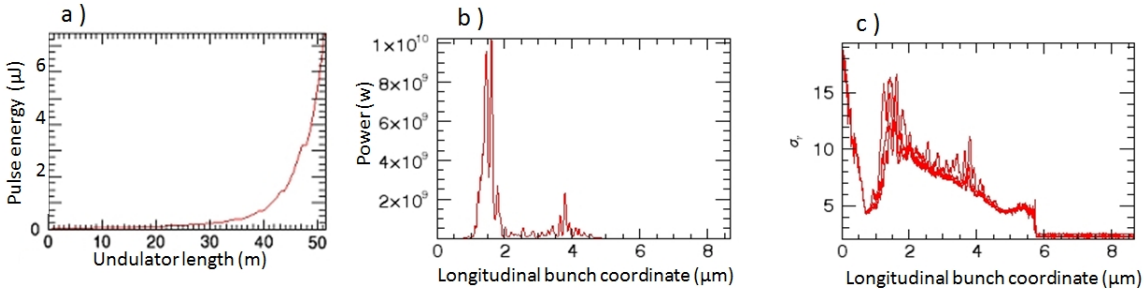

Figure 6.13: a: Growth of the pulse energy along the SASE undulators chain averaged on thirty simulations performed with different seed for the shot noise. The gain length is ≈3.5 m. The pulse energy after thirteen undulators is $7 \pm 3\,\mu J$. b: Typical temporal shape of the FEL pulse produced in thirteen SASE undulators. The SASE pulses have a shape characterized by two high and narrow peaks. c: Energy spread profile after twelve, thirteen and fifteen SASE undulators. The head of the beam is on the right.

We see that the evolution of the SASE pulse, and consequently of the energy spread, in the head of the bunch is reduced with respect to the analytical calculation. This is an effect of the energy profile (figure 6.9b), of the wake fields and of the linear taper used to compensate wake fields and synchrotron radiation. For this reason a part of the beam, located near the head of the bunch is still not spoiled by energy spread after thirteen undulators (see figure 6.13c) and the optimum number of SASE sections is increased by one with respect to that calculated analytically.

Almost all of the self-seeding experiments have been done using 13 undulators in the SASE stage and this partially confirms the simulations. Experimentally, a gain length of 3.9 m meter has been observed in the SASE undulator, and the measured energy at the crystal is ≈10 μJ consistent with the simulations.

SASE is an exponential amplification of the shot noise. Using the knowledge of the noise power, we can estimate the temporal duration of the gain medium, the portion of the

electron beam, that produces 10 μJ in thirteen sections with the measured gain length. Using the gain length calculated for the horn, and considering one gain length for lethargy we obtain that a shot noise energy of about *0.01 nJ* is amplified to produce ≈10 μJ after thirteen sections. The shot noise power is in the range of 2-5 kW for the current level of the 40 LCLS beam. Considering a shot noise power in this range, we obtain that almost only a portion of the beam as long as ≈3 *fs (1μm)* is lasing. This estimate is also consistent with the start to end simulations which indicate that almost only the horns of the beam are contributing to produce the emitted radiation. The temporal profile of the FEL pulse at the end of the SASE undulator is dominated by two very narrow structures, as shown in figure 6.12b, confirming the supposed scenario.

Now we performed simulations of the seeded undulator with the code Genesis 1.3. We show the results of these simulations in the figure 6.14. The figure 6.14a reports the growth of the pulse energy along the seeded undulator. The seed used in this simulation has a peak power of 5 MW in agreement whith simulations of the SASE undulator and with the expected monochromator efficiency.

The gain length obtained by simulation is 5 m in good agreement with the experimental results (see figure 6.6a). The pulse energy after thirteen seeded undulators is about 250 μJ. The maximum pulse energy obtained in the hard X-ray self-seeding experiment at the end of the seeded undulator, including 13 sections (U17-U29), is in the range of 200-250 μJ. The temporal shape of the FEL pulse at the end of the thirteen undulator section is shown in figure 6.14b. The pulse has a duration (FWHM) of ≈10 fs. Figure 6.14c reproduces the spectrum of the seeded pulse obtained in this simulations. The zero point on the horizontal axis refers to the mean energy of 8331.5 eV (0.14881 nm). The FWHM relative bandwidth

of the simulated spectrum is $5{\cdot}10^{-5}$.

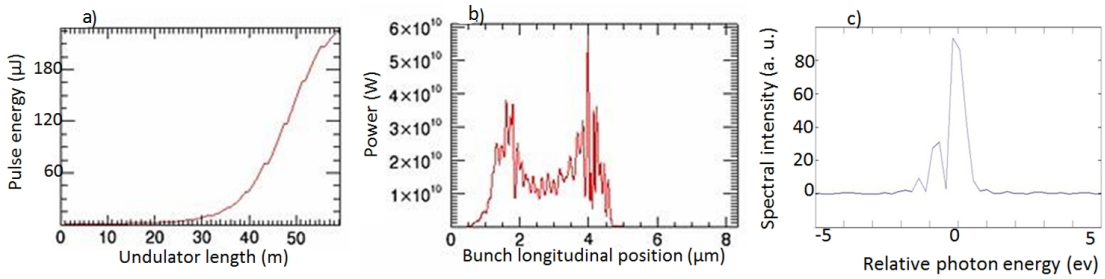

Figure 6.14: Figure 6.14a reports the growth of the pulse energy along the seeded undulator. The seed used in this simulation has a peak power of 5 *MW*. The gain length obtained by simulation is 5 *m*. The pulse energy after thirteen seeded undulators is about 250 μJ. Figure 6.14b reports the temporal shape of the FEL pulse at the end of the seeded undulator, composed of thirteen undulators, is shown in figure 6.14b. The pulse has a duration (FWHM) of ≈10 *fs*. Figure 6.13c reproduces the spectrum of the seeded pulse obtained in these simulations. The 0 in the horizontal axis refers to the mean energy of 8331.5 *eV* (0.14881 *nm*). The FWHM relative bandwidth of the simulated spectrum is $5 \cdot 10^{-5}$.

Figure 6.15 shows the simulated growth of the pulse energy along the seeded undulator for two values of the initial seed power, 5 *MW* and 1 *MW*. We see that the pulse energy at U29, corresponding to the first thirteen undulators downstream of the crystal used in the first experiment reported in the section 6.2, is dependent on the initial seed power while the full radiator composed of seventeen sections is almost saturated. These simulations were done using only a linear taper to compensate the synchrotron radiation and wake fields.

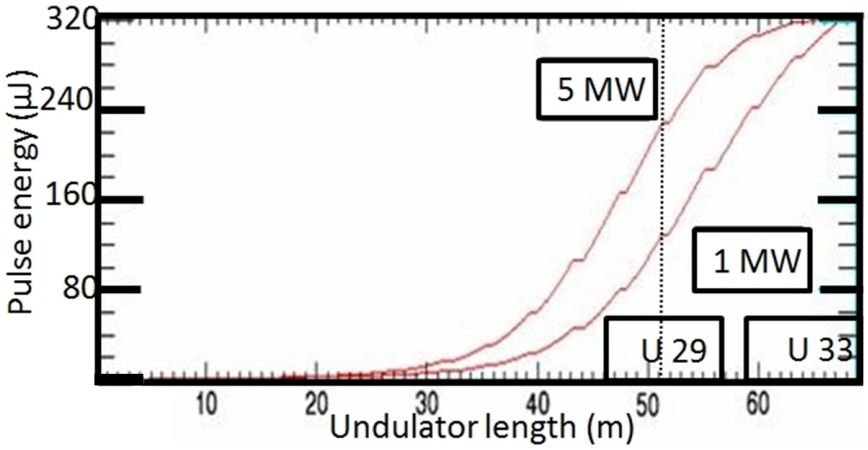

Figure 6.15: Simulated growth of the pulse energy along the seeded undulator for two values of the initial seed power, 5 MW and 1 MW. U29 corresponds to the first thirteen undulators downstream of the crystal used in the first experiment reported in the section 6.2.

The fluctuations of the seed power, inherited from the stochastic nature of SASE, complicate the utilization of the quadratic taper to extract more energy above the saturation level. Indeed different values of the seed required different locations at which the quadratic taper should starts. High power seeds require to start the quadratic taper closer to the crystal compared to the low power seeds. The fluctuations of the final energy related to the seed energy are larger when the taper is optimized for the maximum seed power available and saturation is not observed at U33. The RMS energy jitter at the end of the linac is 0.05% and 30% of the pulses is not seeded due to the energy fluctuation of the electron beam as the bandwidth of the seed is of the order of $\approx 10^{-5}$ [176, 177] and this increases the pulse energy fluctuations. For these two reasons pulse energy fluctuations of the order of 30%-50% are usually observed even when 17 undulators are used after the crystal.

Now we try to derive the amplified seed energy and the maximum seed power from the available data. Considering the final maximum energy of $250\mu J$ obtained in thirteen seeded

undulators, the gain length of 5 m and one gain length for lethargy, we can state that the amplified maximum seed energy is 50 nJ. Supposing that the seed peak power is about 5 MW we obtain that the amplification process happens on a part of the beam about 10 fs long. This is in good agreement with the shape of the pulse from simulations. Now we try to estimate the seeded FEL pulse length from spectral considerations. As stated before the single-shot relative bandwidth for good high energy shots corresponds to a Fourier transform limited pulse of 4-5 fs. The pulse can still be longer than 5 fs in the case that its Fourier limited bandwidth is shorter than the measured one with the pulse bandwidth increased by a chirp on the beam. In particular, the experimental seed bandwidth and the estimated pulse length of 10 fs determines a time-bandwidth product that is about 2 times the Fourier limited one and this corresponds quite well to the simulation results. The FEL seeded pulse obtained by spectral consideration is still shorter than the electron beam but longer than the SASE one. Then we can guess that the core of the beam emits a good part of the FEL energy but the horns, or at least one horn, still dominates. The start to end simulations confirm this scenario (figure 6.13b).

Not all the seeded pulse have a pure Gaussian mode like that in figure 6.4. Some spectrum (see figure 6.16) shows sidebands and multiple peaks and this pulse to pulse spectral variation causes the spectral broadening seen in the average spectrum.

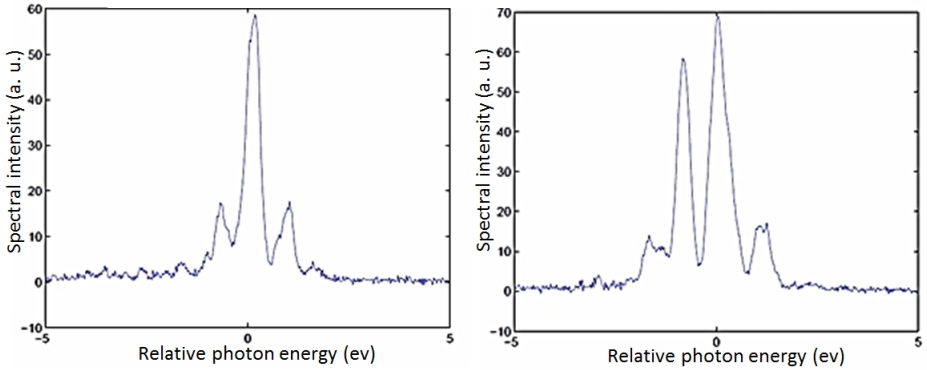

Figure 6.16: Self-seeded single-shot measured spectrum. 13 SASE undulators + 13 seeded undulators.40 pC beam. Courtesy of A. Lutman.

Some spectra obtained in simulation are shown in figure 6.17. The spectrum shown on the left is obtained in start to end simulation with the second undulator detuned with respect to the value that produces the spectrum shown in figure 6.17. The spectrum shown on the right is obtained using in simulation a flat energy distribution and the current profile from start to end simulation.

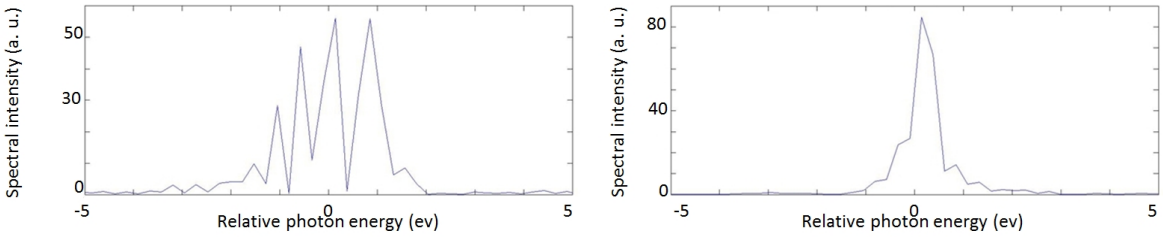

Figure 6.17: Self-seeded single-shot simulated spectrum. 13 SASE undulator + 13 seeded undulator. 40 pC beam. start to end simulation on the left. The spectrum shown on the right is obtained using in simulation a flat energy distribution and the current profile from start to end simulation.

The electron beam energy and shape is changing from shot to shot and this explains the energy and spectral shot to shot fluctuations observed in the experiment. In the measure-

ments shown in figure 6.16 and in the simulation in 6.17 only a linear taper is used to compensate synchrotron radiation and wake field losses. We have presented studies on the hard X-ray self-seeding experiments at LCLS. Experimental data and start to end simulations show that in the SASE undulator, the radiation is produced mainly by the horns of the beam while in the seeded undulator the core of the beam starts to emit radiation. The gain lengths and the level of pulse energy measured experimentally at the end of the two undulators (SASE and seeded undulator) are in agreement with the simulations. Simulations suggest that 10 μJ SASE radiation produced in the SASE stage (U3–U15) generates sufficient seed power (5 MW) but degrades the electron beam energy spread. As a result, the FEL signal grows slower in the seeded stage due to increased energy spread and produces 250 μJ FEL pulse energy after 13 undulator segments (U17–U29), without reaching saturation. The simulations also indicate that the seeded FEL spectra are quite sensitive to the detailed longitudinal phase space distribution of the electron beam and explain the fluctuations of the shape of the single-shot spectra and the broadening of the averaged spectrum. Further studies have shown the impact of the jitter of the electron beam energy on the energy stability of seeded pulse.

Chapter 7

SASE with tapered undulator and chirp

In this chapter we will describe a method to improve the longitudinal coherence of SASE radiation based on a linear energy chirp and on undulator tapering [74, 75]. The FEL line used to implement this method is composed of a single long undulator as in the SASE FEL. In this case the undulator is strongly tapered. It has been shown that the effect of a linear energy chirp on the FEL gain [74] is equivalent to that of a linear undulator tapering. Then it is possible to compensate the FEL spectrum broadening, caused by the undulator tapering, by means of a linear energy chirp. It is possible, in this way to produce a single Gaussian spike with a spectrum close to Fourier transform limit. We present, in this chapter, the results of the first experiment done to test this method. These experimental studies have been done at the SPARC test facility. This method, as it is self-seeding, does not use a seed laser and can be extended, as in the original proposal, down to the hard X-ray regime.

7.1 Compensation of linear chirp by undulator tapering

This scheme combines an electron beam energy chirp with a chosen undulator field taper, i.e., a smooth variation of peak magnetic field along the beam propagation axis, implemented in SASE configuration without an external seed. The basic idea behind this scheme is that a symmetry between the energy chirp and the undulator tapering exists [74] and can be understood by considering the radiation field acting on some test electron emitted at a retarded time from an electron behind. A radiating electron, in the presence of an energy chirp on the electron beam, has a detuning due to an energy offset, while it has the same detuning, in a tapered undulator, because the undulator parameters were different at the retarded time. We will see that these two effects can compensate each other. In case of a linear chirp on the electron beam, the mean ''local'' energy varies as:

$$\gamma(s) = \gamma(s_0) + \alpha(s - s_0) \tag{7.1}$$

where s is the longitudinal bunch coordinate, s_0 represents the centre of the electron bunch in its drifting reference frame and α quantifies the degree of energy chirp. The energy chirp serves to detune the beam's local resonant frequency. The resonant frequency varies along the beam in the presence of a chirp and the central radiation produced in a SASE configuration follows the resonance frequency. The higher velocity of the light with respect to that of the electrons produces a slip of the radiation. As the FEL radiation produced upstream propagates forward in s, it falls out of the local gain bandwidth when it slips a distance of the order of:

$$\delta s \sim \frac{\rho \gamma m_0 c^2}{2\alpha} \tag{7.2}$$

where ρ is the Pierce parameter introduced in section 2.4. This effect can be compensated, however, by choosing the undulator taper to allow the continuous gain of a spike initiated in the rear of the bunch as it moves forward in s with the appropriate velocity, as illustrated in figure 7.1. Analysis of this slippage is complicated by the modification of the radiation spike's velocity in the presence of gain; the peak of a spike in the exponential gain regime moves at a velocity [39]:

$$\beta_L \sim \frac{3\beta_Z}{\beta_Z + 2} \tag{7.3}$$

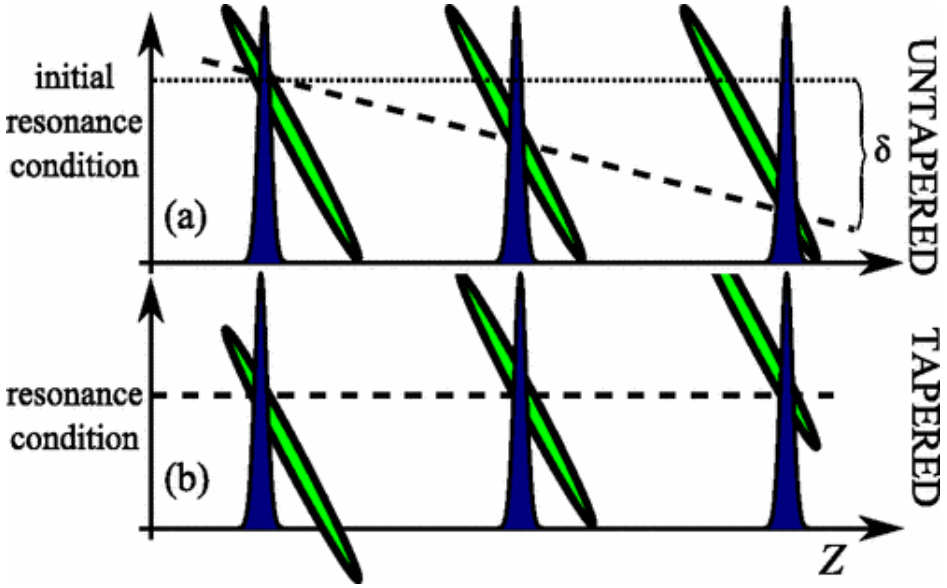

Figure 7.1: Propagation of a field spike (blue) developing at the rear of a chirped e-beam (green) for (a) untapered case, and (b) tapered case as a function of z. Vertical axes indicate the resonant condition as a function of the relative position between the beam and radiation, δ is the final detuning in the untapered case. In (a) the slippage leads the spike out of resonance, when the chirp is combined with an appropriate undulator taper (b), the resonance can be preserved. Taken from [75].

Approaching saturation, the radiation peak propagates at a higher velocity than β_L, closer or even higher than unity, because of the pulse shortening associated with the electron synchrotron oscillation [184]. Above saturation, the front of the pulse moves forward at c. The chirp-taper combination discussed above also affects the spike propagation velocity. Indeed, the chirp-induced energy change observed at the peak of the radiation pulse may be expressed as:

$$\gamma(z) = \gamma(0) + \alpha z \eta \frac{\omega_U}{\omega_0} \tag{7.4}$$

where z is the coordinate along the undulator, $\gamma(0)$ is the beam energy at the undulator entrance (z=0) and at the position along the bunch where the spike will eventually grow, and η is a coefficient accounting for an arbitrary propagation velocity of the radiation. Inserting $\gamma(z)$ in the resonant condition and solving for the undulator K provides a taper scaling which preserves the desired resonance condition during propagation as:

$$K(z) = \sqrt{\frac{\omega_U}{\omega_0}\left(\gamma_s + \alpha z \eta \frac{\omega_U}{\omega_0}\right)^2 - \frac{1}{2}} \tag{7.5}$$

In such a regime the correlated energy spread is compensated only for spikes drifting with the appropriate velocity associated to the taper. When the cooperation length is of the same order of the electron bunch length, only a single radiation spike reaches full saturation. We will report on the first experimental demonstration, at the SPARC FEL test facility, of the generation of short pulses in a single-pass amplifier with this combined chirp-taper method [74, 75] in the next section.

7.2 SPARC results

Longitudinal beam compression is achieved, at SPARC, by electron beam injection off crest in the first linear accelerator (linac) section, close to the zero crossing phase, resulting in velocity bunching that leaves a strong chirp in the longitudinal phase space and subsequent increase of the peak current [150, 151]. The measured longitudinal phase space at the linac exit after velocity bunching shows a residual chirp, of $-8.72 \pm 2\, keV/m$, with the

uncertainty arising mainly due to linac phase jitters of 1degree, combined with the sensitivity of compression to injection phase errors. The experiment was done with a mean energy of 115.2 MeV, projected (slice) energy spread of 1.33 (0.7) MeV and RMS electron bunch length of 0.42 ps, corresponding to a peak current of 380 A. In the transverse plane the beam was matched to the undulator with Twiss parameters (averaged over the undulator length) $\langle\beta_x\rangle = \langle\beta_y\rangle = 1.5\,m$ and with projected emittances $\epsilon_x/\epsilon_y = 2.7/3$ $mm{\cdot}mrad$. In these conditions the chirp with its associated gain degradation prevents the FEL from reaching deep saturation, in the absence of tapering. An in-vacuum spectrometer [151] is used as the main radiation diagnostics. Calibrated gratings and a CCD detector (Versarray, 1300B-Princeton Instruments) enable the simultaneous determination of spectral properties of the observed FEL radiation and of the pulse energy. Figure 7.2 shows a typical single-shot spectrum obtained with the untapered undulator, i.e., six sections tuned at the resonance of 540 nm for the mean beam energy. The strong chirp in the electron bunch produces a broadband spectrum extended over the full spectral window. The analysis of a sequence of 100 spectra gives an average (RMS) pulse energy of $7.8 \pm 8\mu J$, a mean central wavelength of $537 \pm 5nm$ and an RMS linewidth of $8.8 \pm 2nm$.

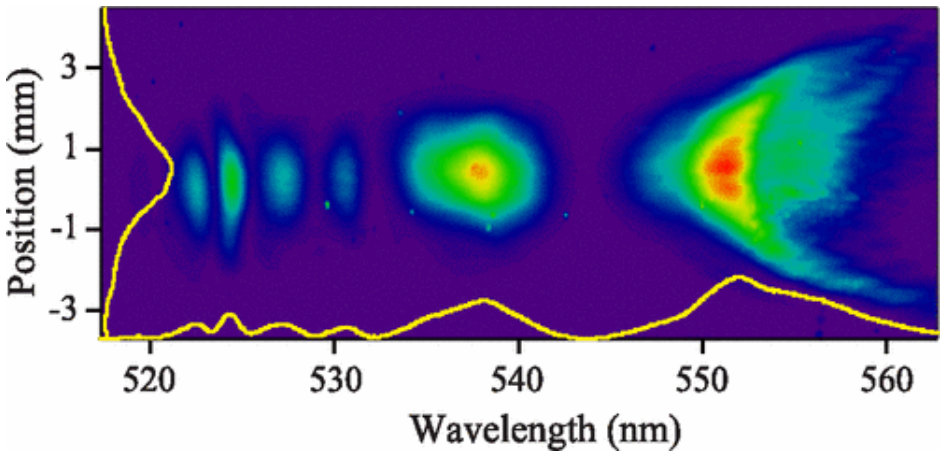

Figure 7.2: Single-shot spectrum acquired with all undulators set at nominal resonance of 540 *nm*, with spectrometer entrance slit opened at 100 m, corresponding to a resolution of 0.17 *nm*. The vertical axis represents the non-dispersive dimension at the slit. Taken from [75].

In order to compensate the chirp, each undulator module was progressively tuned, commencing with the first, while minimizing the spectral width (see figure 7.3 Taper A). This process results in an increase of the pulse energy, a narrowing of the spectrum and in a shift of the mean wavelength down to $521 \pm 3.7\,nm$. The central wavelength was restored to $540.1 \pm 4.4\,nm$ by tuning the undulator gaps to the values corresponding to the solid curve in figure 7.3 (Taper B).

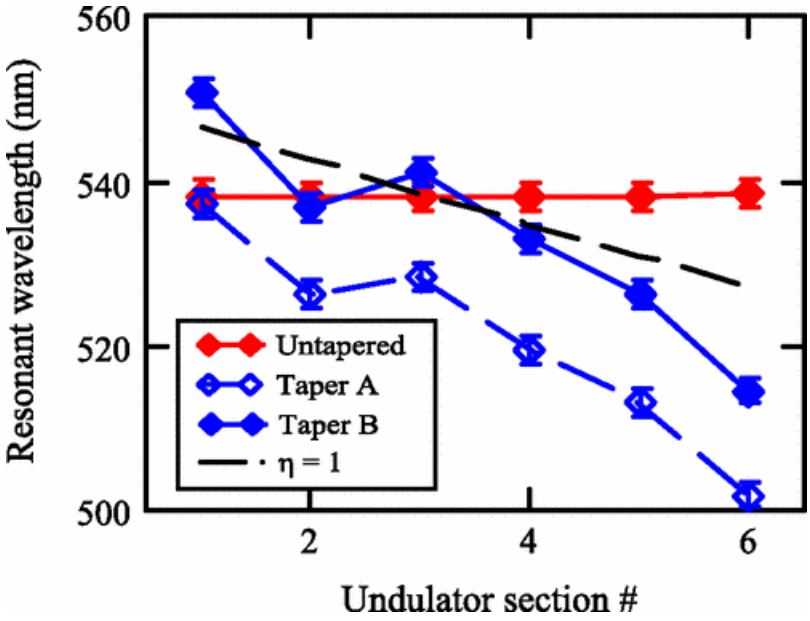

Figure 7.3: Resonant frequency for a 115.2 *MeV* electron beam in the six undulators, untapered and tapered case (Taper A). Taper B after compensation of the observed wavelength blueshift. Taken from [75].

The black dashed line in figure 7.3 indicates the trend of a taper compensating a spike traveling at the velocity c (η =1), as given by equation 7.5. Discrepancies between this last curve and Taper B in the final part of the undulator may be ascribed to non-linearities in the energy chirp, but also to the fact that the taper is simultaneously compensating the electron energy loss. This is confirmed by the extracted energy per pulse. The analysis of the sequence of 100 spectra, as shown in figure 7.4, gives a pulse energy of average value of $139 \pm 97\,\mu J$ and RMS linewidth of $4.3 \pm 1.3\,nm$.

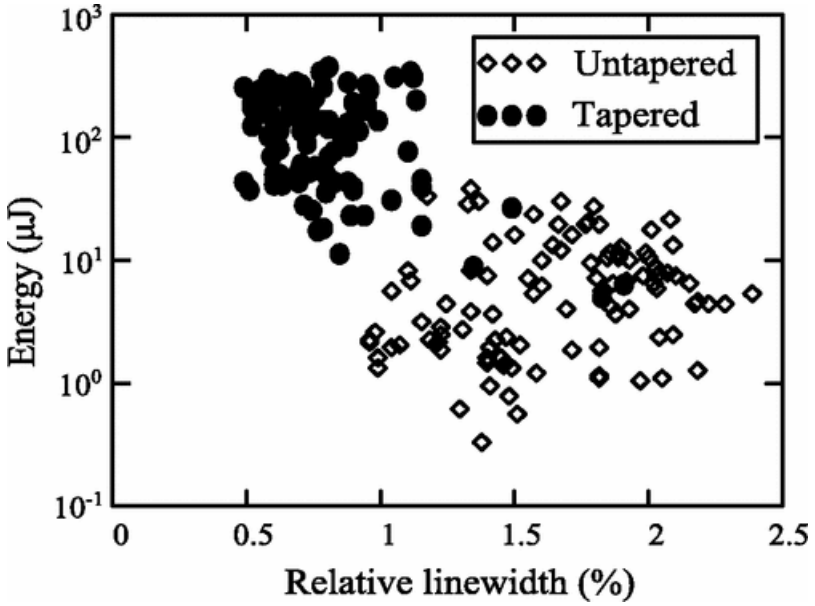

Figure 7.4: Energy vs. relative spectral width for untapered and tapered cases. Taken from [75].

Figure 7.5 compares the experimental output energies with the results of 100 cases simulated with Genesis 1.3 [160]. The RMS pulse energy fluctuation is ≈70% in the experiment, while it is 11% in the Genesis 1.3 simulations including only the intrinsic electron beam shot noise. This value increases up to 50% (distribution (A) in figure 7.5) when a correlated stochastic variation of 28% in the pulse peak current and time duration, compatible with a phase jitter in the first linac section of 1 degree, is introduced. Distribution (B) in figure 7.5 results from the additional fluctuation of the emittance (50%) and of the slice energy spread (13%) which can be attributed to this phase jitter.

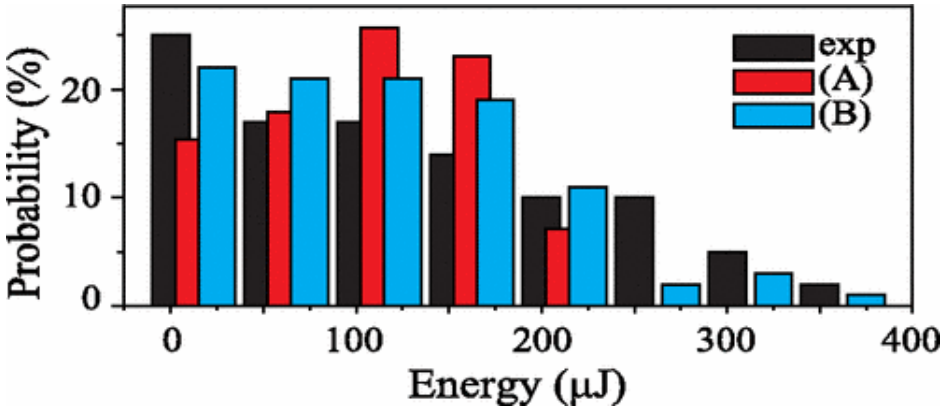

Figure 7.5: Histogram of the pulse energy distribution given by 100 measurements (exp), and by 100 Genesis 1.3 simulations, where statistical fluctuations of peak current and bunch length (A) and also emittances and energy spread (B) were introduced. The listed beam or undulator parameters were used, except for the slice emittances (1-4 *mm.mrad*) and relative slice energy spread ($1.7{\cdot}10^{-3}$) which were chosen to match measured mean pulse energy. Taken from [75].

Distribution (B) in figure 7.5 results from the additional fluctuation of emittances (50%) and slice energy spread (13%) which can be attributed to this phase jitter. About 50% of the acquired spectra were characterized by a pattern similar to that shown in figure 7.6a, where typical SASE spikes are absent and the spectrum is composed of a single coherence region. Image in figure 7.5b, obtained by post processing the Genesis 1.3 simulation data with an algorithm introduced to model the spectrometer input slit or grating transformations to reproduce the image on the CCD camera, exhibits a similar form. While the number of single spike events in the simulations (30%) was lower than in the experiment, the agreement in the details of the reconstructed spectra in these cases is striking. A Gaussian profile fitting the main structure in the spectrum of figure 7.6 has a standard deviation of 1.45 *nm*. It likely results from the contribution of a partially non-linear chirped radiation field spike [185]. A Fourier limited pulse with the same width would have a RM duration of 50 *fs* and

a peak power of about 2 *GW*.

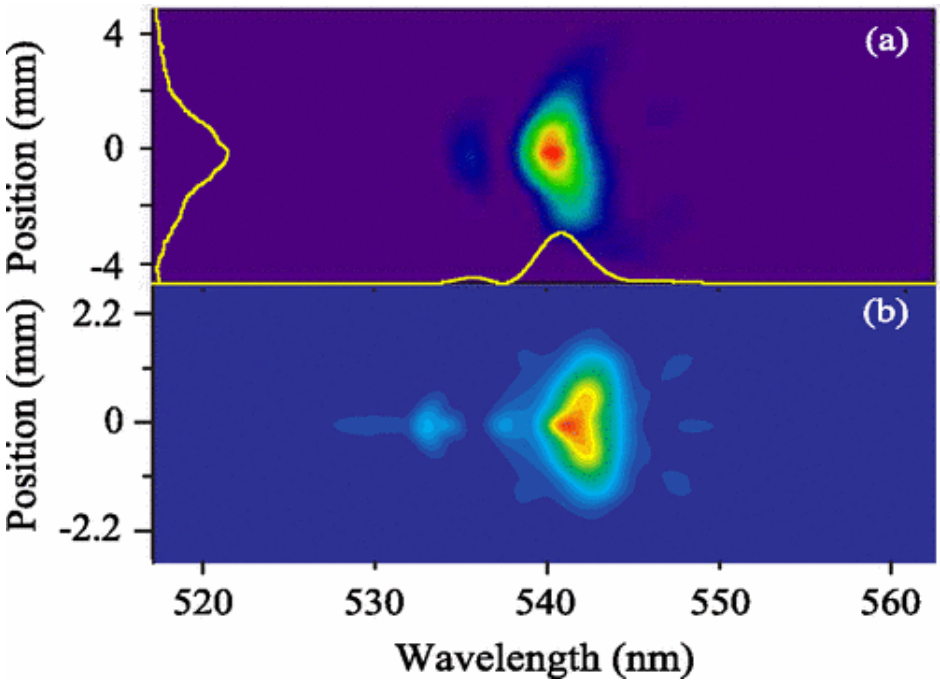

Figure 7.6: Typical FEL spectrum showing a single spike from the experiment (a) and from the Genesis 1.3 simulation (b). The total pulse energy is 300 μJ. Taken from [75].

In this chapter, we have demonstrated the possibility of generating isolated spike radiation pulses in a single-pass FEL operating in SASE mode, by combining a chirped electron beam with a tapered undulator. This was obtained without an increase in the gain length or loss of efficiency, but yielding an increase, by a factor of 20, in the pulse energy due to the involvement of the entire beam in the FEL gain. This higher efficiency is accompanied by a narrowing of the spectral width. These studies provide a further insight into ways for controlling the longitudinal coherence of SASE FELs that are of particular interest for sub-*fs* X-ray radiation applications.

Chapter 8

Conclusions

The need of coherent and intense pulsed radiation is spread among many research disciplines, such as biology, nanotechnology, physics, chemistry and medicine. The synchrotron light from traditional sources only partially meets these requirements. A new kind of light source, free-electron Lasers (FELs), has been conceived and developed in the last decades to provide radiation in VUV/X-ray regime with characteristic beyond the reach of conventional light sources. More precisely, SASE FELs such as LCLS, FLASH and SACLA produce regularly short (pulse duration$\leq 100\,fs$), intense (peak power up to tens of GW) VUV and X-ray radiation pulses characterized by good transverse coherence but poor longitudinal coherence, relevant shot-to-shot central frequency and power fluctuations. The improvement of the longitudinal coherence of the radiation in VUV and X-ray regime is a very valuable goal for the whole scientific community. In fact, the transverse coherence and the large photon flux characterizing these sources have opened up new perspectives for single-shot imaging, and for other techniques allowing multi-dimensional spectroscopy and other sophisticated

experimental methods to study a wide class of relevant phenomena.

In this work we have presented the experimental results of three techniques aimed at further improving the spectral and temporal quality of SASE FEL light. The first technique is high-gain harmonic generation (HGHG). We have presented the commissioning of FERMI@Elettra FEL1 line. At the beginning of our work, this scheme was successfully tested down to $\approx$100 nm. An energy pulse of about 350 μJ, 200 μJ and 100 μJ has been measured at 52 nm (fifth harmonic of the seed), at 26 nm (tenth harmonic of the seed) and at 20 nm (thirteenth harmonic of the seed). The time-bandwidth product was about 0.55, close to the one of a Gaussian pulse, in the range considered (52 nm-20 nm) revealing a good longitudinal coherence. First user experiments have just been performed using the light pulses delivered by FEL1, featuring the complete commissioning of this facility.

The second technique described is self-seeding, applied to hard X-rays. We have presented the results of the experiments done at LCLS (in which we have actively participated) and the simulations we have performed in order to interpret the obtained results. A dramatic improvement of the bandwidth and coherence of the light pulse in the self-seeded mode of operation has been observed with respect to SASE. The mean bandwidth reduction was about a factor 10, with good shots presenting a bandwidth reduction of a factor 50 with respect to SASE.

Finally, we have demonstrated the possibility to reduce dramatically the spectral width of SASE mode, generating isolated radiation spikes, without the increase of the gain length or loss of efficiency, by combining a chirped electron beam with a tapered undulator. Even in this experiment, carried out at SPARC, the importance of the electron beam properties to define the final quality and reliability of the radiation obtained, has been observed.

All these studies provide a further insight into ways for improving the longitudinal coherence of SASE FELs. In conclusion, this work provides new experimental results supporting the idea of using FELs as light sources capable of generating fully coherent and powerful pulses in the VUV and X-ray spectral regime, and confirming the importance of the electron beam quality to reach spectral purity and high flux of these pulses.

Any of the schemes here presented can be applied to other facilities and extended to other wavelengths.

Double stage of HGHG in fresh bunch a been recently demonstrated by the first commissioning of FEL2 at FERMI@Elettra. Activities are ongoing for optimization and to extend the spectral purity and stability of seeded FELs down to the soft X-ray regime appealing for scientific applications.

The LCLS experiment has shown that self-seeding requires a more stable electron beam with respect to SASE to reach the full potential and optimization studies are ongoing in this direction at SLAC with other studies to reach the Terawatt power level through tapering. A self-seeding experiment in the soft X-ray regime is in preparation. Other SASE facilities are considering self-seeding options in the soft and hard X-ray regime.

The SASE operation with a chirp on the electron beam energy and the tapered undulator has been demonstrated only at relative long wavelength ($\approx 500\,nm$) but can be extended to VUV and X-ray regime.

Appendix A

Abbreviations

Abbreviations	Definition
BC	bunch compressor
BPM	beam position monitor
CF	compression factor
CSR	coherent synchrotron radiation
LSC	longitudinal space charge
FEL	free-electron laser
FLASH	free-electron laser in Hamburg
FWHM	full width at half maximum
HERFDX	horizontal high energy RF deflecting cavity
HERFDY	vertical high energy RF deflecting cavity
HGHG	high gain harmonic generation
LCLS	LINAC coherent light source
LERFD	low energy RF deflector
LINAC	linear accelerator
OTR	optical transition radiation
RF	radio frequency
RMS	root mean square
SASE	self-amplified spontaneous emission
SACLA	SPring-8 angstrom compact free-electron laser
SPARC	sorgente pulsate amplificata radiazione coerente
YAG	yttrium aluminium garnet

Bibliography

[1] G. Margaritondo, Introduction to synchrotron radiation, Oxford University Press (1988).

[2] A. H. Zewail, Phys. Chem., 104, 5660 (2000).

[3] M. Chergui and A. H. Zewail, Phys. Chem., 10, 28 (2009).

[4] H. N. Chapman et al., Nature, 448, 676, (2007).

[5] C. Blome, Th.Tschentscher, J. Davaasambuu, P. Durand and S. Techert, Journal of synchrotron radiation. 12, 812 (2005).

[6] F.B. Rosmej et al., Journal of physics: Conference Series, 72, 012007 (2007).

[7] J. Madey, J. Appl. Phys., 42, 1906 (1971).

[8] L. R. Elias et al. Phys. Rev. Lett., 36, 717 (1976).

[9] C. Pellegrini, LCLS-TN-98-3 (1998). Available at https://www-ssrl.slac.stanford.edu/lcls/lcls_tech_notes.html

[10] P. Emma et al., Nature Photonics, 4, 641 (2010).

[11] V. Ayvazyan et al., Eur. Phys. J. D., 37, 297 (2006).

[12] T. Ishikawa et al., Nature Photonics, 6, 540 (2012).

[13] E. Allaria et al., Nature Photonics, 6, 699 (2012).

[14] M. Born and E. Wolf, Principles of Optics: Electromagnetic Theory of Propagation, Interference and Diffraction of Light, Cambridge University Press (1999).

[15] http://www.pma.caltech.edu/Courses/ph136/yr2012/1209.1.K.pdf

[16] J. Kirz, Nature Physics, 2, 799 (2006).

[17] M. J. Bogan et al., J. Phys. B: At. Mol. Opt. Phys., 43, 194013 (2010).

[18] J. Welch et al., Proc. of FEL 2011, 461, Shanghai, China (2011).

[19] C, Gutt, Phys. Rev. Lett., 108, 024801 (2012)

[20] L. -H. Yu et al., Phy. Rev. Lett., 91, 074801 (2003).

[21] G. De Ninno et al., Phys. Rev. Lett., 101, 053902 (2008).

[22] L. Giannessi et al., Phys. Rev. Lett., 108, 164801 (2011).

[23] N. Cutic et al., Phys. Rev. ST Accel. Beams, 14, 030706 (2011).

[24] C. J. Bochetta et al., FERMI commisioning design report, Trieste (2007). Available at https://www.elettra.trieste.it/FERMI/index.php?n=Main.CDRdocument

[25] S. T. Cundiff and S. Mukamel, Phys. Today, 66, 44 (2013)

[26] S. Mukamel, D. Healion, Y. Zhang and J. D.Biggs, Annual Review of Physical Chemistry, 64, 101 (2013).

[27] I. V. Schweigert and S. Mukamel, Phys. Rev. Lett. A,76, 0125041 (2007).

[28] I. V. Schweigert and S. Mukamel, Phys. Rev. Lett., 99, 163001 (2007).

[29] L. Weinhardt et al., J. Chem. Phys., 135, 104705 (2011).

[30] F. Bencivenga and C. Masciovecchio, Nucl. Instrum. Meth. Phys. Res. A, 606, 785 (2009).

[31] R. I. Tobey et al., Appl. Phys. Lett., 89, 091108 (2006).

[32] G. Dattoli and A. Renieri, Experimental and Theoretical Aspects of the Free-Electron, in Laser Handbook 4, North-Holland (1985).

[33] G. Dattoli, A. Renieri and A. Torre, Lectures on the Free-Electron Laser Theory and Related Topics, World Scientific (1993).

[34] W. B. Colson et al., Phys. Lett. A, 64, 190 (1977).

[35] E. L. Saldin, E. A. Schneidmiller and M. V. Yurkov, The Physics of Free Electron Lasers, Springer-Verlag (1999).

[36] R. Bonifacio, L. De Salvo and P. Pierini, Nucl. Instrum. Meth. Phys. Res. A, 293, 627 (1990).

[37] R. Bonifacio, et al., Phys. Rev. Lett., 73, 70 (1994).

[38] R. Bonifacio, C. Pellegrini and L. M. Narducci, Opt. Commun., 50, 373 (1984).

[39] R. Bonifacio et all., Riv. Nuovo Cimento Soc. Ital. Fis., 13, 1 (1990).

[40] J. R. Pierce, Traveling-Wave Tubes, D. Van Nostrand Company Inc. (1950).

[41] E. L. Saldin, E. A. Schneidmiller and M. V. Yurkov, Opt. Commun., 281, 1179 (2008).

[42] E. L. Saldin, E. A. Schneidmiller and M. V. Yurkov, Opt. Commun., 281, 4727 (2008).

[43] R. W. Warren et al., J. Quantum Electronics, 19, 381 (1983).

[44] P. F. Moulton, J. Opt. Soc. Am. B, 3, 125 (1986).

[45] K. Miyata, Opt. Lett., 36, 3627 (2011).

[46] P. Balcou et al., Z. Phys., 34, 107 (1995).

[47] T. Brabec and F. Krausz, Rev. Mod. Phys., 72, 545 (2000).

[48] L. -H. Yu, Phys. Rev. A, 44, 5178 (1991).

[49] I. Ben-Zvi, K.M. Yang and L. -H. Yu, Nucl. Instrum. Meth. Phys. Res. A, 318, 726 (1992).

[50] J. Deacon et al., Phys. Rev. Lett., 38, 892 (1979).

[51] N. A. Vinokurov et al., Rev. Sci. Instr., 60, 1435 (1989).

[52] P. Kadkhoda et al., Proc. of SPIE 4099, 311 (2001).

[53] N. A. Vinokoruv, Nucl. Instrum. Meth. Phys. Res. A, 375, 264 (1996).

[54] N. A. Vinokoruv and O. A. Schevchenko, Nucl. Instrum. Meth. Phys. Res. A, 528, 491 (2004).

[55] M. Xie, Proc. of PAC 1995, 183, Dallas, Texas (1995).

[56] L. -H. Yu and J. Wu, Nucl. Inst. Meth. A, 507, 455 (2003).

[57] H. Wiedemann, Particle Accelerator Physics: Basic Principles and Linear Beam Dynamics, 2nd ed., Springer-Verlag (1999).

[58] K. -J. Kim, Nucl. Instrum. Meth. A, 250, 396 (1986) and Phys. Rev. Lett., 57, 1871 (1986).

[59] C. Pellegrini, The European Physical Journal H, 37, 659 (2012).

[60] J. S. Fraser, R. L. Sheffield and E. R. Gray, Nucl. Instr. and Meth. in Phys. Res. A, 250, 71 (1986).

[61] LCLS Conceptual design report, SLAC Report: SLAC-R-593 (2002). Available at http://www.slac.stanford.edu/pubs/slacreports/slac-r-521.html

[62] B. E. Carlsten, Nucl. Instr. Meth. Phys. Res. A, 285, 313 (1989).

[63] J. B. Rosenzweig and L. Serafini, Phys. Rev. E, 55, 7565 (1997).

[64] M. Ferrario et al., Phys. Rev. Lett., 99 234801 (2007).

[65] T. P. Wangler, RF Linear Accelerators, John Wiley & Sons (2008).

[66] Ph. Piot, Proc. of LINAC 2004, 528 (2004).

[67] K. Flöttmann, T. Limberg and Ph. Piot, DESY-TESLA-FEL-01-06 (2001). Available at http://flash.desy.de/reports_publications/tesla_fel_reports/

[68] E. L. Saldin, E. A. Schneidmiller and M. V.Yurkov, Nucl. Instr. Meth. Phys. Res. A, 490,1 (2002).

[69] E. Allaria et al., Proc. of FEL 2012, 213, Nara, Japan (2012).

[70] M. Altarelli et al., The European X-Ray Free-Electron Laser conceptual design report, Hamburg (2006).

[71] H. S. Kang and S. H. Nam, Proc. of FEL 2010,155 (2010).

[72] P. Emma et al., Phys. Rev. Lett., 92, 074801 (2004).

[73] A. A. Zholents and W. M. Fawley, Phys. Rev. Lett., 92, 224801 (2004).

[74] E. L. Saldin et al., Phys. Rev. ST Accel. Beams, 9, 050702 (2006).

[75] L. Giannessi et al., Phys. Rev. Lett., 106,144801 (2011).

[76] J. Feldhaus et al., Opt. Commun., 140, 341 (1997).

[77] J. Amann et al., Nature Photonics, 6, 693 (2012).

[78] H. N. Chapman et al., Nature Physics, 2, 839 (2006),

[79] A. Barty et al., Nature Photonics, 2, 415 (2008),

[80] M. Marvin et al., Nature, 470, 78 (2011).

[81] L. Redecke et al., Science, 339, 227 (2013).

[82] G. Lambert et al., Proceedings of FEL 2006, 138 (2006).

[83] L. Giannessi et al., Proc. of FEL 2012, 13, Nara, Japan (2012).

[84] E. Allaria et al., Nature Photonics, 7, 913 (2013).

[85] P. J. Bryant, A brief history and review of accelerators, in proc. of general accelerator physics school of CERN 1992 (Jyvaeskylae) vol. 1, 1, CERN, Geneva (1994).

[86] E. D. Courant and H. S. Snyder, Ann. Phys., 3, 1 (1958).

[87] M. Röhrs, Investigation of the Phase Space Distribution of Electron Bunches at the FLASH-Linac Using a Transverse Deflecting Structure. Phd Thesis, Hamburg University, Hamburg, Germany (2008).

[88] P. Castro, DESY-TECHNICAL-NOTE-03-01 (2003). Available at http://www.desy.de/~ahluwali/technicalnotes/calc_path_len_castro_mpy.pdf

[89] L. A. Pipes, Applied mathematics for engineers and physicists, McGraw-Hill, (1958).

[90] J. Rossbach and P. Schmüser, Basic course on accelerator optics, in proc. of general accelerator physics school of CERN 1992 (Jyvaeskylae) vol. 1, 17, CERN, Geneva (1994).

[91] S. Di Mitri, Machine Design and Electron Beam Control of a Single-Pass Linac for Free-Electron Laser: The FERMI@Elettra Case Study. Phd Thesis. Groningen University, Groningen, Netherlands (2011).

[92] D. Dowell et al., Proc. of PAC 1995, Dallas, Texas (1995).

[93] P. Emma, LCLS-TN-01-1 (2001). Available at https://www-ssrl.slac.stanford.edu/lcls/lcls_tech_notes.html

[94] M. Borland et al., Nucl. Instrum. Methods Phys. Res., A 483, 268 (2002).

[95] Z. Huang et al., Phys. Rev. ST Accel. Beams, 7, 074401 (2004).

[96] M. Venturini, Phys. Rev. ST Accel. Beams, 10, 104401 (2007).

[97] M.Venturini and A. A. Zholents, Nucl. Instrum. Meth. Phys. Res. A, 593, 53 (2008).

[98] S. Di Mitri et al., Nucl. Instrum. Meth. Phys. Res. A, 608, 19 (2009).

[99] T. Limberg, Ph. Piot, and E. A. Schneidmiller, Nucl. Instrum. Methods Phys. Res. A, 475, 353 (2001).

[100] S. Heifets, S. Stupakov and S. Krinsky, Phys. Rev. ST Accel. Beams, 5,064401 (2002).

[101] J. Wu et al., SLAC-PUB-10430 (2004). Available at http://www.slac.stanford.edu/cgi-wrap/getdoc/slac-pub-10430.pdf

[102] T. Shaftan and Z. Huang, Phys. Rev. ST Accel. Beams, 7, 080702 (2004).

[103] T. Shaftan et al., in Proc. of PAC2003, 30, Portland, Oregon (2003).

[104] T. Shaftan et al., Nucl. Instrum. Meth. Phys. Res, A, 528, 397 (2004).

[105] A. A. Zholents, ST/F-TN-05-14 (2005). Available at fermi@elettra.trieste.it

[106] E. L. Saldin, E. A. Schneidmiller, M. V. Yurkov, Nucl. Instrum. Methods Phys. Res. A, 528, 355 (2004).

[107] S. Spampinati, S. Di Mitri and B. Diviacco, Proc. of FEL 2007, 362, Novosibirsk, Russia (2007).

[108] Z. Huang et al., Phys. Rev. ST Accel. Beams, 13, 020703 (2010).

[109] S. Krinsky and L. -H. Yu, Phys. Rev. A, 35, 3406 (1987).

[110] G. Dattoli, P. L. Ottaviani and S. Pagnutti, Journ. Appl, Phys., 97, 113102 (2005).

[111] L. -H. Yu, S. Krinsky and R. L. Gluckstern, Phys. Rev. Lett., 64, 3011 (1990).

[112] Y. H. Chin, K. -J. Kim and M. Xie, Phys. Rev. A, 46, 6662 (1992).

[113] K.-J. Kim and M. Xie, Nucl. Instrum. Methods Phys. Res. A, 331, 359 (1993).

[114] W. Fawley et al., Proc. of PAC 1993, 1530, Washington, D. C. (1993).

[115] G. D'Auria et al., Proc. of PAC 2007, 974 (2007).

[116] S. Di Mitri et al., Proc. of FEL 2010, 26, Malmö, Sweeden (2010).

[117] M. Kokole et al., Proc. of FEL 2010, 664, Malmö, Sweeden (2010).

[118] M. Zangrando et al., Proc. of AIP 2010, 1234, 3 (2010).

[119] M. Zangrando, Proc. of FEL 2010, 716, Malmö, Sweden (2010).

[120] A. Di Cicco et al., Journal of Non-Crystalline Solids, 357, 2641-2647 (2011).

[121] E. Pedersoli et al., Rev. Sci. Instrum., 82, 043711 (2011).

[122] D. Palmer, The Next Generation photoinjector. Phd Thesis, Stanford University, Menlo Park, USA (1998).

[123] G. Penco, S. Di Mitri and S. Spampinati, Proc. of EPAC 2008, 1230, Genova, Italy (2008).

[124] J. Welch, Proc. of FEL 2008, 313, Geongju, Korea (2008)

[125] G. D'Auria et al., Proc. of IPAC 2010, 2173, Kyoto, Japan (2010).

[126] G. Penco et al., Proc. of FEL 2012, 417, Nara, Japan (2012).

[127] G. A. Loew and O. H. Altemueller, SLAC-PUB-135 (1965). Available at http://www.slac.stanford.edu/cgi-wrap/getdoc/slac-pub-0135.pdf

[128] P. Craievich et al., Proc. of DIPAC 2007, 168, Venice, Italy (2007).

[129] M. Petronio, Research and Applications of Radio-Frequency Deflecting Cavities. Phd Thesis, University of Trieste, Trieste, Italy (2011)

[130] V. L. Ginzburg and V. N. Tsytovich, Transition Radiation and Transition Scattering (Adam Hilger, Bristol, 1990).

[131] W. Graves and P. G. O'Shea,Proc. of PAC 1997, 1995, Vancouver, Canada (1997).

[132] M. Dal Forno et al., Proc. of FEL 2013, 3309, New York, New York (2013).

[133] B. Diviacco et al., Proc. of IPAC 2011, 3278, San Sebastián, Spain (2011).

[134] M. Dal Forno et al., Nucl. Instrum. Meth. Phys. Res. A, 662, 1 (2012).

[135] M. B. Danailov et al., Proc. of FEL 2011, 183, Shanghai, China (2011).

[136] M. Zangrando et al., Proc. of FEL 2010, 706, Malmö, Sweden (2010).

[137] M. Zangrando et al., Proceeding of SPIE conference, 8504, (2012).

[138] R. Akre et al., Phys. Rev. ST Accel. Beams 11, 030703 (2008).

[139] R. Akre et al., Proc. of FEL 2008, 548, Gyeongju, Korea (2008).

[140] Y. Ding et al., SLAC-PUB-13525 (2009). Available at http://www.slac.stanford.edu/cgi-wrap/getdoc/slac-pub-13525.pdf

[141] M. White et al., Proc. of LINAC 2008, 1087, Victoria, Canada (2008).

[142] H-N. Nuhn et al., Proc. of FEL 2009, 714, Liverpool, England (2009).

[143] D. R. Walters et al., Proc. of FEL 2008, 455, Gyeongju, Korea (2008).

[144] P. Emma, R. Carr and H.-D. Nuhn. Nucl. Inst. and Meth. Res. A, 429, 407 (1999).

[145] K. Hacker and Z. Wolf, LCLS-TN-05-4 (2005). Available at https://www-ssrl.slac.stanford.edu/lcls/lcls_tech_notes.html

[146] H-N. Nuhn et al., Proc. of FEL 2006, 529, Berlin, Germany (2006) .

[147] S. Moeller et al., SLAC-PUB-14348 (2010). Available at http://www.slac.stanford.edu/cgi-wrap/getdoc/slac-pub-13525.pdf

[148] M. Ferrario et al., Proc. of Fel 2009, 734, Liverpool, England (2009).

[149] M. Quattromini et al., Proc. of EPAC 2008, 2297, Genova, Italy (2008).

[150] L. Serafini and M. Ferrario, Proc. of AIP 2001, 581, 87 (2001).

[151] M. Ferrario et al., Phys. Rev. Lett., 104, 054801 (2010).

[152] M. Labat et al., Phys. Rev. Lett., 107, 224801 (2011).

[153] N. Y. Joly et al., Proc. of FEL 2012, 269, Nara, Japan (2012).

[154] G. Marcus et al., Appl. Physics Lett., 101, 134102 (2012).

[155] C. Gutt et al., Phys. Rev. Lett., 108, 024801 (2012).

[156] S. Spampinati et al., Proc. of FEL 2012, 177, Nara, Japan (2012).

[157] S. G. Biedron, S. V. Milton and H. P. Freund, Nucl. Instrum. Meth, Phys. Res. A, 475, 401 (2001).

[158] A. Lutman, et al., J. Phys. A: Math. Theor., 42, 085405 (2009).

[159] A. Marinelli et al., Phys. Rev. ST Accel. Beams, 13, 070701 (2010).

[160] S. Reiche, Nucl. Instrum. Meth. Phys. Res. A, 429, 243 (1999).

[161] W. M. Fawley, LCLS-TN-04-3 (2004). Available at https://www-ssrl.slac.stanford.edu/lcls/lcls_tech_notes.html

[162] S. Di Mitri, M. Cornacchia, C. Scafuri and M. Sjostrom, Phys. Rev. Lett., 15, 012802 (2012).

[163] E. Ferrari et al., Proc. of IPAC 2012, 1741, New Orleans, Luisiana (2012).

[164] S. Di Mitri, M. Cornacchia and S. Spampinati, Phys. Rev. Lett., 110, 014801 (2013).

[165] M. Borland, ANL/A Report LS-287 (2000). Available at http://www.aps.anl.gov/Science/Publications/lsnotes/ls287.pdf

[166] H. Loos, SLAC-PUB-13395 (2008). Available at http://slac.stanford.edu/cgi-wrap/getdoc/slac-pub-13395.pdf

[167] R. Fiorito, Proc. of FEL 2009, 714, Liverpool, England (2009).

[168] S. Spampinati et al., Proc. FEL2013, 680, New York, New York, (2013).

[169] W. Ackermann et al., Nature Photonics, 1, 336 (2007).

[170] D. F. Ratner, A. Fry, G. Stupakov and W. White, Phys. Rev. ST Accel. Beams, 15, 030702 (2012).

[171] J. Welch et al., Proc. FEL 2011, 461, Shanghai, China (2011).

[172] L. Giannessi, P. Musumeci and S. Spampinati, J.Appl. Phys., 98, 043110 (2005) .

[173] L. Giannessi et al., Phys. Rev. Lett., 110, 044801 (2013).

[174] L. Giannessi and P. Musumeci, New Journal of physics, 8, 294 (2006).

[175] G. Geloni, V. Kocharyan and E. L.Saldin, J. Mod. Opt., 58, 1391 (2011).

[176] R. Lindberg and Y. Shvyd'ko, Phys. Rev. ST Accel. Beams, 15, 050706 (2012).

[177] A. Authier, Dynamical theory of X-ray diffraction. IUCr monographs on crystallography, no. 11. Oxford University Press (2003).

[178] R. Kronig, J. Opt. Soc. Am., 12, 547 (1926).

[179] H. A. Kramers, Phys. Z., 30, 522 (1929).

[180] J. S. Toll, Phys. Rev. Let., 104, 1760 (1956).

[181] Z. Huang, K. Bane, Y. Ding and P. Emma, Phys. Rev. ST Accel. Beams, 13, 092801 (2010).

[182] D.J. Dunning, E. Prat, S. Reiche, Proc. FEL 2012, 281, Nara, Japan (2012).

[183] J. Qiang, S. Lidia, R. D. Ryne and C. Limborg-Deprey, Phys. Rev. ST Accel. Beams, 9, 044204, (2006).

[184] S. J. Hahn and J. K. Lee, Phys. Rev. E, 48, 2162 (1993).

[185] J. Wu et al., J. Opt. Soc. Am., B, 24, 484 (2007).